Mid-Infrared Photonics in Silicon

(Article begins on next page)

Mid-Infrared Photonics in Silicon

A DISSERTATION PRESENTED

BY

RAJI SHANKAR

TO

THE SCHOOL OF ENGINEERING AND APPLIED SCIENCES

IN PARTIAL FULFILLMENT OF THE REQUIREMENTS

FOR THE DEGREE OF

DOCTOR OF PHILOSOPHY

IN THE SUBJECT OF

ENGINEERING SCIENCES

HARVARD UNIVERSITY

CAMBRIDGE, MASSACHUSETTS

APRIL 2013

Thesis advisor: Marko Lončar   Raji Shankar

Mid-Infrared Photonics in Silicon

Abstract

The mid-infrared wavelength region (2-20 μm) is of great utility for a number of applications, including chemical bond spectroscopy, trace gas sensing, and medical diagnostics. Despite this wealth of applications, the on-chip mid-IR photonics platform needed to access them is relatively undeveloped. Silicon is an attractive material of choice for the mid-IR, as it exhibits low loss through much of the mid-IR. Using silicon allows us to take advantage of well-developed fabrication techniques and CMOS compatibility, making the realization of on-chip integrated mid-IR devices more realistic. The mid-IR wavelengths also afford the opportunity to exploit Si's high third-order optical nonlinearity for nonlinear frequency generation applications.

In this work, we present a Si-based platform for mid-IR photonics, with a special focus on micro-resonators for strong on-chip light confinement in the 4-5 μm range. Additionally, we develop experimental optical characterization techniques to overcome the inherent difficulties of working in this wavelength regime. First, we demonstrate the design, fabrication, and characterization of photonic crystal cavities in a silicon membrane platform, operational at 4.4 μm (Chapter 2). By transferring the technique known as resonant scattering to the mid-IR, we measure quality (Q) factors of up to 13,600 in these photonic crystal cavities. We also develop a technique known as scanning resonant scattering microscopy to image our cavity modes and optimize alignment to our devices.

Next, we demonstrate the electro-optic tuning of these mid-IR Si photonic crystal cavities using gated graphene (Chapter 3). We demonstrate a tuning of about 4 nm, and demonstrate the principle of on-chip mid-IR modulation using these devices. We then investigate the phenomenon of optical bistability seen in our photonic crystal cavities (Chapter 4). We discover that our bistability is thermal in origin and use post-processing techniques to mitigate bistability and increase Q-factors.

We then demonstrate the design, fabrication, and characterization grating-coupled ring resonators in a silicon-on-sapphire (SOS) platform at 4.4 µm, achieving intrinsic Q-factors as high as 278,000 in these devices (Chapter 5). Finally, we provide a quantitative analysis of the potential of our SOS devices for nonlinear frequency generation and describe ongoing experiments in this regard (Chapter 6).

Contents

Author List

The following authors contributed to Chapter 2: **Rick Leijssen and Irfan Bulu**.
Portions of this chapter appear in

- Raji Shankar, Rick Leijssen, Irfan Bulu, and Marko Lončar. Mid-infrared photonic crystal cavities in silicon. *Opt.Express*,19(6): 5579-5586, March 2011.

The following authors contributed to Chapter 3: **Yu Yao, Julie Frish, Ian Frank, Yi Song, Jing Kong, and Federico Capasso**

The following authors contributed to Chapter 4: **Irfan Bulu and Rick Leijssen**
Portions of this chapter appear in:

- Raji Shankar, Irfan Bulu, Rick Leijssen, and Marko Lončar. Study of thermally-induced optical bistability and the role of surface treatments in Si-based mid-infrared photonic crystal cavities. *Opt.Express*, 19(24):24828-24837, Nov 2011.

The following authors contributed to Chapter 5: **Irfan Bulu**.
Portions of this chapter appear in:

- Raji Shankar, Irfan Bulu, and Marko Lončar. Integrated high-quality factor silicon-on-sapphire ring resonators for the mid-infrared. *AppliedPhysicsLetters*, 102(5):051108, 2013.

The following authors contributed to Chapter 6: **Irfan Bulu**

Listing of figures

To my parents.

Acknowledgments

Completing a PhD is not unlike raising a child, if that oft-cited African proverb is anything to go by: it takes a village. This is my effort to thank all the village denizens who have made this thesis possible.

Most of all, I would like to thank my PhD advisor, Professor Marko Lončar, for all his guidance and support throughout my time at Harvard. Marko had established his group only a few months before I arrived at Harvard, and since I was one of the "Original Six" students he hired in his first full year, I wasn't quite sure what to expect. Happily, the lab environment that Marko fostered turned out to be even better than anything I envisioned. I feel very fortunate that I was given the opportunity to help build up the lab from scratch, which was a wonderful learning experience on its own. Marko is a great scientific mentor, with a talent for achieving a balance between providing his own ideas and

respecting those of his students. I am especially grateful that he trusted me enough to handle the decision-making for the mid-infrared project from the start, allowing me to develop as an independent researcher. Additionally, I deeply appreciate Marko's kindness and optimistic nature, as well as his willingness to cheerfully tolerate my irreverent sense of humor. Most importantly, I would like to thank Marko for having faith in my abilities even when I did not have faith in myself. No matter what I may do next, Marko has provided me with a model of mentorship that I will do my best to emulate in the future.

Marko also had a great knack for hiring amazing people to populate his lab group. Without these people, the countless hours I spent in lab would not have been so enjoyable nor so productive. Many of my best friends of the last 6 years have come from the Lončar group, and I hope our friendships will continue for the rest of our lives. First, I would like to thank our group's original three postdocs: Dr. Mughees Khan, Dr. Murray McCutcheon, and Dr. Irfan Bulu. Mughees was our (very patient) guru of fabrication and could always be counted on to provide a solution to any fabrication issues we could conjure. Murray provided much of the resonant scattering know-how for our group and introduced us all to Lumerical. I would especially like to thank Irfan, who was my close (and often only) collaborator for most of the work described in this thesis. He was the theoretical powerhouse behind much of the mid-infrared project, and was a fantastic mentor and friend throughout my PhD.

I would also like to specially thank the "first generation" students who were there with me in the Lončar Lab from the very beginning. I feel lucky that I had

such an amazingly talented and helpful peer group to work with and learn from. Parag Deotare was an academic "elder brother" to us and always went out of his way to help me or give me advice on any problem, large or small. Tom Babinec was a doyen of optical setup-building knowledge and a source of many interesting late-night discussions, with topics ranging from Pink Floyd to the American political system. Qimin Quan gave me a great deal of help with simulations and provided many useful discussions on the bistability project in particular.

I regard the fact that Yinan Zhang and I were in the same lab group as a felicitous coincidence, as I have gained so much from this friendship. Thank you, Yinan, for all the discussions on topics all and sundry, the life advice and philosophy, and most importantly, all the funny moments we shared. Also, I thank Yinan for being a willing subject for most of my "Associated Press" dispatches from the Lončar Group. I am also grateful that I got to be friends with Jennifer Choy, a paragon of kindness and humility. I thank JC for her support and wise counsel, especially when we were "wandering together in the wilderness" in the earlier part of our PhDs. Birgit Hausmann is another exceptionally generous and thoughtful friend. I thank Birgit for all the heart-to-heart talks and road trip adventures we shared–I'm glad we finally got to go to the US Open!

Ian Burgess was always willing to share his prodigious knowledge in both physics and chemistry, which was was helpful on many occasions. I also greatly admire Ian B.'s grandmaster-like ability to think many steps ahead in life. I thank Ian Frank for working with me on the PSI collaboration as well as for providing ALD alumina for the graphene project. Ian F.'s wide-ranging scientific knowledge

has benefitted me and everyone else who has had the pleasure of discussing science with him.

I was also fortunate enough to mentor two wonderful students during my PhD. Rick Leijssen was a master's student from the Netherlands who worked with me for 6 exceptionally productive and fun months. While I was ostensibly Rick's mentor, I learned as much from Rick as he did from me. I am sure Rick will be very successful as he starts his own PhD back in the Netherlands. Julie Frish was an undergraduate student from Boston University who worked with me on the graphene project. I was very impressed with her enthusiasm for the cleanroom and willingness to accommodate research in her schedule even during her very busy semesters. Recently, I have started working with Ray Ng, and I wish him all the best as he continues the mid-IR project.

I would also like to thank the following members of the Loncar Group for helpful discussions (and friendship) throughout the years: Dr. Eiji Iwase, Dr. Alejandro Rodriguez, Dr. Dan Floyd, Dr. Dan Ramos, Dr. Stefan Kalchmair, Dr. Vivek Venkataraman, Wallace Hui, Mike Burek, Haig Atikian, Anna Shneidman, Erika Janitz and Leonard Kogos.

Professor Federico Capasso and his lab group provided invaluable assistance to me during my PhD, especially when I was setting up the mid-IR resonant scattering setup and needed advice on mid-IR optical components. I would like to especially single out Dr. Christian Pflugl, Dr. Laurent Diehl, Romain Blanchard, Mikhail Kats, and David Woolf for thanks. Additionally, I would like to thank Dr. Yu Yao, my close collaborator on the graphene project. I have greatly

me to the world of optics research.

I also formed many wonderful friendships outside of the lab during my time at Harvard, and these friendships have enriched my life considerably. I cannot possibly name everyone, but I would like to single out a few in particular: my former roommate Mandrita Datta, my current roommate Alison Rosenblum (who helped keep me fed during the writing of this thesis), and my best friend during graduate school, Lusann Wren Yang. Wren, thanks for all the adventures and the innumerable conversations (almost every single day!) we've had over the last 6 years.

Finally, I would like to thank my parents for all the love and support they have given me throughout my entire life. My father, Dr. P. Mohana Shankar, was my inspiration for embarking upon this PhD. My mother, Rajakumari Shankar, has always has been a source of great comfort to me and never passes on an opportunity to pamper me with home-cooked food. I dedicate this thesis to them.

There are two ways of spreading light: to
be the candle or the mirror that reflects it.

-Edith Wharton

1

Introduction

The mid-infrared (IR) wavelength range (2-20 μm) is often referred to as the
"fingerprint region", since most molecules have uniquely identifiable absorption
spectra within this wavelength range. Because of this, the mid-IR region is of great
utility for a number of applications, including chemical bond spectroscopy, trace

gas sensing, and medical diagnostics. Additionally, the mid-IR wavelength region is also particularly suited for thermal imaging and free-space communications, especially within the atmospheric windows of 3-5 μm and 8-11 μm.

Despite this wealth of applications, the on-chip mid-IR photonics platform needed to access them is relatively undeveloped. While the last 10-15 years have seen the development of high-power, room temperature-operational mid-IR light sources and sensitive mid-IR detectors, little work has been done in developing the passive photonics elements such as waveguides, resonators, splitters, modulators, etc. for the mid-IR. Conventionally, mid-IR photonics has been associated with the III-IV materials used for active optoelectronic devices (lasers and detectors), as well as chalcogenide glasses used for passive photonic elements [1]. However, R. Soref *et al.* proposed in 2006 that group IV materials (silicon and germanium) are also promising mid-IR materials, as they exhibit low loss through much of the mid-IR [2]. In particular, silicon is an attractive material of choice for the mid-IR, as we can take advantage of extremely well-developed fabrication techniques and CMOS compatibility, making the realization of on-chip integrated mid-IR devices more realistic. In Figure 1.0.1, we show the imaginary part of the refractive index of Si, κ, plotted as a function of wavelength for mid-IR wavelengths (data taken from [3]). Below 6.5 μm, κ is smaller than 10^{-6}, which offers the potential for extremely strong light confinement in Si devices from 2 to 6.5 μm.

Finally, due to the lack of two- and three-photon absorption in the mid-IR, the power density of optical signals propagating in Si waveguides or stored in Si
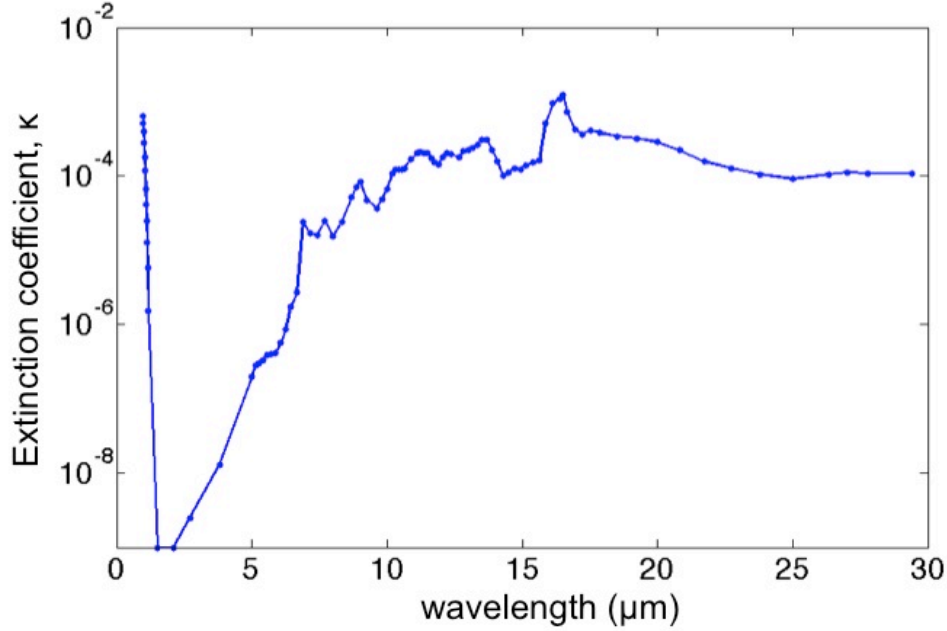
Figure 1.0.1: The extinction coefficient, κ, as a function of wavelength for silicon. Data taken from [3].

optical cavities can be significantly higher than at the near-IR wavelengths used for telecommunications [4–8]. Because of this, the mid-IR wavelengths afford the opportunity to exploit Si's high third-order optical nonlinearity $(n_2 = 3.6x10^{-18} m^2/W$ [9]$)$ for nonlinear frequency generation applications, since these applications require high pump powers. On-chip four-wave mixing, parametric oscillation, and most excitingly, frequency comb generation should be possible at mid-IR wavelengths in the proper Si platform. On-chip frequency combs would be especially useful for mid-IR sensing and spectroscopic applications, as broadband sources are often required for these applications.

The work presented in this thesis is focused on the development of a Si mid-IR

photonics platform, mainly in the form of mid-IR microresonators, as well as the development of tools to effectively characterize mid-IR photonic devices. Applications in modulation, trace gas sensing, and nonlinear wavelength generation are also discussed.

In Chapter 2, we discuss the design, fabrication, and characterization of mid-IR photonics crystal cavities in a Si membrane platform. Chapter 3 discusses the electro-optic tuning of these photonics crystal cavities using graphene, a potential method for on-chip modulation at the mid-IR. In Chapter 4, we discuss the phenomenon of optical bistability in our photonic crystal cavities, and the role of surface treatments in decreasing absorption loss and mitigating bistability. Chapter 5 describes the design, fabrication, and characterization of mid-IR ring resonators in a silicon-on-sapphire (SOS) platform. This is a particularly suitable platform for integrated mid-IR photonics in the 2-5 μm range. In the final chapter, Chapter 6, we discuss the use of our SOS ring resonators for nonlinear frequency generation in the mid-IR.

2

Mid-Infrared Photonic Crystal Cavities in Silicon

In this chapter, we demonstrate the first wavelength-scale optical resonators for the mid-IR, in the form of L3 photonic crystal cavities [10] fabricated in the

CMOS compatible silicon-on-insulator material platform [11]. High quality factor (Q) and low mode volume optical resonators in the mid-IR are of interest for many applications including trace gas sensing, optical interconnects, and so on.

2.1 Design of Photonic Crystal Cavities

Optical resonators or cavities are indispensable to to the field of photonics, as the ability to strongly confine light is essential for lasers, sensors, filters, and many other applications. With advances in microfabrication techniques, ultrasmall optical resonators are now easily achievable, allowing for strong light confinement at the nano-and micro-scale. There are two important figures of merit relevant to optical resonators:

- The quality factor, **Q**. Q is a measure of the quality of the resonator, i.e. how well light is confined within the optical cavity. It is defined as $Q = \frac{\omega W}{P}$, where ω is the resonance frequency of the the optical resonator, W is the energy stored within the resonator, and P is the power radiated by the resonator. We can also think of the Q in terms of the photon lifetime τ_{ph}, which is the amount of time the photon spends inside the cavity before being leaked out: $Q = \omega \tau_{ph}$. The Q is also a measure of the bandwidth of a resonator in frequency space around a resonance frequency: $Q = \frac{\omega}{\Delta \omega}$, where $\Delta \omega$ is the line width of the cavity resonance. High Qs are very often desirable for many applications due to their strong light confinement and narrow linewidth.

- The mode volume, **V**. The mode volume of a resonator, V, is the volume occupied by the energy of the mode. It can be expressed analytically as $V_{mode} = \frac{\int \varepsilon(\mathbf{r})|\mathbf{E}(\mathbf{r})|^2}{max[\varepsilon(\mathbf{r})|\mathbf{E}(\mathbf{r})|^2]}$.

High Q-factors and small mode volumes V are often desirable for many applications, especially those requiring strong light-matter interactions, such as the enhancement of spontaneous emission and strong coupling. One particular resonator design that is notable for a high Q/V ratio is the so-called photonic crystal cavity, which relies on distributed Bragg reflection for light confinement in at least one dimension. Photonic crystal cavities for the mid-IR will be the focus of Chapters 2 and 3.

Photonic crystals are structures that involve distributed Bragg reflection (DBR) in at least one dimension [12]. The classic example of distributed Bragg reflection in one-dimension is the so-called Bragg stack, which consists of a repeating stack of two different materials with refractive indices n_1 and n_2. If the thickness t of the material layers is chosen such that $t = \frac{\lambda}{4n}$, the stack will exhibit very high reflectivity in normal incidence. As the number of periods increases, the reflectivity of the Bragg stack will also increase. While we can describe such a structure in real space, in practice it is preferred to describe periodic reflectors such as these in the Fourier domain, in terms of k-vectors. A 1-D Bragg stack with periodicity a in the x-direction can be described by the relation $k_x = 2\pi/a$. A simple resonator may be formed by placing a cavity (of thickness a) between two DBRs.

Bragg reflection and confinement need not be restricted to one dimension, however. For ease of fabrication and integration, there has been much interest in planar devices with Bragg reflection in two dimensions, known as 2-D photonic crystals. Many variations of 2D photonic periodic lattices exist; two of the most common are the square lattice of holes in a slab, and the triangular lattice of holes in a slab, shown in Figure 2.1.1 (arrays of rods can also support Bragg reflection). The triangular lattice is particularly useful since it can act as a Bragg reflector for all in-plane k-vectors (i.e., have a complete bandgap in-plane) for a broad range of frequencies depending on the choice of hole size and periodicity. Out of plane confinement is provided by total internal reflection within the slab.

To obtain the precise dispersion relationship between the k-vector and frequency, we need to solve Maxwell's equations for the structure. The most common numerical approach for doing so is known as finite difference time-domain (FDTD). In the FDTD method, Maxwell's equations are solved by spatial and temporal discretization. By launching sources (current, dipole, or field sources) around the structure of interest and monitoring its evolution in time at various points on a grid, and then taking the Fourier transform of the resultant time-evolved electromagnetic fields, we can obtain information about the frequency response of our structure in Fourier space. The result of a FDTD simulation of a triangular lattice of holes in a slab is shown in Figure 2.1.1 [13]. The blue area represents the "light cone", which is the projection of the states which can radiate into the air. The solid red and dashed blue lines represented guided modes, i.e. modes confined to the slab. Solid red lines are TE-like and
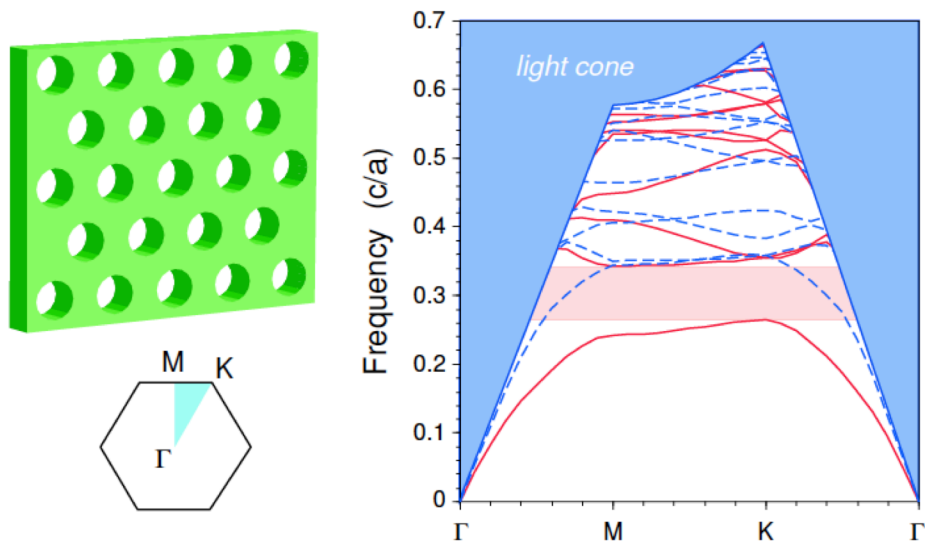
Figure 2.1.1: This is the band diagram for a dielectric slab of finite thickness with air holes. The blue area represents the "light cone", which is the projection of the states which can radiate into the air. The solid red and dashed blue lines represented guided modes, i.e. modes confined to the slab. Solid red lines are TE-like and solid blue lines are TM-like. For a slab with air holes in a 2-D triangular lattice, only TE-like modes support a band gap (region without guided modes). Taken from: http://ab-initio.mit.edu/photons/tutorial/photonic-intro.pdf [13], permission granted by Prof. Steven Johnson.

solid blue lines are TM-like. For a slab with air holes in a 2-D triangular lattice, only TE-like modes support a band gap (region without guided modes). However, even TE-like modes will radiate out of the slab if the translational symmetry is completely broken (as through a waveguide bend or a defect cavity). These vertical radiation losses can be minimized by design.

By introducing a small perturbation into a photonic crystal, we can create a so-called "defect mode" by locally changing the mode frequency and pulling it into the band gap. In this way, we can create photonic crystal cavities that can confine light in small mode volumes, usually on the order of $(\lambda/n)^3$. Many

different designs for photonic crystal cavities exist. For our photonic crystal cavities, we chose the well-known L3 cavity design [10] due to the relative ease of free-space in- and out-coupling in this cavity (Figure 2.1.2). This cavity design consists of a two-dimensional hexagonal photonic crystal lattice of air holes in a Si slab, with three central air holes removed to form a line defect. Bragg scattering accounts for electromagnetic confinement in the x and y directions, while index contrast provides confinement in the z direction. The cavity mode is linearly polarized. To further achieve confinement of the light to the cavity region, the air holes on either side of the cavity are shifted outwards, decreasing the phase mismatch between the cavity region and the Bragg mirror region formed by the photonic crystal (Figure 2.1.2). This allows for higher Q-factors to be achieved [10].

The cavities were designed using three-dimensional finite-difference time-domain method (Lumerical Solutions, Inc.) for a Si device layer thickness t of 500 nm. The periodicity of the photonic crystal lattice is $a = 1.34$ μm, and the air hole radius $r = 353$ nm ($r/a = 0.263$). The air hole shift s was scanned from zero shift to a maximum shift of $0.275a$ in order to optimize the Q factor of the cavity. An air hole shift of $s = 0.2a$ results in an optimal design at $\lambda = 4.615$ μm with a Q factor of 66,000 when 10 mirror hole pairs surround the cavity region. The mode profile is plotted in Figure 2.1.2, and the theoretical calculations for the resonance wavelength and Q factor as a function of s are shown in Figure 2.1.3. As expected, as the hole shift is increased, the cavity resonance is pushed to

10
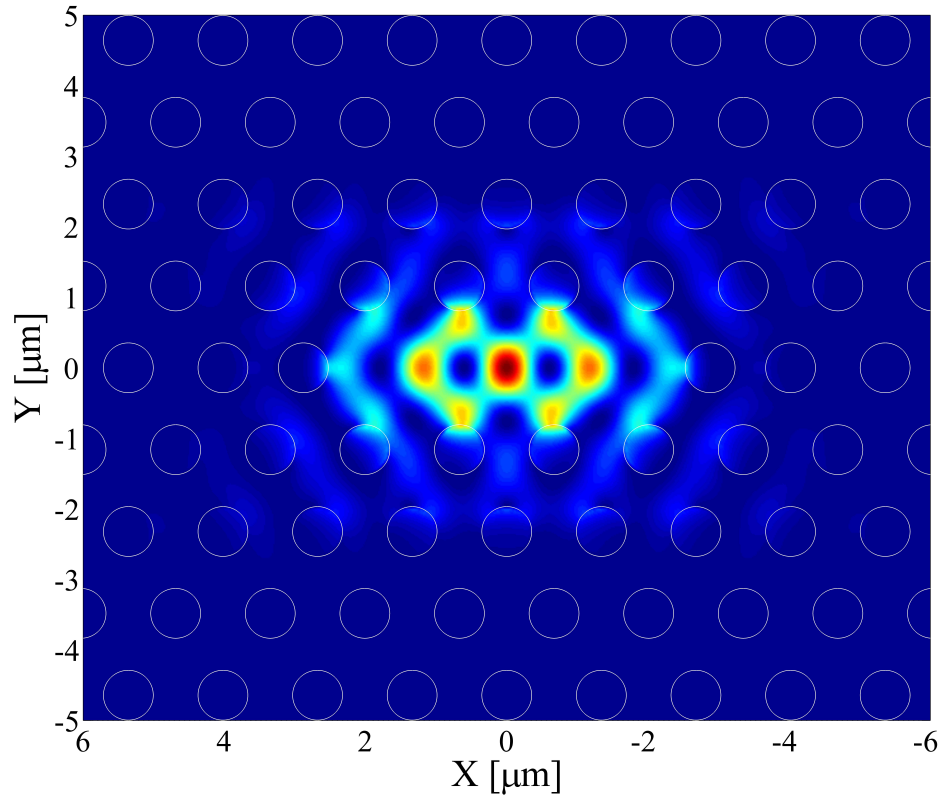
Figure 2.1.2: Mode profile of E_y field component of L3 photonic crystal cavity with a = 1.34 µm, r= 0.263a, t = 0.5 µm, and hole shift s = 0.15a, with resonance wavelength λ = 4.604 µm and Q = 24,000.
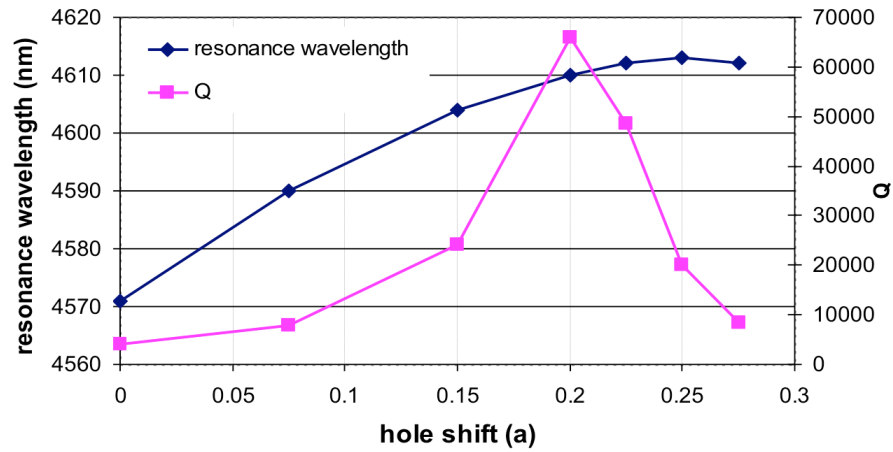
Figure 2.1.3: Results of FDTD calculations showing L3 photonic crystal cavity resonance wavelengths and quality factors as a function of *s*, the hole shift.

longer wavelengths, due to the increase in high-dielectric material in the cavity region. We could have designed our structures to have even higher quality factors, but chose moderate Q-factors so that locating the modes experimentally would not be especially challenging.

2.2 FABRICATION

The photonic crystal cavities were fabricated on a silicon-on-insulator (SOI) substrate (SOITEC Inc.), with a device layer thickness of 500 nm and SiO_2 buried oxide (BOX) layer thickness of 3 μm. ZEP (Zeon Corp), a positive electron-beam resist, was used as a mask for electron-beam lithography. The patterns were then transferred into the silicon via inductively-coupled plasma reactive ion etching (ICP-RIE), and then undercut using a 5:1 buffered oxide

etch for 45 minutes. A scanning electron micrograph of a completed device is shown in Figure 2.2.1. Details of the sample preparation, e-beam lithography, and ICP-RIE processes are given below.

2.2.1 PATTERNS FOR E-BEAM LITHOGRAPHY

Patterns were generated in Design CAD and AutoCAD. Due to the proximity effect, hole radii needed to be shrunk by about 25% to obtain the correct dimensions in fabrication.

2.2.2 SAMPLE PREPARATION FOR E-BEAM LITHOGRAPHY

Steps for sample preparation:

- ultrasonicate in acetone for 5 minutes

- ultrasonicate in isopropyl alcohol (IPA) for 5 minutes

- bake on 180°C hotplate for 10 minutes

- clean in O_2 plasma stripper, 2 minutes (O_2 flow rate: 20 sccm, power: 80 W)

- spin ZEP-520A e-beam resist on sample at 2000 rpm (usual resist thickness after spin: 550 nm)

- post-spin bake: 180°C hotplate for 3 minutes

2.2.3 E-beam lithography (ELS-7000)

The patterns were written in the Elionix ELS-7000 tool at the Center for Nanoscale Systems (CNS) at Harvard University. A write field size of 300 μm was used, with 60,000 dots. The current used was 100 pA, with a dosage range from 375 μC/cm^2 to 425 μC/cm^2. After writing, the samples were developed in o-xylene for 40 seconds, and then rinsed in IPA and blow-dried using N_2.

2.2.4 Reactive ion etching

The patterns were transferred to the mask using the STS ICP-RIE tool at CNS. A 6" Si wafer was used as a carrier, and thermal paste was used to provide good thermal conductivity between the sample and the carrier wafer. Two recipes were used for the dry etching: the first (Recipe 1), to etch the Si device layer, and the second (Recipe 2) to etch both Si and the BOX layer. Parameters for both recipes are given below. To clean the etching chamber, an O_2 clean is run for 20 minutes, followed by a 10 minute precondition using Recipe 1. For the purpose of etch rate determination, a Si wafer with lines patterned in Shipley photoresist was then etched using Recipe 1 for 2 minutes. The photoresist on the etch test wafer was then removed using ultrasonication in acetone and IPA. The Dektak profilometer tool was then used to determine the etch depth of the lines patterned into the Si. From this etch depth, an etch rate was determined. This etch rate was then used to calculate the etch time needed to etch 550 nm of Si using recipe 1 (because the holes are smaller than the large lines in the etch test wafer, we need to over etch to make sure we go through the entire device layer). Then we etched using Recipe 2

Table 2.2.1: Recipe 1

Gas	Value
C_4F_8	80 sccm
SF_6	130 sccm
Platen power	12 W
RF Power	1000 W

Table 2.2.2: Recipe 2

Gas	Value
C_4F_8	30 sccm
SF_6	65 sccm
H_2	15 sccm
Platen power	17 W
RF Power	1000 W

for 40 seconds. This is done to prevent undercutting of the Si layer due to the etch selectivity of Recipe 1 to silicon dioxide.

2.2.5   RESIST REMOVAL AND WET ETCHING

After dry etching, the remaining ZEP resist was removed using 8 minutes of Piranha clean (a 3:1 mixture of H_2SO_4:H_2O_2) on a hotplate at 180°C, followed by rinsing in de-ionized water 2 times. In order to release the membranes by removing the sacrificial BOX layer, the samples are placed in 5:1 buffered oxide (5:1 NH_4:HF) for 45 minutes. This is enough time to ensure that the 3 μm BOX layer is removed around the photonic crystal cavities as the BOE goes through the holes in the Si layer to attack the BOX layer. After the wet etch in BOE, the sample is rinsed twice in de-ionized water and the fabrication is complete. A

Mag = 21.48 K X   1 μm
Width = 14.06 μm   EHT = 5.00 kV   Signal A = SE2
                            WD = 16.6 mm
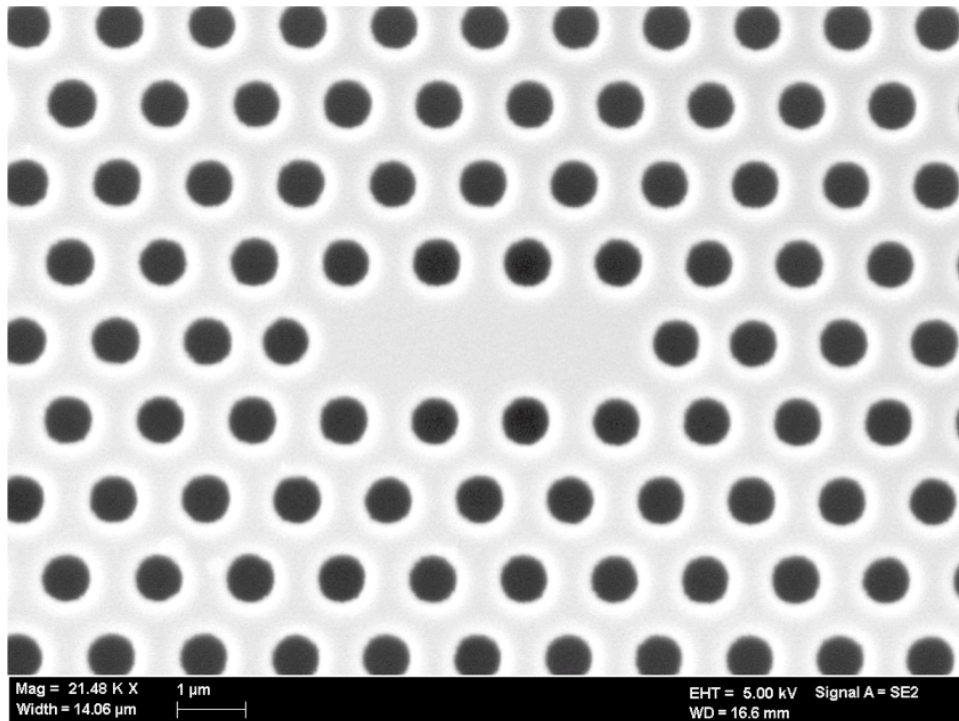
Figure 2.2.1: A scanning electron microscope (SEM) image of one of our L3 photonic crystal cavities.

scanning electron microscope (SEM) image of a characteristic photonic crystal device is shown in Figure 2.2.1.

2.3   CHARACTERIZATION

Building complex optical characterization setups for mid-IR photonic devices is probably the most challenging aspect of working at the mid-IR. Mid-IR beams are invisible, and no true viewing cards (such as those used for the telecom) exist for mid-IR beams. For rough alignment with a high intensity (mW level) beam, one can use photo-thermal paper (coated with a thin layer of heat-sensitive LCD

crystal) to detect the thermal emission from the beam. However, for finer alignment and lower-intensity beams, this method is inadequate. Additionally, commercially available quantum cascade lasers (QCLs), the light sources of choice between 4 and 20 μm, do not have fiber coupling options (at shorter wavelengths, there has been much recent promising work on ZBLAN fiber lasers [14]). Mid-IR fibers themselves are expensive and prone to degradation over a period of months. Other mid-IR optical components, such as lenses, polarizers, modulators, etc. are often quite primitive (as well as more expensive) compared to their visible and telecom counterparts. For all these reasons, we chose to concentrate our efforts on building entirely free-space setups for the mid-IR. This section will describe in detail the resonant scattering reflectivity setup we built for the mid-IR.

2.3.1 PRINCIPLE OF RESONANT SCATTERING

The resonant scattering method is a well-known free-space technique for investigating the response of photonic crystal cavities [15, 16]. In this technique, the polarization of the input signal is oriented so that the E-field of the focused input beam and the major component of the photonic crystal cavity mode (E_y) form a $45°$ angle. The laser beam is coupled into the photonic crystal cavity via an objective lens, which also captures the light re-radiated from the photonic crystal cavity through backscattering. The backscattered light is then sent through a second polarizer (called the analyzer), which is cross-polarized with respect to the input laser signal. This cross-polarization method enhances the

signal-to-background ratio of the resonantly scattered light (the signal) to the non-resonantly scattered light (the background), which is rejected by the analyzer polarizer. It is crucial to have an analyzer polarizer with a high extinction ratio for a high signal-to-background ratio. Depending on this ratio, the resonance peak can appear as a Lorentzian or a Fano lineshape caused by the phase shift between the resonant (re-emitted by cavity) and non-resonant components of the back-scattered signal. This ratio is also influenced by how tightly focused the beam is on the photonic crystal cavity region[17]. Tighter beam spots mean a higher signal-to-background ratio because more of the laser beam is focused on the defect region rather than the surrounding photonic crystal region, and hence the measured photonic crystal cavity spectrum is closer to a true Lorentzian line shape. For a larger beam spot (from a lower numerical aperture lens, for example), the signal-to-background ratio is lower and a more Fano-like line shape is measured. Spectra can be obtained either by using a broadband excitation source and a spectrometer/optical spectrum analyzer, or by using a tunable laser and a single channel detector.

We chose the resonant scattering method for a number of reasons. As mentioned previously, it is an entirely free-space method and allowed us to bypass fibers entirely. Additionally, this method does not require any gratings, couplers, waveguides, etc. to couple light into the cavities, which means a) there are fewer optical elements to fabricate and b) the cavity is entirely unloaded, which means we are measuring the intrinsic Q-factor of the cavity.

2.3.2 Techniques for mid-IR alignment

The light source for all the experiments described in this thesis is a external-cavity tunable quantum cascade laser (QCL), with continuous-wave (CW) emission from 4.315 to 4.615 μm (Daylight Solutions, Inc.), and a peak power of 200 mW. QCLs rely on intersubband transitions within a multi-layered stack of semiconductor multiple quantum well heterostructures, rather than interband transitions within a semiconductor active material, as in semiconductor lasers. Because of this, QCLs can emit at longer wavelengths than semiconductor lasers whose lasing wavelengths are determined by the material bandgap, and the wavelength of emission can be tuned over a broad range by changing the components of the stack. QCLs can achieve room temperature, continuous-wave (CW) emission of over 2W [18] over much of the mid-IR. We chose to work at 4.5 μm because of the availability of high-power QCLs at this wavelength (partially due to its location within the first mid-IR atmospheric window from 3-5 μm). The mode-hop free tuning range of 300 nm is achieved via an external cavity with a rotating diffraction grating providing narrowband optical feedback.

To align our QCL with the precision needed to measure the response from photonic crystal microcavities, we needed to align the laser to a visible source, which we could then use to align the rest of the optical elements in our system. In our case, we chose to align our QCL to a HeNe beam with output at 594 nm. Therefore, all the optics (lenses, mirrors, polarizers, and beamsplitters) we used needed to be operational for both mid-IR and visible light. With such a large discrepancy in wavelength between our QCL and the HeNe laser, chromatic

aberration becomes an issue, and we tried to minimize the number of refractive elements in our setup because of this. Au-coated mirrors were used rather than Ag-coated mirrors due to their higher reflectivity in the mid-IR.

Using two Au-coated mirrors mounted on tip-tilts, we aligned our mid-IR laser light onto a PbSe mid-IR detector (Thorlabs) placed almost a meter away from the laser head (photo-thermal paper was used to help locate the beam initially). The position of the laser beam was adjusted using the tip-tilts until the signal was maximized on the detector. Next, an iris was placed along the beam path halfway between the laser and the detector, in order to provide a second point for alignment (the detector is the other point). By monitoring the signal on the detector as half the iris opening was blocked in both horizontal and vertical directions, we were accurately able to center the iris in the beam path. Then, the HeNe beam was introduced into the setup via a beamsplitter and a flip-mounted Ag mirror, both of which were housed in tip-tilt mounts. Using the tip-tilt positioners, we were able to guide the HeNe beam through the iris and onto the detector. Since the HeNe beam and the QCL were now aligned at 2 points over a long distance, we considered the two beams aligned and then used the visible beam to align the rest of the optics. As we built more and more of the setup, we placed the PbSe detector along the beam path of the HeNe to check for mid-IR signal to ensure good alignment between both beams.
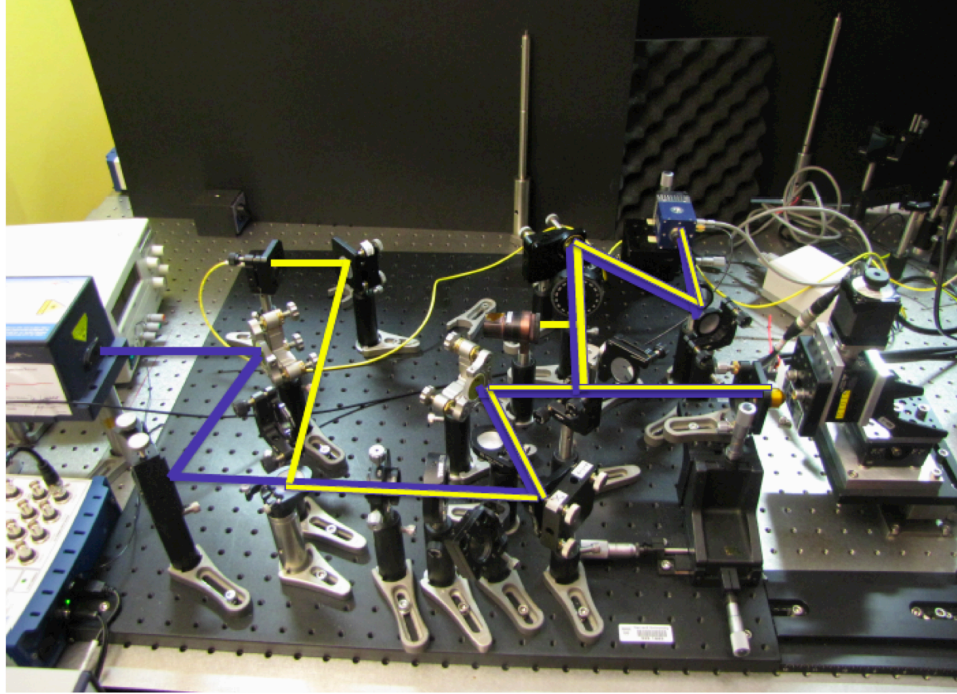
Figure 2.3.1: A photograph of the resonant scattering setup used to measure photonic crystal cavity spectra. The blue line indicates the QCL beam path; the yellow line indicates the HeNe beam path.

2.3.3 MID-IR RESONANT SCATTERING SETUP

Having aligned the mid-IR and HeNe beams to each other, we then proceeded to build the resonant scattering setup. As discussed in Section 2.3.1 , the basic principle of resonant scattering is cross polarization, so it is important to have a good extinction ratio between the two polarizers. We chose nano particle polarizers from Codixx AG for their 10,000:1 extinction ratio in the mid-IR. The laser output is horizontally polarized, but we still use a polarizer at the input in order to remove any vertically polarized components in the beam.
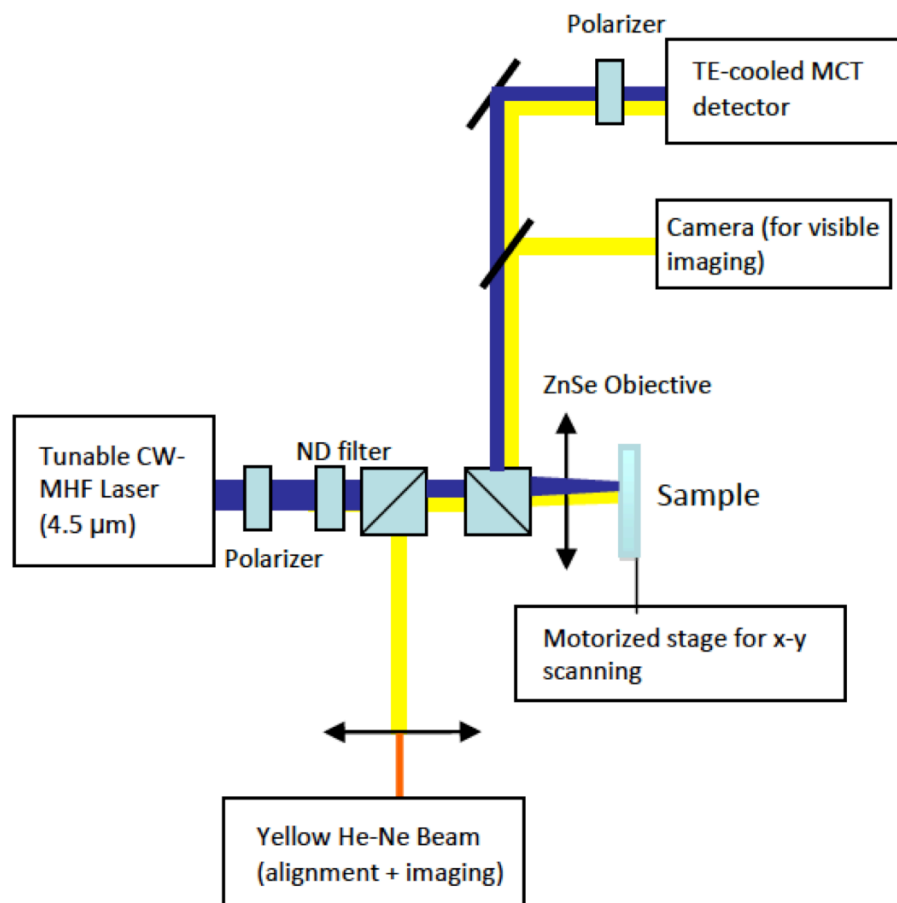
Figure 2.3.2: A schematic diagram of the resonant scattering setup used to measure photonic crystal cavity spectra. The blue line indicates the QCL beam path; the yellow line indicates the HeNe beam path.

Using Au-coated mirrors mounted on tip-tilts, the QCL beam is steered through a pellicle beamsplitter coated for 3-5 μm (Thorlabs), and then into a ZnSe objective lens (Innovation Photonics), with numerical aperture (NA) of 0.22, that focuses light onto the sample. The sample is mounted on an automatic micropositioner stage that can be scanned using computer control. More detail about this scanning functionality is provided in Section 2.3.5. The photonic crystal cavities are e-beam written at a $45°$ angle on the sample so that the cavity mode polarization is oriented at $45°$ with respect to the horizontally-polarized E-field of the laser spot. The light that is coupled and re-emitted by the photonic crystal cavities is backscattered into the ZnSe objective. This beam is then directed via the beamsplitter into the second polarizer (the analyzer) which is cross-polarized with respect to the input polarizer, before being focused by a BaF_2 (ISP Optics) lens onto a thermoelectrically cooled mercury cadmium telluride (MCT) detector (Vigo). A photograph of the setup is shown in Figure 2.3.1, with a schematic of the setup shown in Figure 2.3.2.

2.3.4   Experimental results

The experimental results for photonic crystal cavities with 10 mirror hole pairs are shown in Figure 2.3.3. Photonic crystal cavity modes are found within the range of 4.38 to 4.42 μm. As predicted by theory (Figure 2.1.2), the cavity resonance wavelengths redshift as the air hole shift s is increased from zero to a maximum of $s = 0.225a$ (Figure 2.3.3). The Q-factors also roughly follow the trend predicted by theory. A peak Q-factor of 13,600 is found for $s = 0.15a$, representing what was
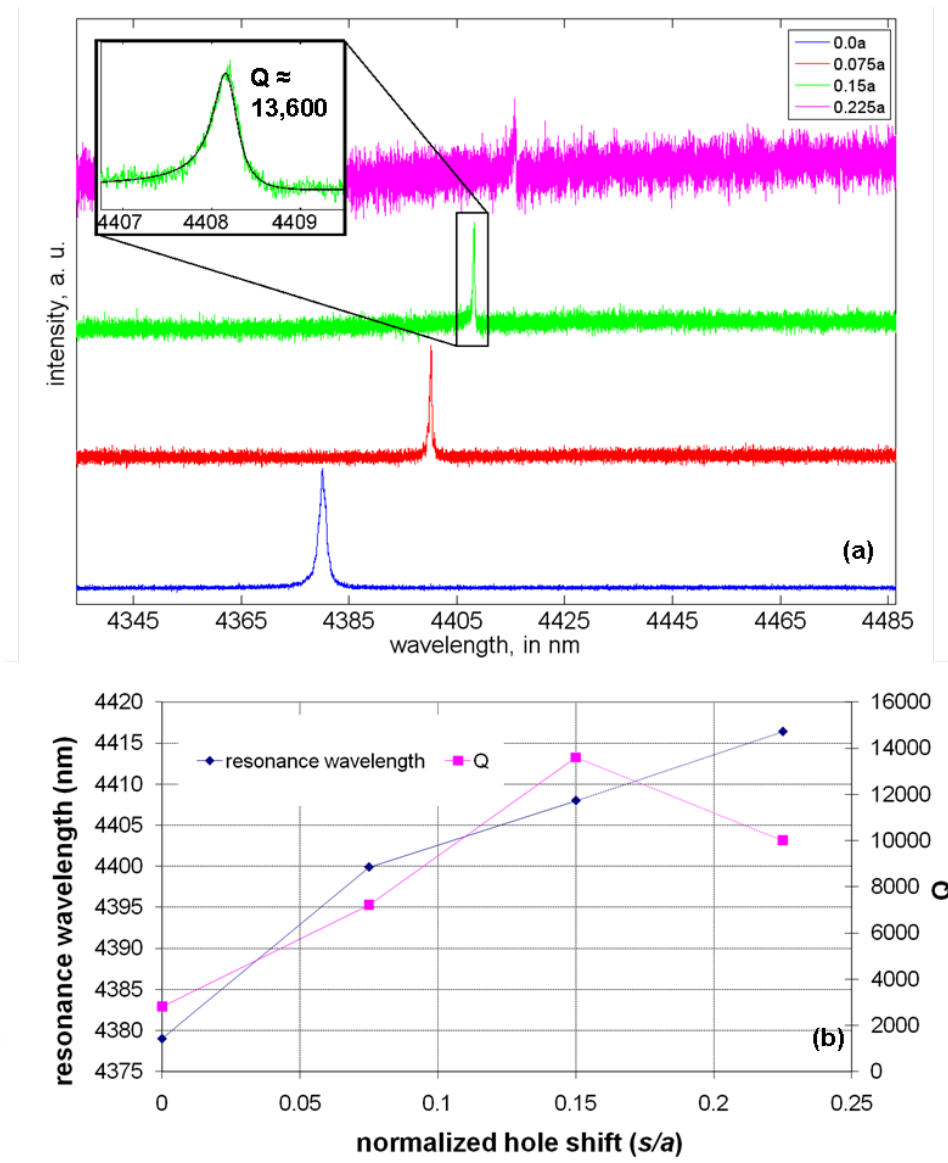
Figure 2.3.3: (a) Resonant scattering spectra of photonic crystal cavities with $s = 0$, $s = 0.075a$, $s = 0.15a$, $s = 0.225a$. Scale is linear. Inset shows Fano fit to $s = 0.15a$ cavity. Fitting parameters are A_o = 5.6e-5, q = 2.52, Γ = 5.0 GHz, f_o = 68 THz, and F_o = 0.0013. Cavity with s = $0.2a$ did not show a resonance. (b) resonance wavelength and Q vs. s for measured cavities. A peak Q of 13,600 is measured at 4408 nm. Lines between points are there to guide the eye.

at that time the highest Q factor measured for any Si-based optical cavity in the mid-infrared (Figure 2.3.3b). The inset in Figure 2.3.3 shows the measured Fano lineshape of the resonance along with the theoretical fit F(f) [13] given by:

$$F(f) = A_{\mathrm{o}} + F_{\mathrm{o}}\frac{[q + 2(f - f_{\mathrm{o}})/\Gamma]^2}{1 + [2(f - f_{\mathrm{o}})/\Gamma]^2},\qquad(2.1)$$

where A_{o} and F_{o} are constants, q is the Fano parameter, f_{o} is the cavity mode frequency, and Γ is the linewidth. The fit is plotted in terms of the wavelength $\lambda = c/f$, where c is the velocity of light. We extract the quality factor from the ratio of f_{o} to Γ. In the case of the $s = 0.15a$ cavity, the extracted linewidth was 5.0 GHz with a f_{o} of 68 THz. In the $s = 0.2a$ cavity we did not detect a resonance (the reason for this will be discussed in Chapter 4). In order to improve signal-to-noise ratio in our experiments, we can increase the excitation power of our laser. However, when the QCL output power was increased to 100 mW (only about 3-5% of this power gets coupled into the cavity), we noticed the evidence of optical bistability in our photonic crystal cavities [19], as seen in Figure 2.3.4. We will explore this bistability further in Chapter 4.

2.3.5 Scanning resonant scanning microscopy

In order to further confirm that the observed resonances are indeed associated with cavity modes, it is important to visualize their spatial profiles. However, since no true viewer cards exist for the mid-IR wavelength range, and mid-IR cameras are rather expensive, we adapted the scanning-confocal microscopy
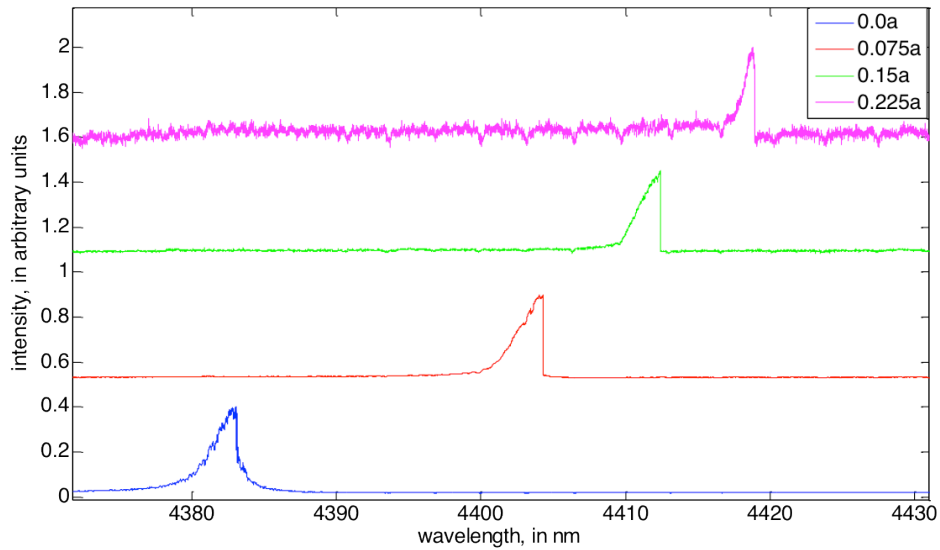
Figure 2.3.4: (a) Resonant scattering spectra of the same photonic crystal cavities in Figure 2.3.3, taken at higher power. Bistable line shapes are clearly seen, especially for the higher Q-factor devices.

approach to image our devices [20]. We call this method scanning resonant scattering microscopy. A single mid-IR detector is used, and the spatial profile is obtained by scanning the sample in x- and y-direction using computer-controlled micropositioners. In order to locate the cavities, we scan the sample stage in both x- and y- directions at an arbitrary wavelength. The outlines of the cavities can be made out at all wavelengths, so we can then move to the center of the photonic crystal cavity region and sweep the laser in wavelength in order to obtain a resonant scattering spectrum. This procedure allows us to precisely position the laser beam onto our cavities. Furthermore, we can obtain the image of the cavity resonance by tuning the laser to the cavity resonance and moving the sample holder stages in the x- and y-directions and recording the detector reading at each
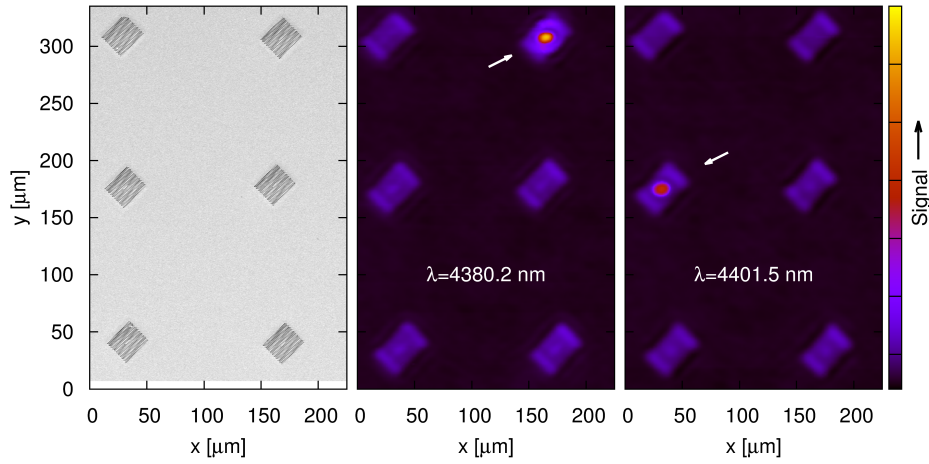
Figure 2.3.5: Mid-infrared scanning resonant scattering image of an array of 5 cavities (upper left hand structure is photonic crystal with no cavity). Scanning electron micrograph is provided for comparison. When our laser is tuned to one of the cavity resonances, and scanned over the cavity array, only the cavity in resonance with the laser lights up. For example, when 4380.2 nm light, corresponding to the resonance of the top right cavity in the center panel, is scanned over the array, only that cavity appears "ON", featuring a bright spot in its center. Alternatively, when the laser is tuned to 4401.5 nm and scanned over the array, only the middle-left cavity (rightmost panel) resonates.

position. Images obtained using this approach are shown in Figure 2.3.5. It can be seen that the cavity regions light up at the wavelengths corresponding to the resonance peak in the wavelength scan, and remain dark off-resonance, confirming that the peaks we see in the wavelength scans do indeed correspond to L3 photonic crystal cavity modes. In effect, this imaging approach can be seen as a single-pixel mid-infrared camera, allowing for the visualization of fabricated structures and resonant modes without the use of extremely expensive mid-IR cameras.

In Figure 2.3.6, we show a spectrum and scanning mid-IR images of additional
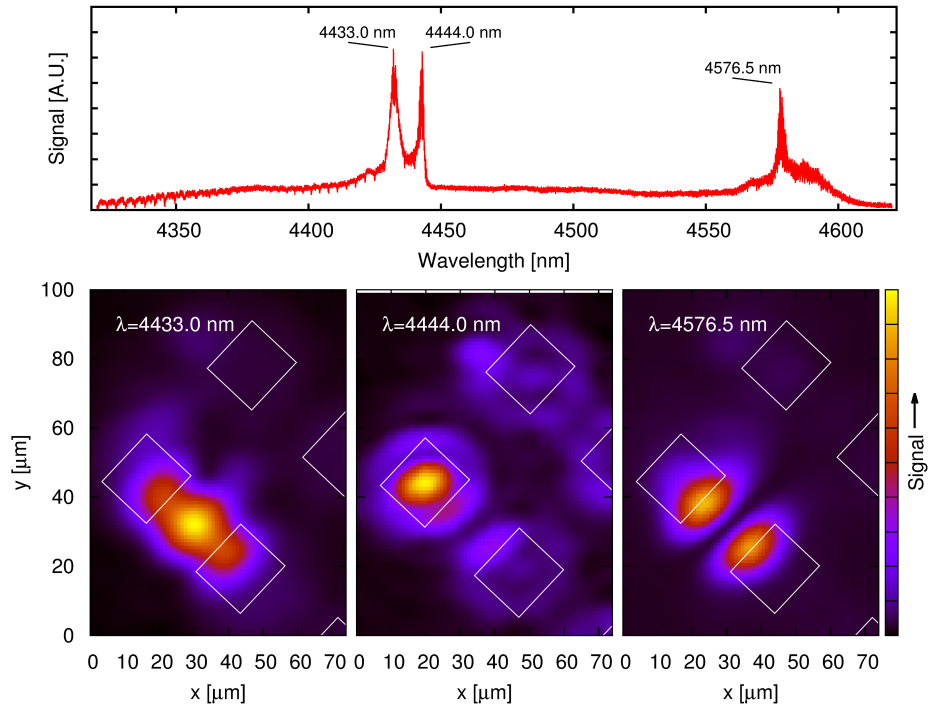
Figure 2.3.6: Resonant scattering spectrum showing peaks corresponding to two inter-cavity Fabry-Perot resonances (4430.0 nm and 4567.5 nm) and one L3 photonic crystal cavity resonance (4444.0 nm). (b) scanning images of Fabry-Perot resonances (leftmost and rightmost panels) and photonic crystal cavity resonance (center panel).

resonances that were observed in our four-mirror hole pair devices. These devices were placed relatively close together, with a separation of 22 μm in the y-direction. Resonant scattering spectra of these cavity devices show two extra peaks appearing (at 4.433 μm and 4.567 μm) in addition to the cavity resonance peak (4.444 μm). Using our scanning resonant scattering microscopy technique, we were able to image these modes and attribute them to the inter-cavity resonances of the Fabry-Perot cavity formed between two adjacent photonic crystal structures (Figure 2.3.6b): one resonance has an anti-node (leftmost panel, 4.433 μm) and the other one has a node (rightmost panel, 4.567 μm) in the center of the inter-cavity region. The resonance at 4.444 μm (center panel in Figure 2.3.6b) corresponds to a bonafide resonance of the L3 photonic crystal cavity.

The ability to accurately image the spatial profile of resonances observed in the collected spectra, and therefore unambiguously attribute them to the modes of different cavities, is an important demonstration of the utility of the mid-IR scanning resonant scattering microscopy that we developed. The combination of scanning microscopy and resonant scattering wavelength measurements results in a very powerful tool that overcomes many of the difficulties inherent in working at the mid-IR. Iterating between scanning microscopy and wavelength scanning allows us to optimize our resonant scattering spectra signals more quickly and accurately than we would be able to with only a visible-wavelength CCD camera sensitive to visible wavelengths to guide us as to the location of our cavities. We see scanning resonant scattering microscopy as an essential tool in a mid-IR toolbox.

2.4   CONCLUSION

In conclusion, we have demonstrated the design, fabrication, and characterization of silicon-based photonic crystal cavities for the mid-infrared, with a peak quality factor of 13,600. Additionally, we have transferred experimental techniques used at telecommunication and visible wavelengths, most notably resonant scattering and scanning confocal microscopy, to characterize our mid-IR cavities. Further work will be focused on achieving higher quality factor cavities and in coupling mid-IR photonic crystal cavities to waveguides so that the vision of on-chip integrated photonics in the mid-infrared can be attained. Such a fully integrated platform would enable realization of chip-scale systems for trace gas sensing, optical-wireless, on-chip optical interconnects, phased-arrays for LIDAR applications, and so on.

3

Electro-Optic Tuning of Mid-IR Photonic Crystal Cavities Using Graphene

The mid-infrared (MIR) wavelength range (2-20 μm) is of great interest for a wide range of applications, from trace gas sensing to thermal imaging. Due to

silicon☒s high transparency through much of the mid-IR, much recent work has focused on developing passive optical components for the mid-IR such as waveguides and microresonators [11, 21–23]. Additionally, Si photonic components such as supercontinuum sources, parametric amplifiers, wavelength conversion devices, etc. have also been developed. However, to truly access on-chip applications at these wavelengths, on-chip Si modulators will be needed. Recently, on-chip electro-optic modulation at MIR wavelengths in a silicon platform, at 2.165 μm, was demonstrated for the first time[24]. However, this modulator employs free-carrier dispersion as a mechanism for modulation, whereas at higher wavelengths ($\lambda > 3$ μm), free-carrier absorption dominates over free-carrier dispersion.

Graphene holds great promise as a method for MIR on-chip modulation at higher wavelengths, since its optical properties can easily be controlled by the gate voltage, potentially at high speeds[25]. Electro-optic modulation in a graphene-covered waveguide has already been demonstrated at telecom wavelengths[26], but graphene photonic crystal cavity-based modulators would allow for greater interaction between the graphene and the optical field, decreasing the modulator footprint. A photonic crystal cavity-based modulator operates if the cavity resonance can be shifted off and on by an incoming optical signal. Modification of a photonic crystal cavity response using the electrical gating of graphene via electrolyte has been shown around 1.5 μm [27, 28]. Here, we present our results on electro-optic modulation of Si photonic crystal cavities at the mid-infrared based on the direct gating of graphene. A wavelength tuning

range of 4 nm is demonstrated around a wavelength of 4470 nm, showing the feasibility of on-chip electro-optic modulation at the mid-IR, as well as on-chip tunable filters.

3.1 OPTICAL PROPERTIES OF GRAPHENE

Graphene has several interesting optical properties, due to its two-dimensional structure and linear dispersion, which creates a very low density of states near the Dirac point. Because of this, small variations in carrier density, achievable through electrical gating, can cause considerable shifts in the Fermi energy E_F[29]. Graphene is well-known to have a constant absorption at normal incidence throughout the visible and infrared of about 2.3% [25], but this absorption can be tuned via electrical gating due to the shift in E_F. If E_F is shifted by more than half of an incident photon's energy $\hbar\omega/2$ from the Dirac point, the interband transition for that photon will be blocked, leading to reduced absorption and hence greater transmission at the frequency ω [28]. Gate-variable optical transitions in graphene are of great interest for high-speed modulators and detectors with small footprint and ultra-wide bandwidth.

3.2 FABRICATION

Our devices, as shown in Figure 3.2.1, consist of suspended L3 photonic crystal cavities (PhCs) fabricated in a silicon-on-insulator (SOI) platform as described in Chapter 2, in contact with a graphene field-effect transistor (FET). A thin (30
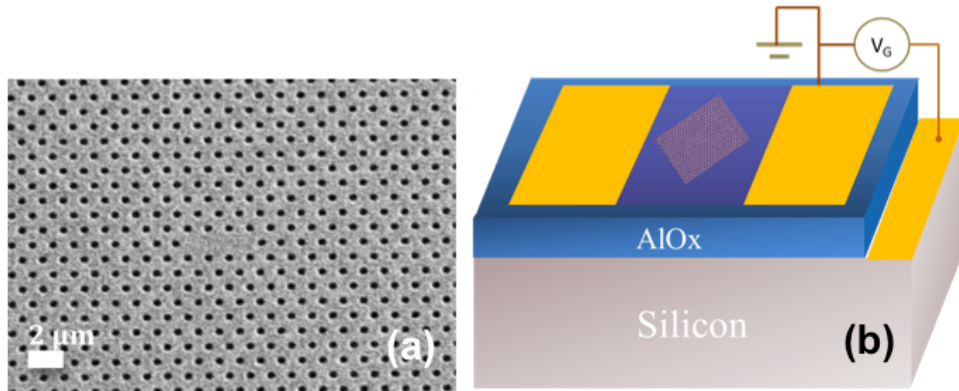
Figure 3.2.1: (a) A scanning electron micrograph of the graphene-covered photonic crystal cavity. (b) schematic of graphene field-effect transistor integrated with photonic crystal cavity.

nm) layer of alumina is deposited on top of the PhCs in order to prevent the Si membrane from being gated directly. Atmospheric pressure chemical vapor deposition-grown graphene is transferred onto the PhCs [30]. Metal contacts on the graphene are fabricated by evaporating palladium (10 nm; chosen for its low contact resistance with graphene) and gold (30 nm) on the sample using e-beam evaporation and then patterning via e-beam lithography and liftoff. Unnecessary graphene was removed via photolithography and oxygen plasma etching. Ti/Au pads (20 nm of Ti, 300 nm of Au) for probing/bonding purposes are patterned by photolithography and liftoff. The alumina gate oxide is selectively removed and Ti/Au gate contacts are placed on the sample via e-beam evaporation. Finally, we wire bond the devices of interest so gate voltages can be applied to the graphene.

We performed electronic characterization of our device by applying a voltage between the two contact pads and measuring the conductance (not shown). The charge neutral point (CNP), where the hole and electron concentrations are

34
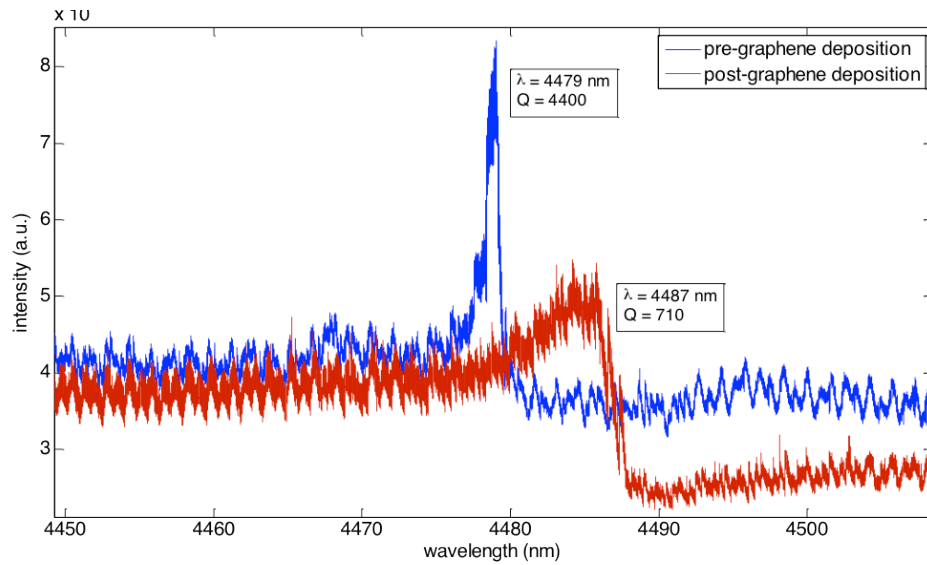
Figure 3.3.1: Resonant scattering measurements of a characteristic photonic crystal device before and after graphene transfer. The Q-factor before deposition is 4400; after graphene deposition, it decreases to 710, and the overall reflectivity declines due to the absorptivity of graphene. The change in resonance wavelength post-graphene transfer was not consistent from device to device.

equal, is at about 2 V. We see asymmetry around the CNP, likely due to the fact that the Pd-Si junction is not ohmic. Because of this, we chose to use negative bias voltages, as the conductance as a function of gate voltage has a higher slope on this side.

3.3   DEMONSTRATION OF ELECTRO-OPTIC TUNING

We used a cross-polarization reflection setup [11] to measure the reflectivity response of our devices, using a quantum cascade laser (Daylight Solutions, Inc.) with emission from 4.3-4.6 μm as our source. A thermoelectrically-cooled

mercury cadmium telluride (MCT) detector is used to collect the light.

Figure 3.3.1 shows the response of one of our photonic crystal cavities before and after graphene deposition. The quality (Q) factor of the PhC before graphene transfer was measured to be about 4400; after graphene is transferred onto the sample, the Q-factor declines to about 700, and the overall reflectivity declines due to the absorptivity of graphene. The shift in the resonance wavelength post-graphene transfer was not consistent from device to device. All spectra are fitted with a Fano lineshape in order to extract the cavity resonance wavelength and Q-factor [11, 17].

We then applied a gate voltage to the graphene using a source meter (Keithley). Our gate voltage was limited to a maximum of 8V, due to the breakdown of our gate oxide at higher voltages. As the gate voltage we apply becomes smaller and smaller than the charge neutral point voltage (VCNP, 2V in our samples), the cavity resonance blueshifts, due to the increase in carrier density in graphene and resultant decrease in permittivity (Figure 3.3.2). The effective refractive index of the photonic crystal slab becomes smaller as the graphene permittivity decreases, and thus the cavity resonance blue shifts.

A maximum tuning range of 3.8 nm around 4470 nm is achieved, which agrees well with FDTD simulations (Figure 3.3.3b). We simulate the effect of gated-graphene on our devices by calculating the permittivity as a function of charge carrier concentration using the random phase approximation[31](Figure 3.3.3a), and then using perturbation theory to model

36
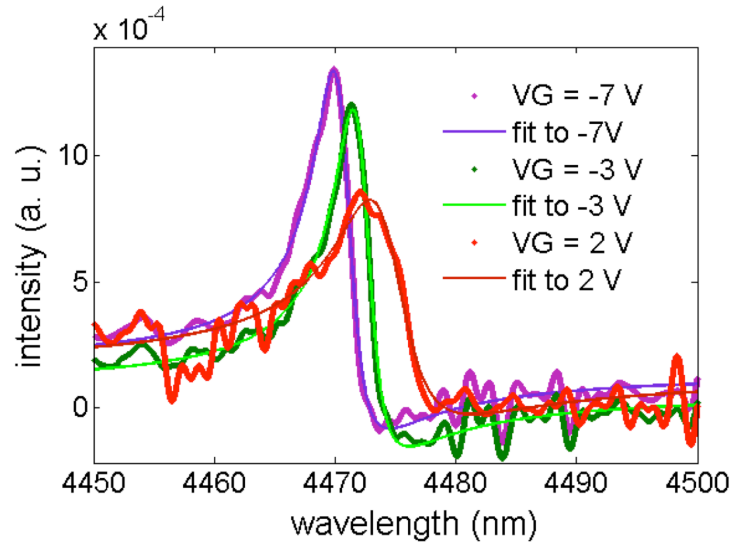
Figure 3.3.2: Resonant scattering spectra of our devices at three gate voltages: V_G = 2V, V_G = -3V, V_G = 7V. As the gate voltage becomes smaller and smaller than the charge neutral point (V_{CNP} 2V in our samples), the cavity resonance blueshifts, due to the increase in carrier density in graphene and resultant decrease in permittivity

the effect of this permittivity change on our photonic crystal cavities. In Figure 3.3.3b, we show both the calculated and experimentally measured dependences of the resonance wavelength shift on the gate voltage. The hysteresis seen in Figure 3.3.3b for the experimentally measured data is likely due to charge trapping due to the exposure of graphene due to air [32].

We also observed modulation of Q factor as the gate voltage changes (Figure 3.3.4). As the gate voltage decreases from 0V to -3V, the interband transition is blocked, leading to a decrease in the light absorption of the graphene (Pauli blocking) and subsequent increase in the Q-factor of the cavity. The Q-factor is relatively stable after the -3V point, due to full Pauli blocking being achieved. The highest Q-factor of 1350 is achieved at -3V, at a resonance
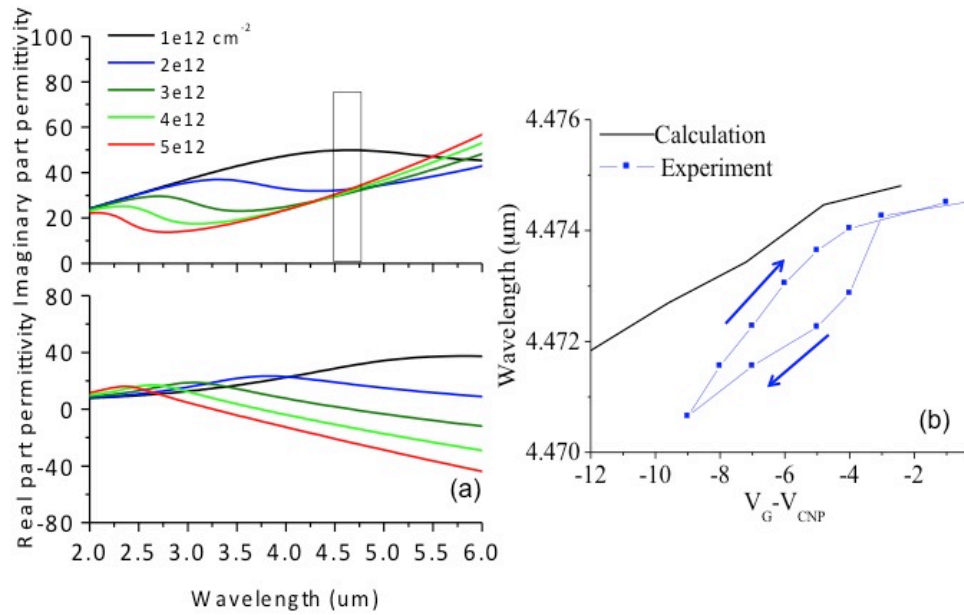
Figure 3.3.3: (a) Real and imaginary parts of the graphene permittivity calculated with the random phase approximation[31]at a temperature T = 300 K for different carrier concentrations in single layer graphene. (b) Resonance wavelength shift as a function of gate voltage, from experiment (blue), and simulations (black). The hysteresis in the experimentally measured data is likely due to environmental factors.
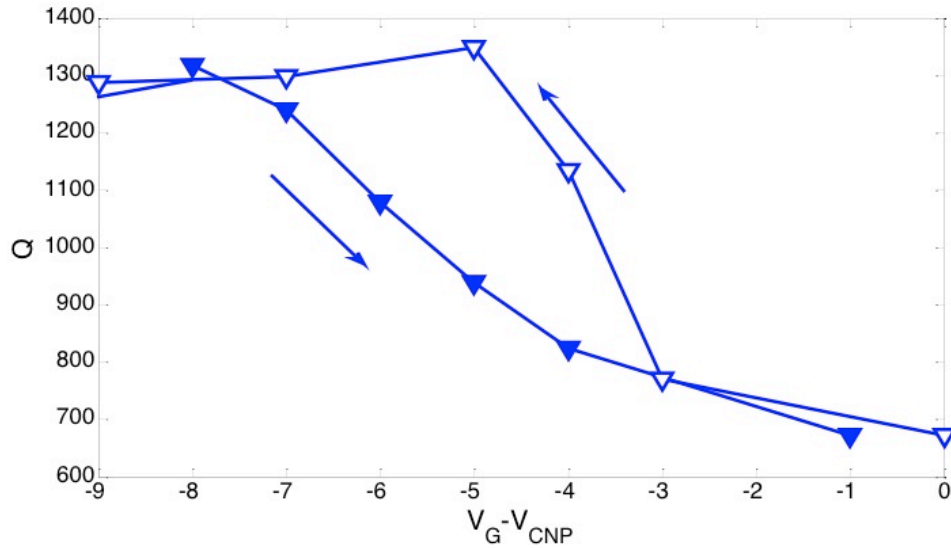
Figure 3.3.4: Measured values of the Q-factor of our devices as a function of gate voltage. The highest Q-factor of 1350 is achieved at V_G= -3V at a resonance wavelength of at 4472.3 nm, representing a Q factor modulation of 2.

wavelength of at 4472.3 nm, representing a Q factor modulation of 2. However, the graphene does not achieve full transparency, as the original Q is not recovered. This residual graphene absorption may be due to the presence of mid-gap states and electron-phonon coupling [28, 33]. Additionally, as the Q-factor increased to about 1000, we saw the evidence of optical bistability in the measured lineshapes (Chapter 4)[34]. Thus, all measurements shown here were taken at low power, below the bistability threshold, so as to remove the effect of thermal-broadening on our cavity resonances.
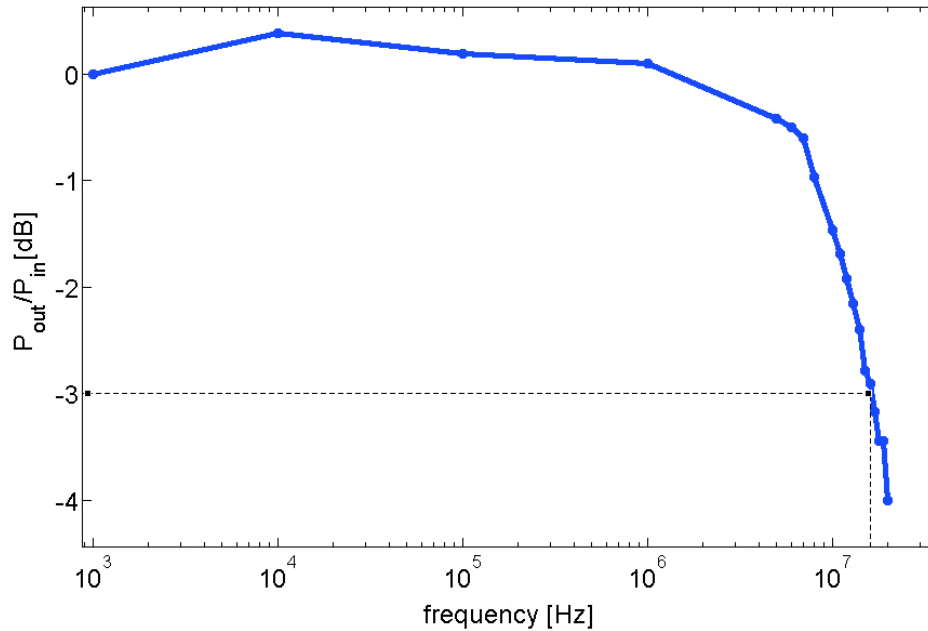
Figure 3.4.1: Electronic frequency response of our device in response to gate modulation. We deduce a cut-off frequency of about 16-17 MHz.

3.4 MODULATION MEASUREMENTS

Since one of our major interests in graphene-silicon photonic crystal cavities is in their potential use as mid-IR on-chip modulators, we decided to determine the limit of the modulation speed attainable in our devices. Future devices may involve waveguide integration so that a transmitted signal is modulated, but here we look at the optical modulation of reflectivity. Unlike the work done by Majumdar et al.[27] and Gan et al.[28], we did not use ionic gels, which have notoriously slow response speeds (on the order of 1 kHz[35]), to gate our graphene, so we expected modulation speeds in the MHz for our devices. First, we measured the maximum modulation speed of the gated graphene directly, by
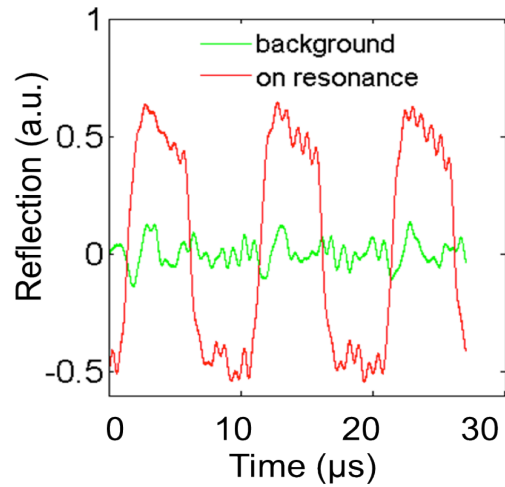
Figure 3.4.2: Modulation of optical reflectivity signal at 100 kHz. We fix the laser wavelength at 4470 nm, which corresponds to a location with strong modulation depth, and modulate our gate voltage from -6 to 2V (red curve). The green curve is taken at a wavelength of 4450 nm, off the resonance of the cavity. No modulation is seen at this wavelength.

applying a sine wave signal from a function generator (with maximum frequency 20 MHz) as the gate voltage for the device, and monitoring the frequency response of the modulation voltage amplitude on an oscilloscope. The result of this measurement is shown in in Figure 3.4.1. The cut-off frequency, where the signal drops to -3 dB, is deduced to be about 16 MHz from this measurement, a value consistent with other graphene-silicon devices[31].

Next, we monitored the optical reflectivity signal as we modulated the gate voltage via the function generator. We fix the laser wavelength at 4470 nm, which corresponds to a location with strong modulation depth, and modulate our gate voltage from -6 to 2V. Signal from our detector was sent into a pre-amplifier before being sent into the oscilloscope, in order to boost the signal levels. Results

from modulation at 100 kHz are shown in Figure 3.4.2 (red curve is on resonance). We also modulate the gate voltage while having the laser wavelength tuned to 4450 nm (off resonance, in green), in order to verify that the effect we are seeing is due to gating of graphene. In this optical modulation experiment, our cut-off frequency was about 200 kHz, a much slower cut-off speed than in the gate voltage experiment. The reason for this discrepancy is unknown, but we speculate that it may have to do with thermal effects, or other processes that affect the structure optically, that may have a shorter time constant than the time constant of the electronic device alone. More investigation into this discrepancy is needed. We also expect that significantly higher modulation speeds can be attained by patterning the graphene to reduce its RC constant and by using highly p-doped Si for the photonic crystal cavity.

3.5 Conclusion

In conclusion, we have demonstrated electrical tuning of mid-infrared Si PhCs using the electrical gating of graphene. A wavelength tuning range of almost 4 nm is achieved over a gate voltage range of 9V, which shows these devices hold promise for on-chip electro-optic modulation. Additionally, these devices can be used for any applications that require tunable narrow-band filters. Further work needs to be done in order to increase the modulation speed of our devices and to make waveguide-integrated devices.

4

Optical Bistability in Mid-Infrared Photonic Crystal Cavities

Optical bistability in Si microresonators is a well-known phenomenon at telecommunications wavelengths[19, 36–39]. Since the refractive index of Si can

change either directly or indirectly due to incident light intensity, the resonance wavelength of a microresonator also changes with a buildup of optical power in the resonator. This results in a positive feedback process which allows the resonator to act as a bistable switch, with an off-resonance, or "empty" state and an on-resonance, or "loaded" state. The power dependence of the refractive index can be attributed to various effects, including the $\chi^{(3)}$ of Si, free-carrier dispersion, and the thermo-optic effect. Strong light confinement in nano-photonic devices at telecom wavelengths (e.g. 1.55 µm), and in high quality (Q) factor photonic crystal cavities in particular, results in two-photon absorption processes which lead to a pronounced thermo-optic effect due to free-carrier absorption. The high-Q factors and low mode volumes of photonic crystal microcavities lead to a low bistability threshold, with a switching energy that scales roughly with V/Q^2 [19]. This phenomenon has found use in low-power optical circuitry, as bistable photonic crystal devices can be used for optical logic gates and memory [40]. On the other hand, two-photon absorption processes and the resultant optical bistability hinder high-power density applications in Si-based photonic devices at the telecom wavelength range. However, it has recently been proposed [2, 4, 5] and demonstrated [6, 8] that Si devices operating at longer, mid-infrared (IR) wavelengths would not suffer from this problem due to the lack of two-photon absorption effects. Therefore, Si devices operating in the mid-IR could be of interest for the realization of high-power optical interconnects, as well as enable nonlinear wavelength conversion and amplification of optical signals directly in Si.

We demonstrated the operation of photonic crystal cavities in an air-bridged Si membrane platform at 4.4 μm[11], in chapter 2. In Section 2.3 of this thesis, we noted the likely presence of optical bistability in our cavities at high input powers. Here, we present an in-depth study of this effect and investigate the origin of the observed nonlinearity using time domain measurements (Sections 4.1 and 4.2). Our results indicate that the observed bistability is thermal (thermo-optic effect) in nature. We also explore the effects of standard microelectronic treatments and annealing on the bistability and Q-factors of our cavities (Section 4.3). These processes allow us to mitigate the bistability in our cavities and achieve Q-factors as high as 45,000 [34].

4.1   Fabrication and Characterization

Our devices are L3 photonic crystal cavities made in an air-bridged silicon membrane platform, with device thickness t = 500 nm (Figure 4.1.1). The basic fabrication process and device structure are detailed in Chapter 2. The hole periodicity is a =1.31 μm, and the radius is 0.259a= 339 nm. Cavities with varying hole shifts s were fabricated, with the highest Q of 13,600 being measured in an as-processed cavity with s= 0.15a at 4479.80 nm. The theoretical Q for this cavity design is Q = 34,000. We note that cavities with s = 0.2a are expected to have higher Qs of 64,000 (according to FDTD simulations), but could not be measured experimentally.

We used the resonant scattering method to couple light into our cavities via
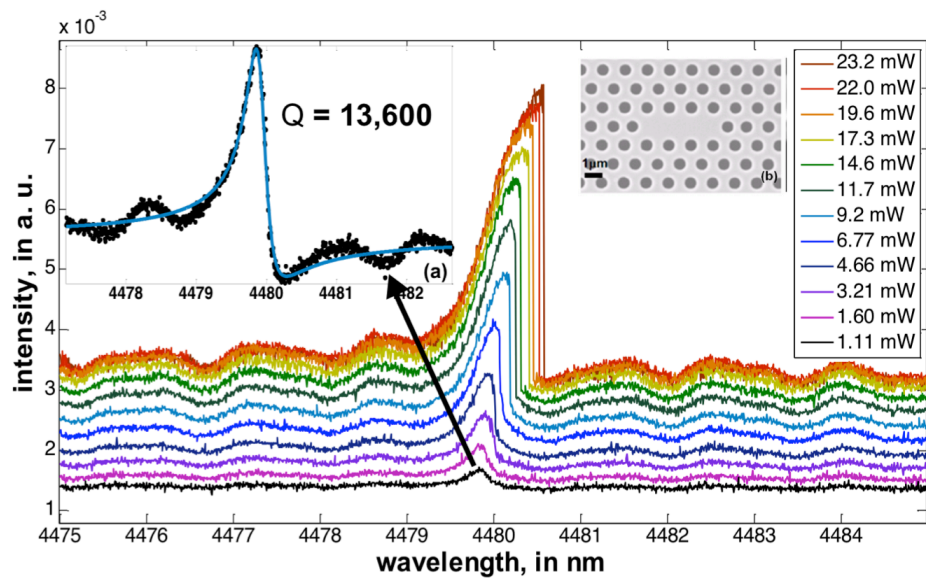
Figure 4.1.1: Cavity spectrum taken at various input powers showing characteristic bistable lineshape. Power levels given represent the power measured after the objective, before it is coupled into the device. Inset (a) shows cold cavity resonance and Fano fit to lineshape; Q = 13,600. Inset (b) shows scanning electron micrograph of one of our L3 cavities.

free-space, as described in Section 2.3. Light from a tunable quantum cascade laser (QCL) with emission from 4.315 to 4.615 μm (Daylight Solutions, Inc.) is sent into a ZnSe objective lens (N.A. = 0.22) and focused onto the sample, which is placed so that the cavity mode polarization is oriented at 45° with respect to the E-field of the laser spot.

Figure 4.1.1 shows the resonant scattering spectrum of one of our mid-IR cavities (with $s = 0.15a$), at various input powers, with the wavelength swept from shorter to longer wavelengths. A ZnSe wiregrid polarizer (Thorlabs), placed between the laser output and the input polarizer, was used as a variable attenuator in order to vary the power incident on the cavity. The power incident on the cavity was calibrated using a thermal power meter (Ophir) placed after the ZnSe objective lens. The evidence of bistability can be clearly seen at input powers over 3 mW, with the characteristic asymmetric bistable lineshape. We note, however, that the coupling efficiency of our setup is less than 20% and therefore we estimate that less than a milliwatt of incident optical power is actually coupled into the cavity. This estimation was made by calibrating our detector and by measuring power emitted from the cavity on resonance (in steady state, total in-coupled and out-coupled power are the same), taking into account the numerical aperture (N.A.) as well as the emission profile of the cavity. It is clear that in our mid-IR cavities, the bistability is due to a redshift of cavity resonance with increasing power, which as we will discuss later, narrows the possible origins of the optical bistability. The characteristic bistable lineshape is due to the fact that as the cavity is swept through red detunings from the cold cavity resonance

47
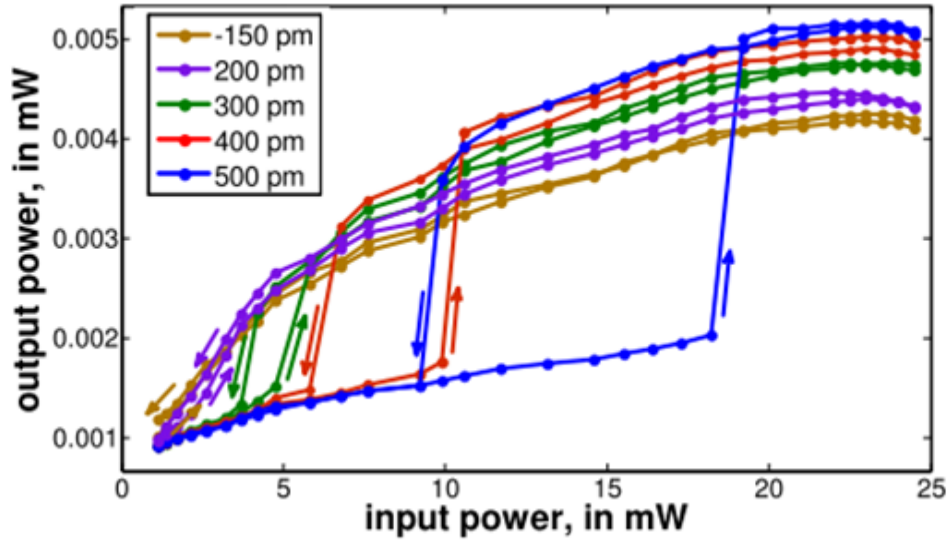
Figure 4.1.2: Power input-power output hysteresis curves. Onset of bistability is seen at a detuning of 300 pm.

(4479.80 nm); the cavity remains in a loaded state, because of positive feedback from the power-dependent refractive index, until the detuning becomes so large that the cavity transitions sharply into the empty state. As the input power increases, this effect is more dramatic, and the wavelength at which the transition occurs red-shifts. At powers below the bistability threshold of 3.2 mW, the lineshape becomes more Fano-like[17]. Using a Fano fit, we measured the Q-factor of this cavity using the spectrum taken at the lowest power, obtaining a value of 13,600.

To further study the observed bistability, we generated hysteresis curves by setting the laser at a fixed red detuning from the cold cavity resonance and measuring the input power and output power for upward and downward sweeps

of input lower power level (Figure 4.1.2)[19, 41, 42]. At detunings $\delta \geq$ 300 pm, clear bistability is seen, with the hysteresis growing with increasing δ. Again, we can see from the figure that the bistability threshold is a little over 3 mW, which is consistent with Figure 4.1.1.

4.2 TIME DOMAIN MEASUREMENTS

A variety of mechanisms can alter the effective refractive index as a function of the intensity stored inside a Si cavity. They can generally be classified into three categories: thermal effects, free carrier dispersion, and $\chi^{(3)}$ effects[42, 43]. Thermal effects occur when light is absorbed into the cavity, changing the temperature of the cavity and hence the refractive index through the thermo-optic effect, resulting in an increased refractive index and redshift of the cavity resonance. Silicon has a high thermo-optic coefficient (1.8×10^{-4} K^{-1}), so the resonance shift due to heating can be quite pronounced. Different absorption mechanisms that can lead to the thermo-optic effect include the intrinsic absorption of silicon in mid-IR (phonon-assisted absorption), various surface absorption effects, free-carrier absorption, absorption from native oxide formed on Si surfaces, and multiphoton absorption. A comparison of the intrinsic absorption of Si, free-carrier absorption and native oxide absorption is given in Table 4.2.1. Values for the absorption coefficient α are taken from literature (references provided in the table), and for the linear absorption of Si and the free carrier absorption, $Q_{absorption}$ is calculated from the well-known formula for

49

Table 4.2.1: Comparison of potential sources of absorption in our Si photonic crystal cavities at 4.5 μm

Source of Absorption	a (cm^{-1})	$Q_{absorption}$
Linear absorption of Si[2]	0.004	1×10^7
Free carrier absorption [45] (n-type doping, ρ=50 Ω.cm)	0.002	2.4×10^7
Native oxide growth (4 nm) [46]	9.8	1.8×10^6

material-limited absorption:

$$Q_{absorption} = \frac{2\pi n}{\lambda a} \tag{4.1}$$

where n is the refractive index of Si at 4.5 μm and λ is 4.5 μm. $Q_{absorption}$ for 4 nm of native oxide [44] is estimated from perturbation theory and also from FDTD calculations.

Multiphoton absorption is unlikely at this wavelength, as at least 4 photons are needed to overcome the Si bandgap energy. Free carrier absorption, either from carriers generated via multiphoton absorption or from carriers introduced by doping of the wafer is also unlikely: (i) our highly resistive Si wafer (ρ=50 Ω.cm) has a loss constant of a < 0.002 cm^{-1} at 4.5 μm [45], which cannot explain the amount of heating that we observe. The $Q_{absorption}$ due to free carrier absorption, 2.4×10^7, is too large to contribute to the losses we see. (ii) free-carrier generation by multi-photon (four-photon) effects is unlikely. Similarly, the linear absorption of Si, comparable to free-carrier absorption ($Q_{absorption}$ = 1×10^7), cannot explain our results. Free carrier dispersion results in a blue-shift of cavity resonance and thus cannot be the cause of our bistability. Therefore, we conclude that among

the different possible absorption mechanisms, surface effects and absorption due to the thin native oxide layer could explain our results (especially if oxide layer is thicker than the expected 4 nm). In addition, direct nonlinear processes due to the $\chi^{(3)}$ of Si (the Kerr effect in particular) could explain our results. However, the Kerr effect results in an instantaneous change of refractive index, whereas thermally-induced refractive index changes occur on a much slower time scale (on the order of µs). Therefore, time domain analysis can help us separate these effects and establish whether or not our nonlinearity is primarily thermal [42, 43, 47]

To do this, we followed the method of [42] and [47], in which the input laser signal is modulated with a sine wave before being coupled into the cavity. In the bistable regime the output signal should be distorted, and tend towards a square wave [18], due to the hysteresis loop (Figure 4.1.2). The minimum detuning at which bistability can be observed can be estimated as $\frac{\sqrt{3}}{2}\delta\lambda$, where $\delta\lambda$ is the linewidth of the cavity resonance. In our experiments, we explored a range of detunings δ, both above and below the theoretical minimum $\delta_{min} = 285$ pm, and gradually increased the modulation speed from 1 kHz to 300 kHz. Since external modulators are not easily available at the mid-IR, we had to modulate the driving current of our QCL using a sine wave from a function generator in order to obtain a modulated laser signal. The signal from the MCT detector was sent into an oscilloscope so that the responses to different input modulation speeds could be monitored. In Figure 4.2.1, we show the results of this experiment at 80 kHz (Figure 4.2.1a) and 200 kHz (Figure 4.2.1b) modulation frequencies. For

51

δ<285pm at 80 kHz, no effect of bistability is seen in Figure 4.2.1a, and a

sinusoidal waveform is recovered at the output. However, at higher detunings, we

can see a clear deviation from the sinusoid, with δ = 300 pm and δ = 380 pm

resulting in a square-looking waveform. At δ = 410 pm, we are at the drop-off

wavelength for this particular input power-level and hence we recover a sharp

discontinuity in the waveform. In contrast, when the input signal is modulated at

200 kHz Figure 4.2.1b, a much less distorted, sinusoidal-like, waveform is

recovered for both δ = 380 pm and δ = 410 pm. This indicates that our bistability

is slow in nature, and is therefore due to thermal effects and not instantaneous

$\chi^{(3)}$ effects. We note that 200 kHz was the modulation frequency at which all

bistability effects disappeared, and therefore we estimate the thermal time

constant to be about 5 μs. This is also consistent with our finite-element

modeling of thermal effects in our cavities.

In order to identify the impact of different surface effects on absorption, we

performed various microelectronic treatments which alter the surface properties

of our cavities. First, an additional hydrofluoric (HF) acid dip was performed to

remove the native oxide formed on our Si cavities due to prolonged exposure to

air (several days). We estimate that 3-4 nm of native oxide can form on our

cavities [45]. Since SiO_2 has a high material absorption in the mid-IR (a = 9.8

cm^{-1} at 4.5 um[46]), even 4 nm can have a detectable absorptive effect, with a

calculated $Q_{absorption}$ of $1.8x10^6$. We carried out a brief dip in 49% HF (10

seconds) and then transferred the sample to a N_2 purged environment to

minimize oxidation and the effects of environmental moisture. The results at low
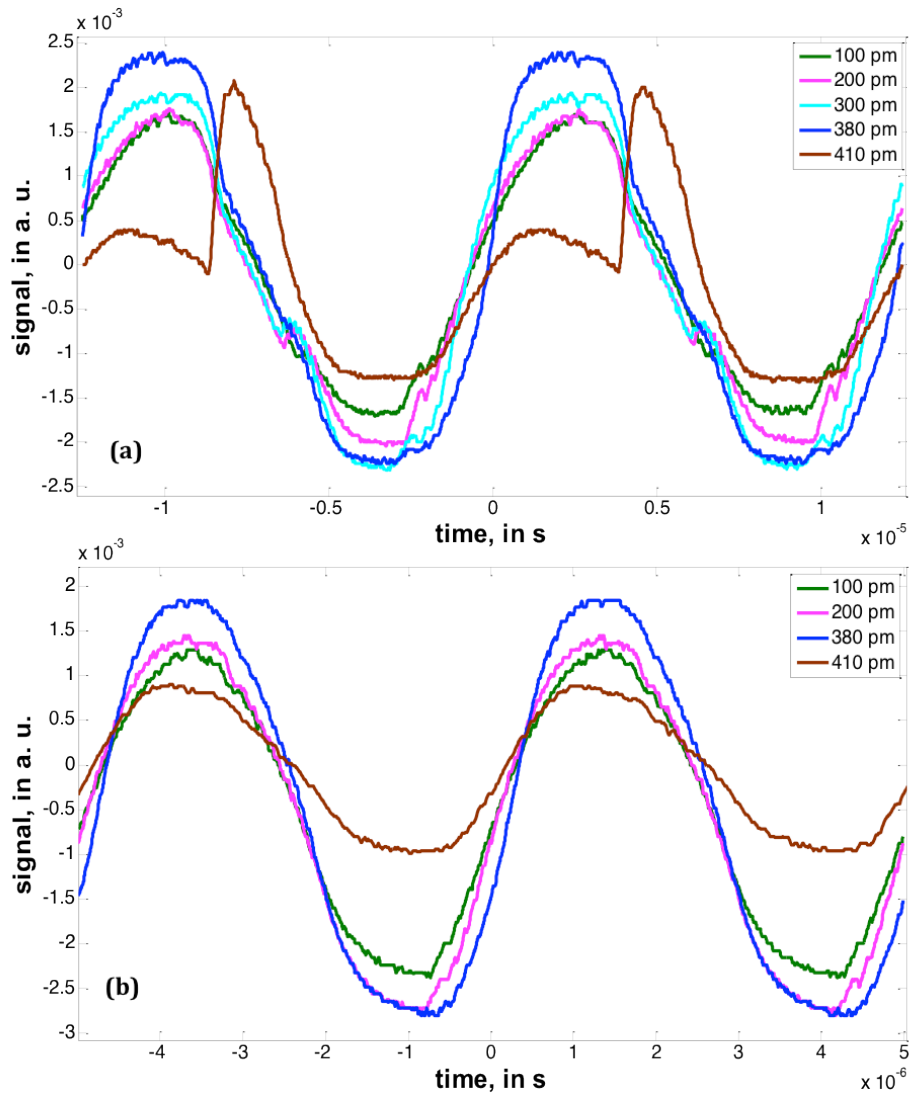
Figure 4.2.1: Temporal response of bistable cavities excited with light modulated at 80kHz and 200kHz. (a) For 80 kHz modulation, clear bistability can be observed for detunings higher than 300 pm: the waveform deviates from the sinusoid, taking on more of a square waveform at detunings of 300 and 380 pm. At $\delta = 410$ pm, we see a sharp discontinuity in the waveform because we are at the drop-off wavelength at this particular power level. (b) For 200 kHz modulation, distortion is reduced and detected waveform tends to sinusoidal.

excitation power are shown in Figure 4.3.1b, with the pre-HF dip cavity spectrum shown in Figure 4.3.1a. As a result of the HF dip, the Q increased from from 11,500 to 21,000 and blueshifted about 500 pm. This is a much larger increase in Q than we expected by only taking into account native-oxide removal, and indicates that the $Q_{absorption}$ of the removed material is about 25,000 (nearly two orders of magnitude smaller than estimated). We speculate that this difference may be due to various surface states formed on native oxide, that when removed result in an increase in Q. However, at higher powers, bistability was still clearly present in the cavity (data not shown). Any potential change in bistability threshold was difficult to quantify, since different amounts of power couple into the cavity during different measurements.

4.3 Effects of micro-electronic treatments on device performance and bistability

In addition to the effects of native oxide, we were concerned about the effects of surface absorption states in the oxide-silicon interface[48, 49] and roughness [48]. To address this, we performed a repeated piranha clean (3:1 H_2SO_4:H_2O_2)/HF dip cycle as proposed by Borselli et al. in [48] to decrease surface roughness and other surface absorption effects. Each cycle consisted of 10 minutes of piranha clean, followed by three rinses in de-ionized (DI) water (30 seconds each), then 1 minute of 10:1 diluted HF acid dip, followed by two DI water rinses (15 seconds each). This cycle was performed three times in total. The purpose of this cyclic process is to oxidize the surface and sidewalls of the

54
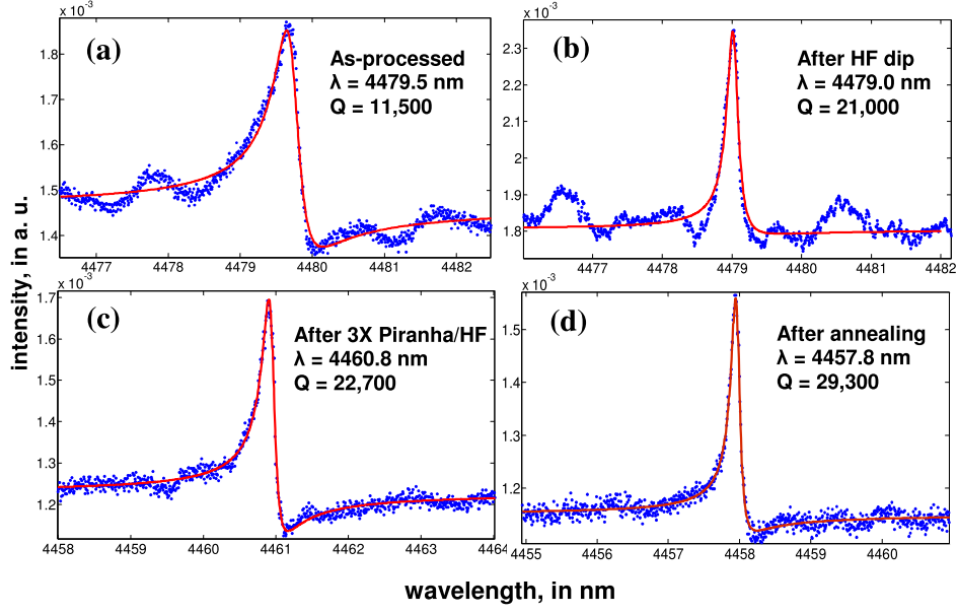
Figure 4.3.1: Effect of different post-fabrication treatments on cavity Q. All spectra are taken at low pump powers, well below bistability threshold. (a) Cavity as-processed. (b) After HF dip. (c) After performing Piranha/HF cycle three times. Note large blue-shift. (d) After annealing.

cavities through the piranha clean and then remove the oxide using HF, resulting in reduced surface roughness and fewer surface absorption states. After this process, the cavities were placed in a N_2 purged environment and characterized. As shown in Figure 4.3.1c, the Q-factor of the cavity went up to 22,700 and the cavity resonance blueshifted by about 18 nm. We estimate $Q_{absorption}$ of the removed material to be 2.8×10^5. Using finite-difference time-domain (FDTD) methods, we calculated that an 18 nm blueshift meant that the Si device layer had decreased in thickness by about 4 nm. Again, even after this processing step, the bistability was still present at high input powers (data not shown).

Finally, we decided to investigate the effects of annealing in order to remove

water moisture from our devices. We annealed our samples in a Lindberg Mini-Mite tube furnace (Thermo Scientific) by ramping up from room temperature to 500°C over a period of 5 hours, holding the temperature at 500°C for 2 hours, and then ramping down to room temperature for one hour. The Q-factor of the cavity went up even further after this treatment, to 29,300, and the resonance wavelength blue-shifted by about 3 nm, as shown in Figure 4.3.1d. $Q_{absorption}$ of the removed material corresponded to about 1×10^5. After this first annealing step, the bistability did not disappear at high input powers (data not shown). However, the increase in Q-factor was significant, indicating to us that water moisture likely has a considerable absorptive effect at 4-5 μm.

A further literature review indicated annealing in a N_2 environment can be used to desorb hydrogen from the surface of Si[50]. Si-H bonds can absorb energy in the 250-300 meV range[50], which corresponds roughly to the resonance wavelength of our cavities. We returned to our cavities after a month's time for another cycle of surface treatments (Figure 4.3.2) in order to address this potential source of absorption. The Q-factor of the cavity decreased to about 22,000 in this period. As before, wavelength spectra were taken before and after each step (not shown). Re-doing the HF dip and Piranha/HF cycling resulted in an increase of Q-factor (to 25,000) and a shift in resonance wavelength from 4458 nm to 4431 nm due to the material removed through this process. Bistability was still present in the cavity after these two steps were completed. However, after repeating the anneal, but this time flowing N_2 through the chamber, we noticed that the cavity spectrum no longer had the characteristic

bistable lineshape (blue curve, taken before annealing) and instead was more Fano-like (red curve) at high input powers. To confirm that the cavity was no longer bistable, we compared input power vs. output power hysteresis loops taken before and after the anneal (insets). The detuning for both hysteresis loops was kept constant, at a value of $\delta = 330$ pm, which is approximately $2\delta_{min}$ for a cavity with Q = 25,000. The pre-anneal hysteresis loop (blue) clearly shows the bistable turn-on and turn-off, whereas the post-anneal hysteresis loop (red) lacks these sharp bistable transitions. Some hysteresis is present in the post-anneal, indicating that some small sources of absorption still remain in the cavity [19], but the bistable turnoff is no longer seen after annealing treatment. The Q-factor did not change measurably after annealing, reaching a value of 25,600. After the sample was placed in air for a few days, the cavity spectrum returned to its pre-annealed state, with bistability appearing at the same input powers as before. However, additional annealing in a N_2 environment caused the bistability to disappear again. Therefore, based on our results we concluded that water moisture and/or Si-H bonds on the surfaces of the silicon device layer is the primary source of absorption that leads to bistability.

Though our main objective in performing these microelectronic treatments on our cavities was to elucidate the source of our bistability, we also discovered a method by which to substantially improve the quality factor of our cavities, from an initial Q of 11,500 to 29,300. We believe that at this point the Q of our cavities is limited by the design; the Q-factor obtained from FDTD calculations was 34,000. In addition, after these treatments, we were able to measure a photonic

57
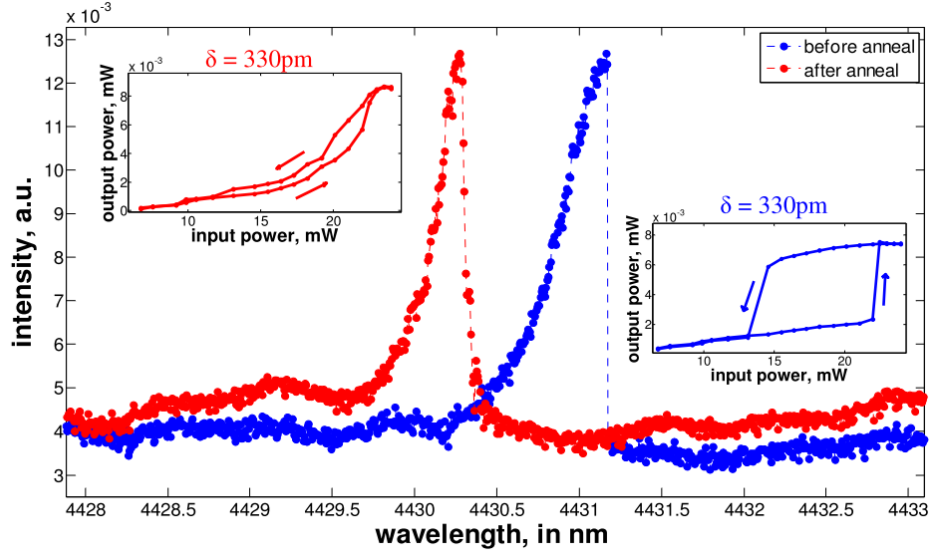
Figure 4.3.2: Cavity spectrum taken before (blue) and after (red) annealing in a N2 environment. The blue spectrum and corresponding hysteresis loop (taken at $\delta = 330$ pm $\approx 2\delta_{min}$) show clear evidence of bistability, while the red spectrum and corresponding hysteresis loop (taken at the same detuning of $\delta = 330$ pm) indicate that bistability is no longer present.

crystal cavity with $s = 0.2a$ with a theoretical $Q = 80{,}000$ that had not been visible pre-treatment, again showing the utility of our treatments in minimizing optical losses. A Q-factor of 45,000 was measured in this case. (We note, however, that this cavity was not used as the basis for the previous discussions due to poorer signal-to-noise ratio as compared to the $Q = 29{,}300$ device, and lack of pre-treatment data.) These micro-electronic treatments and annealing processes can be applied to future mid-infrared Si devices to help improve performance and realize high-Q mid-IR cavities with $Q > 100{,}000$. To achieve this goal, heterostructure cavity designs [51] or nanobeam cavity designs [16] can be used, as they are known to support modes with high quality factors.

4.4 Conclusion

In conclusion, we have observed the presence of bistability in Si mid-IR photonic crystal cavities at 4.5 μm. Through the use of time-domain measurements, we have established that the bistability we see in our mid-infrared photonic crystal cavities is thermal in nature. Finally, we explored the effects of various post-processing methods (HF dips, piranha/HF cycles, and annealing) on the bistability and Q-factors of our cavities. These methods resulted in an increase of Q from 11,500 to 29,300 after processing. In our best devices, Q-factors as high as 45,000 were also measured. Further investigation led to the discovery that annealing in a N_2 environment removed bistability from our cavities even at the highest pump powers possible in our setup, pointing to water moisture or Si-H bonds at the surface as the likely cause of our bistability. Surface effects play a large role in microstructured devices in thin Si device layers, since they have a much higher surface-to-volume ratio as compared to bulk crystalline Si. Because of this, the surface treatments we investigated will likely be necessary to achieve nonlinear optics at the 4-5 μm range [5, 8], allowing us to pump high powers (necessary in order to see nonlinear effects) into Si cavities without deleterious effects. For short-term studies, a single anneal is sufficient, especially if the sample is kept in a dry environment, such as an N_2 chamber or a gel carrier. For longer-term use, surface passivation methods (e.g., capping the devices in alumina or SiN) should be investigated. Decreasing the thermal resistance of the structure will also help mitigate the effects of bistability through the use of

59

different cavity geometries or material platforms, such as

silicon-on-sapphire[22, 23, 52].

5

Grating-coupled Silicon-on-Sapphire

Ring Resonators

The mid-infrared (IR) wavelength region (2-20 μm) is of great interest for a variety of applications as wide-ranging as trace gas sensing, free-space

communications, and thermal imaging. While high-power sources and sensitive detectors at the mid-IR range have finally reached maturity, the passive photonic devices needed to properly access these applications on-chip are still a work in progress. Silicon has previously been proposed as an ideal material for the mid-IR due to its low material losses below 8 μm [2, 4]. Additionally, due to the absence of two- or even three-photon absorption, the mid-IR wavelengths offer us the opportunity to efficiently exploit the optical nonlinearities of Si, opening up a whole host of applications in nonlinear wavelength conversion and signal amplification. However, the traditional silicon-on-insulator (SOI) platform is of limited utility at these wavelengths, since SiO_2 is a highly lossy material in the mid-IR, with losses of over 2 dB/cm at wavelengths longer than 3.5 μm [4, 53]. In Chapter 2, we demonstrated Si membrane photonic crystal cavities (PhCs) operating at 4.5 μm [11, 34], but many mid-IR photonics applications will require an integrated, on-substrate platform. Also, applications in nonlinear optics require higher in-coupled powers than those attainable through the free-space coupling method employed in [11, 34]. Silicon-on-sapphire (SOS) provides an attractive platform for on-substrate mid-infrared photonics, due to the low loss of sapphire through much of the mid-IR [2, 4]. SOS waveguides operating at 2.75 μm [54], 4.5 μm [22], 5.18 μm [52], and 5.5 μm [23], microring resonators operating at 2.75 μm [55] and 5.5 μm [23] , and grating couplers operating at 2.75 μm [54, 55] have already been demonstrated. In this chapter, we demonstrate grating-coupled SOS microring resonators operating in the 4.3-4.6 μm range, with loaded quality (Q) factors of 151,000 and intrinsic Q-factors of

278,000[21].

5.1 GRATING COUPLERS

Coupling high optical powers into MIR resonators has proven to be a challenging task [11, 22, 23]. The fiber-coupling inverse taper method of spot size conversion [56] commonly used at telecommunications (telecom) wavelengths is difficult to achieve with high efficiency, due to the immaturity of fiber technology at the mid-infrared. Grating couplers, on the other hand, can provide highly efficient coupling of light from a free space beam into an optical waveguide. This method has already been well studied at the telecom wavelengths, with experimentally measured coupling losses as low as -1.6 dB [54, 57]. Additionally, grating couplers can be placed anywhere on the chip, affording flexibility in input/output coupling location. For these reasons, we chose to use grating couplers to couple light into our ring resonators.

5.1.1 PRINCIPLES OF GRATING COUPLER OPERATION

In essence, a grating coupler provides phase matching between an input light beam and a particular waveguide mode. Grating couplers consist of a structure with a corrugation with some periodicity Λ (Figure 5.1.1), located next to a slab waveguide with a propagation constant β for the fundamental TE mode of that waveguide. If we choose the the incident angle θ_i and Λ such that

$$k_o n_o sin\theta_i + m\frac{2\pi}{\Lambda} = \beta,$$ (5.1)
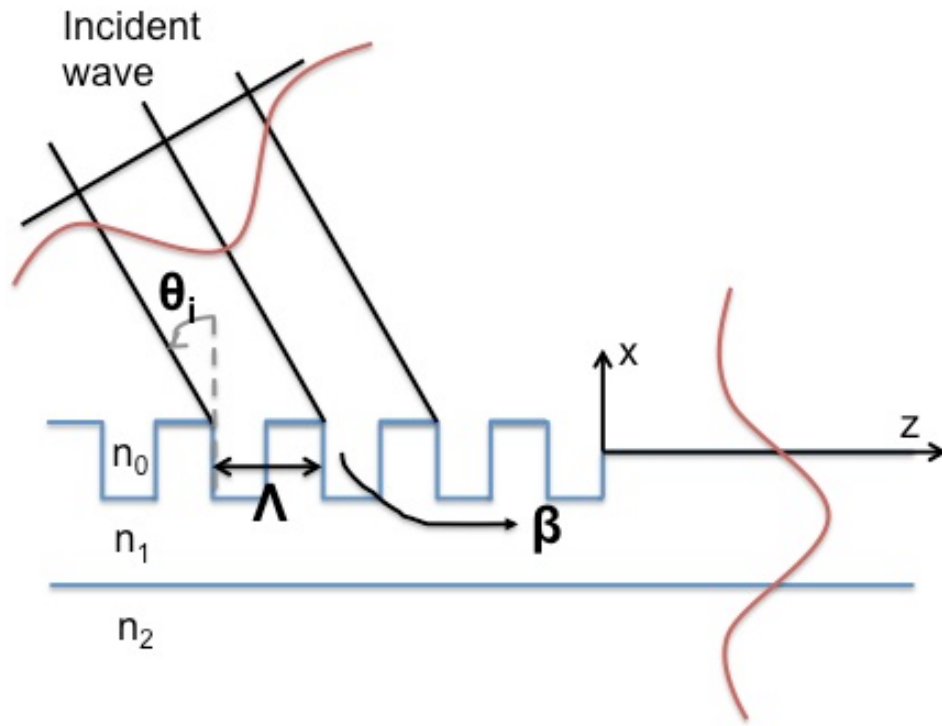
Figure 5.1.1: Principle of grating coupler operation.

for a particular integer m, light from the incident beam will couple to the fundamental TE mode of the waveguide[58]. Grating couplers can also be used for output coupling by the reciprocity principle. This is the general principle of grating couplers, but the specifics of grating efficiency depend on many factors, including the periodicity, number of periods, and cross-sectional shape of the corrugated elements of the grating. As can be seen by looking at Equation 5.1, grating operation is highly angle dependent, so any divergence in the input laser beam has to be taken into account while designing the grating.

64

5.1.2 Grating coupler design

We designed a grating coupler to couple light from our QCL (CW emission from 4.3-4.6 μm) at normal incidence into a waveguide etched into the device layer of our SOS, with thickness $t = 812$ nm. We chose normal incidence for ease of experimental characterization. The grating coupler design was optimized in Comsol using NOMAD[59], a global optimization algorithm. A linear taper function was applied both to the periodicity and the duty cycle of the grating structure, which consisted of fully etched slits in the Si device layer. The theoretical coupling efficiency of the optimized grating at normal incidence for a fully-etched geometry was 40%, with a bandwidth of about 150 nm (Figure 5.1.2). We note that coupling efficiencies in excess of 70% are possible at larger incidence angles. The grating slits are 50 μm wide, so as to accommodate our relatively large beam, about 30 μm in diameter.

5.1.3 Fabrication

The gratings were fabricated on a silicon-on-sapphire substrate with a device layer thickness of 812 nm (IQEP Silicon, Ltd.). ZEP (Zeon Corp.) was used as a mask for electron-beam lithography. A standard 125 kV electron-beam lithography tool (Elionix F-125) was used to define patterns in the ZEP layer, using the procedure described in Section 2.2. A single step etch process was performed in the STS ICP-RIE (Recipe 1 in Section 2.2). The resist was removed using a Piranha etch ($3:1$ $H_2SO_4:H_2O_2$). A scanning electron micrograph of one of our gratings is
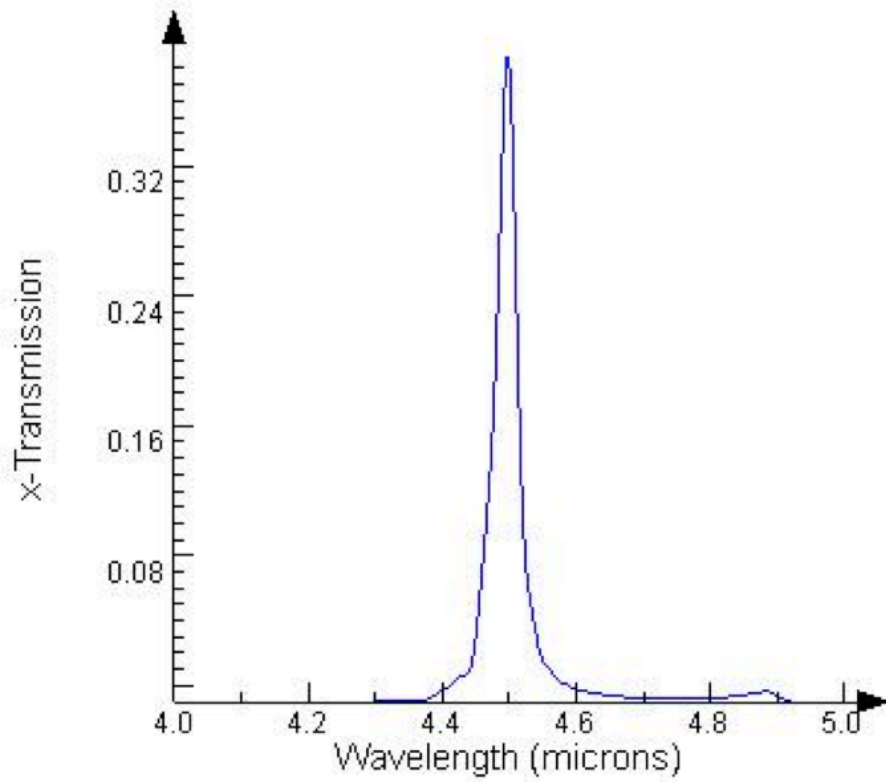
Figure 5.1.2: Result of FDTD simulations of the transmission of our SOS grating coupler. A maximum coupling efficiency of 40% is achieved at 4.5 μm, with a bandwidth of about 150 nm.

Figure 5.1.3: Scanning electron micrography image of a fabricated SOS grating coupler.

shown in Figure 5.1.3. The grating slits need to be oriented in the same direction as the polarization of our input laser, which in our case is horizontally polarized. Due to proximity effects in e-beam lithography, it is hard to exactly match the dimensions of the fabricated coupler to the dimensions in design. For this reason, we fabricated a number of grating couplers with their dimensions scaled by a scaling parameter varying from 0.8 to 1.2.

5.1.4   RESONANT SCATTERING MEASUREMENTS OF GRATING RESPONSE

With the resonant scattering measurement described in Chapter 2, we were able to ensure that the visible light path and the QCL light path were aligned, since both beams were simply reflecting off the sample. However, there is no way to do

the same with a transmission measurement with a grating coupler. The transmission bandwidth of a particular grating coupler is very narrow, and will not accommodate both visible and mid-IR beams no matter the design. Hence, we needed a way to decouple the initial characterization of our grating couplers from the transmission setup (described later in this chapter). To do this, we performed resonant scattering measurements on our grating couplers. A grating coupler can be considered to be a photonic crystal cavity with very low quality factor. Therefore, by using our cross polarization setup (described in Chapter 2), we should be able to recover a peak while scanning the laser over the wavelength range the grating coupler operates within. Alternatively, if the setup is in input polarization configuration (both polarizers aligned), the response should have a dip corresponding to where the light couples to the grating coupler. The samples were oriented at $45°$ with respect to the laser polarization to maximize the signal-to-noise ratio.

Results from this characterization for a particular grating coupler are shown in Figure 5.1.4, with the background removed. Because the etched regions tended to scramble polarization irrespective of whether the grating bandwidth was in the tuning range of the laser or not, there was a high background signal for the cross polarized signal. Nevertheless, we were able to see clear peaks in cross polarization (CP) and dips in input polarization (IP) for the particular gratings that coupled light within our laser's tuning range. As the slit widths increased, the peaks shifted further to the right, as expected (not shown). Using this method, we were able to characterize the response of our grating couplers and knew, going
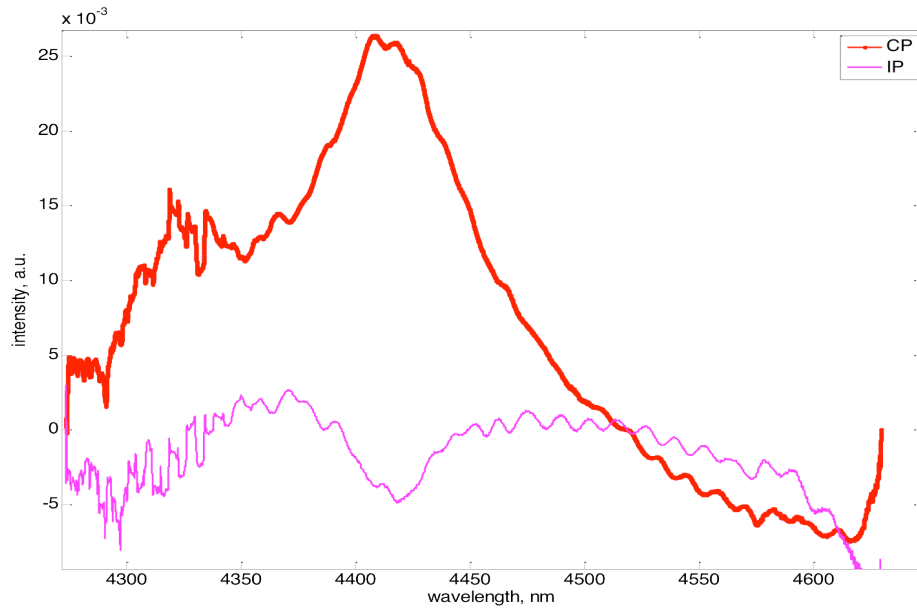
Figure 5.1.4: Resonant scattering response of a grating coupler. A peak is seen in cross-polarization, and a dip seen in input polarization, if the grating coupler couples light within our laser tuning range.

forward, which dimensions to use in fabrication to make grating-coupled devices. However, this method does not provide us with much information regarding coupling efficiency.

5.2 GRATING-COUPLED DEVICES

Having determined that we had operational grating couplers, we then turned to fabricating grating-coupled resonators. We chose to focus on ring resonators, since they can support numerous high-Q factor modes, a useful trait for nonlinear wavelength conversion applications. For the 4.3-4.6 μm wavelength

range, a waveguide with width 1.5 μm and height 0.812 μm is single mode. These dimensions are used for both the coupling waveguide and ring resonator. However, our grating slits are 50 μm wide, meaning we need to taper down from a 50 μm width for the grating down to a 1.5 μm width for the single mode waveguide. The length of this taper is very crucial in order to achieve adiabatic transition from wide waveguide to the narrow one. Otherwise, short tapers can result in a high percentage of reflected signal due to impedance mismatch. Results of FDTD simulations of transmission through the taper are shown in Figure 5.2.1. A taper of 150 μm, for example, reflects almost 45% of the light. We chose a taper length of 500 μm to ensure that more than 90% of our light is transmitted to the single mode waveguide.

On the output end, we chose to collect light from an end-cleaved facet, rather than use a grating out-coupler. This simplified the experimental setup considerably. Because of the N.A. of the output coupling lens (0.5), an inverse taper needed to be applied to the end facet so that more of the light from the facet would fall within the acceptance angle of the lens. To accommodate this, a horn-shaped coupler consisting of a 750 μm long linear taper with a width of 50 μm at the output end was used to improve collection of light at the output. By using this approach [22, 23], we were able to increase our theoretical out-coupling efficiency from 9% (for a 1.6 μm waveguide without a horn) to 25%, assuming a lens with numerical aperture of 0.5.

The grating coupled devices were fabricated using the same method described in Section 2.2, with one additional step: the sample was manually cleaved on the
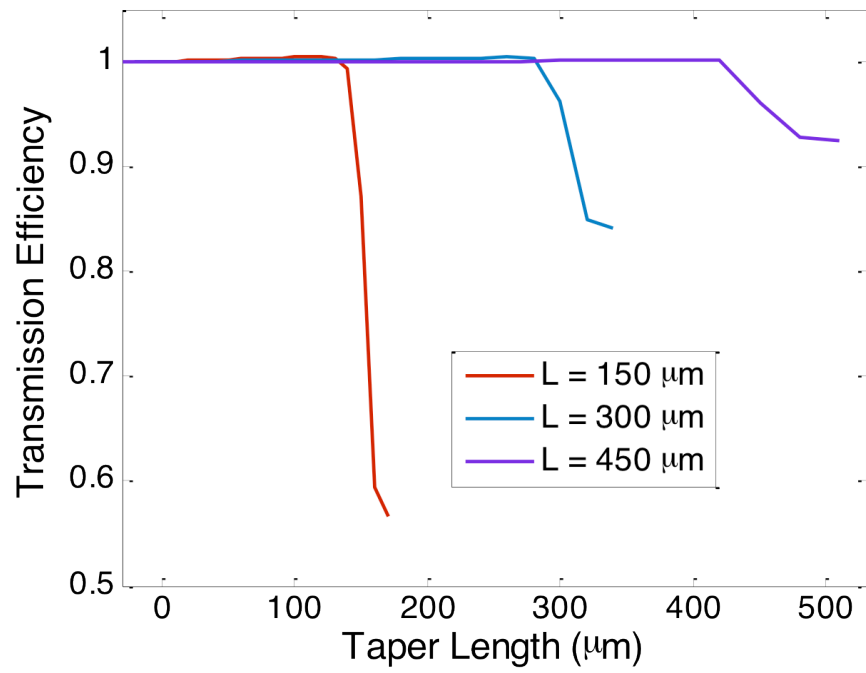
Figure 5.2.1: Results from FDTD simulations of transmission efficiency through tapers (from grating to single mode waveguide) of varying lengths. Shorter taper lengths result in significant reflection loss.

output waveguide (in the 50 μm wide portion), providing the end-facet for out-coupling. Photoresist (Shipley 1813) was spun on the the device side of the sample so as to protect the devices, and then stripped off in Remover PG (MicroChem) and isopropanol alcohol after cleaving. This cleaving step was performed before resist removal in the piranha clean.

An optical micrograph of one of our devices is shown in Figure 5.2.2. The grating coupler, taper region, ridge waveguide, and ring resonator all are fully etched into the Si device layer with thickness $t = 812$ nm. The coupling waveguide and ring resonator both have a width $w = 1.5$ μm, and the ring radius $r = 60$ μm. The grating slits are 50 μm wide, and the taper region between the grating and coupling waveguide is 500 μm long. Rings with gaps d between the coupling waveguide and ring resonator varying between 300 and 700 nm were fabricated. Since the bandwidth of the grating is smaller than the mode-hop free tuning range of our laser, the grating geometry was varied from device to device in order to cover the laser's tuning range. This was done by multiplying each grating dimension with a constant in the range of 0.98 to 1.06, which shifts the center wavelength of the grating by the same factor.

5.2.1 Characterization setup

To characterize these devices, we built an additional arm on the setup for transmission measurements. This way, the original resonant scattering setup could still be used to locate the grating couplers using SRSM. A schematic of the transmission arm used to characterize our devices is shown in Figure 5.2.3. Light
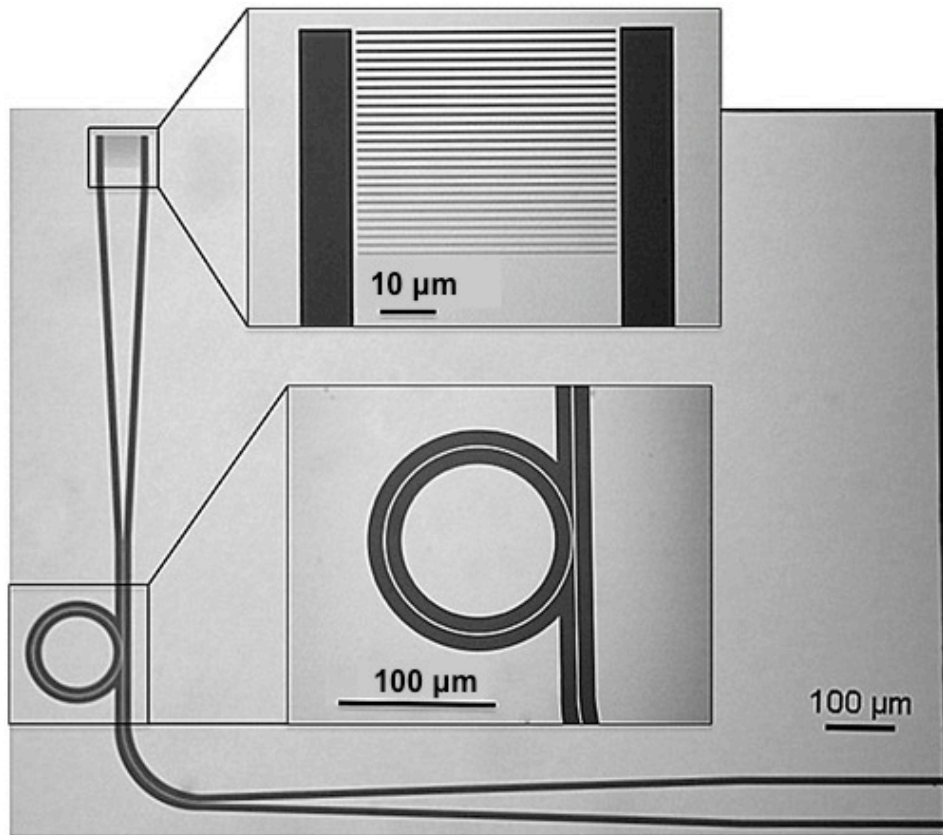
Figure 5.2.2: Optical image of a representative device, consisting of a ring resonator (bottom inset) coupled to a waveguide with a grating coupler (top inset) on input end and horn-coupler on the output end.
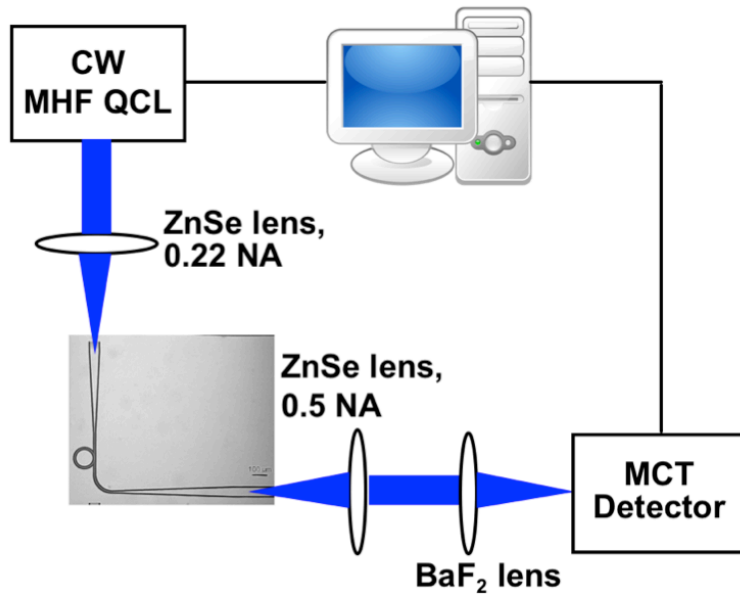
Figure 5.2.3: Schematic of mid-IR setup used to measure our devices in transmission.

from a tunable continous-wave quantum cascade laser (QCL) from Daylight Solutions, Inc., with emission from 4.27 to 4.63 μm and linewidth of <45 MHz, is sent through a ZnSe objective (numerical aperture of 0.22) and focused onto the input grating. A second ZnSe lens (numerical aperture of 0.5) is placed at right angle to the first lens in order to collect light from the end facet. Finally, the light is focused onto a thermoelectrically cooled HgCdTe detector.

5.2.2   FULLY ETCHED RESULTS

Transmission data from our as-processed ring resonators is shown in Figures 5.2.4 and 5.2.5. Results from device with value of d = 300 nm (Figure 5.2.4), 400 nm (Figure 5.2.5, top), and 550 nm (Figure 5.2.5, bottom) are shown. No resonances

were seen for devices with $d = 700$ nm. The free spectral range (FSR) of our resonators was measured to be 12.4 nm around 4.4 µm, which closely matches the expected FSR of a ring with radius $r = 60$ µm and theoretical group waveguide index of 4.1 at 4.4 µm. For a ring resonator coupled to a waveguide, the total (loaded) Q-factor Q_t is given by the relation $Q_t^{-1} = Q_o^{-1} + Q_c^{-1}$, where Q_o is the intrinsic Q-factor (determined by radiation losses and material absorption, including surface states) of the ring resonator, and Q_c is the coupling Q-factor (determined by the coupling strength with the waveguide). Power transfer between the waveguide and the ring resonator is maximized when $Q_o = Q_c$, a regime known as critical coupling. For $Q_o < Q_c$, the ring resonator is considered undercoupled, and for $Q_o > Q_c$, the ring resonator is considered overcoupled. In our measurements, the coupling decreased with increasing d, indicating that our devices operate in the undercoupling regime. The experimentally obtained transmission spectra were fitted to theoretical curves obtained by solving a set of coupled mode equations [60] that take into account the scattering-induced coupling of clock-wise and counter-clock-wise propagating modes, which can be observed as mode-splitting for very high-Q resonators.

We can obtain the expression for the ring resonator transmission in the case of mode-splitting by using a coupled oscillator model:

$$\frac{da_{cw}}{dt} = -(\frac{1}{\tau_t} + i\Delta\omega)a_{cw} + i\beta a_{ccw} + k|s|, \qquad (5.2)$$
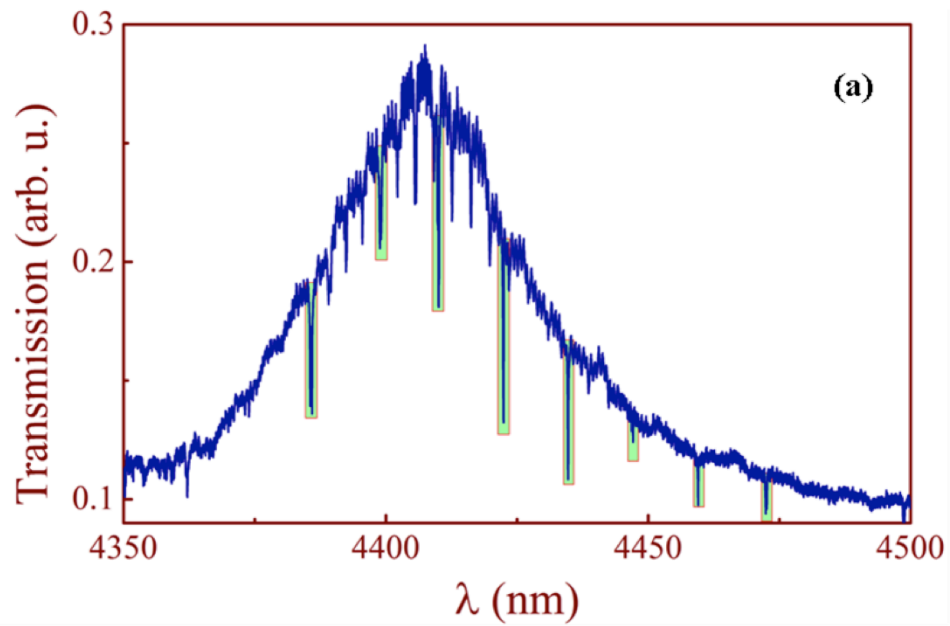
Figure 5.2.4: Transmission measurement of device with coupling gap d = 300 nm, as fabricated. Ring resonances are highlighted with green to distinguish them from gas absorption dips (from atmospheric $C_{13}O_2$).
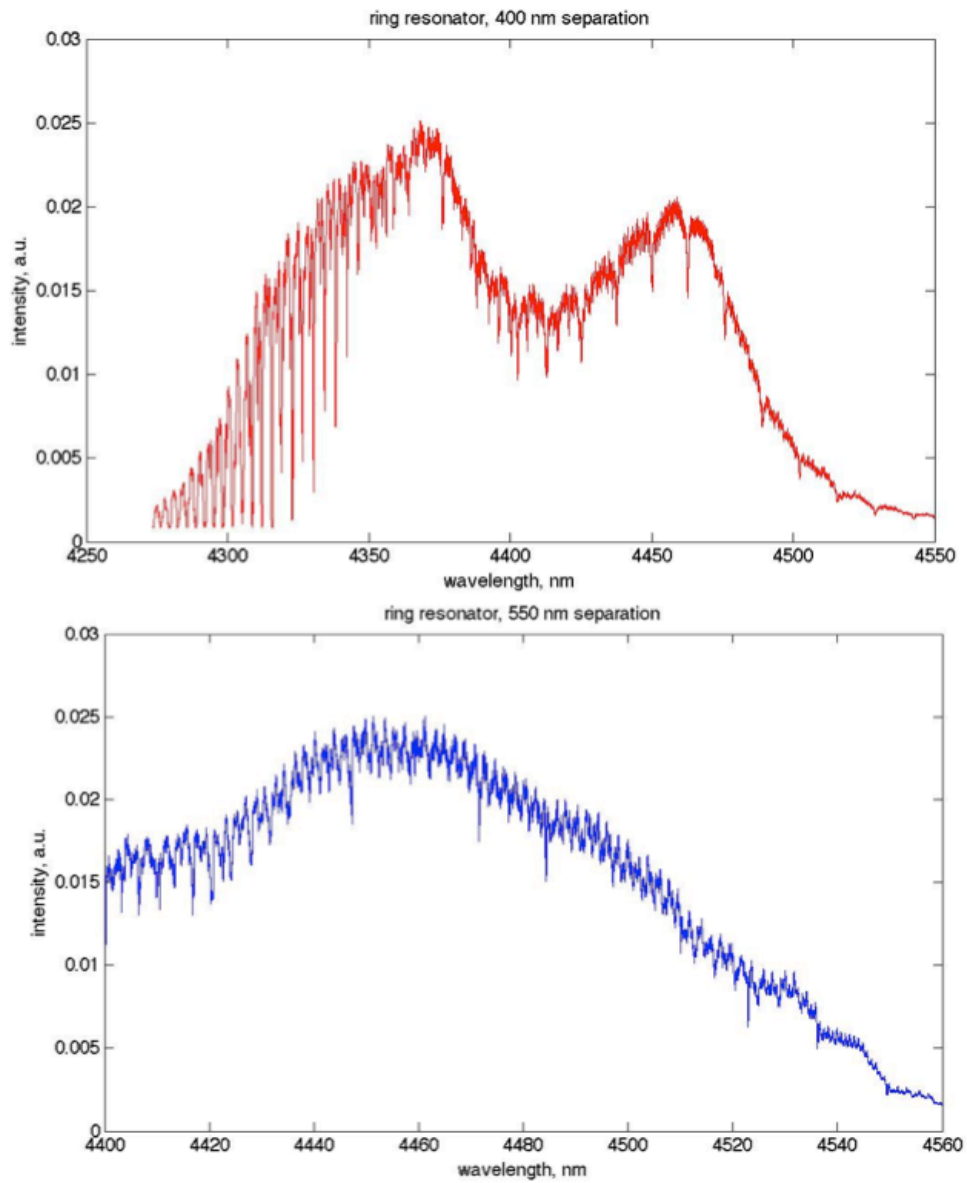
Figure 5.2.5: Transmission measurements of devices with coupling gap d = 400 nm (top panel) and 550 nm (bottom panel), as fabricated. No resonances were seen for d = 700 nm.

$$\frac{da_{ccw}}{dt} = -\left(\frac{1}{\tau_t} + i\Delta\omega\right)a_{ccw} + i\beta a_{cw}, \tag{5.3}$$

where a is the amplitude of the clockwise (CW) and counterclockwise (CCW) modes of the resonator, the mode decay rate is $2/\tau_t$, $\Delta\omega$ is the detuning of the laser from the cavity resonance, β is the coupling strength of the modes, $\kappa = \sqrt{\frac{2}{\tau_c}}$ is the coupling rate between the coupling waveguide and the ring resonator where τ_c is the coupling lifetime, and s is the input field ($|s|^2$ is the input pump power). At steady state, $\frac{da_{cw}}{dt} = \frac{da_{ccw}}{dt} = 0$. Then we can solve Equation 5.3 for a_{ccw} and substitute into Equation 5.2 , obtaining the following expression for a_{cw}:

$$a_{cw} = \frac{\kappa|s|}{\left[\left(\frac{1}{\tau_t} + i\Delta\omega\right) + \frac{\beta^2}{\frac{1}{\tau_t}+i\Delta\omega}\right]} \tag{5.4}$$

The coupling of the CW and CCW modes to the waveguide results in a transmitted field (with transmission coefficient t) and reflected field (with reflection coefficient r):

$$t = -|s| + \kappa a_{cw}; r = \kappa a_{ccw}, \tag{5.5}$$

The transmission coefficient t then becomes:

$$t = -|s|\left(1 - \frac{\kappa^2}{\left[\left(\frac{1}{\tau_t} + i\Delta\omega\right) + \frac{\beta^2}{\frac{1}{\tau_t}+i\Delta\omega}\right]}\right) \tag{5.6}$$

Then rewriting t in terms of $Q_t = \omega_o\tau_t/2$, and $Q_c = \omega_o\tau_c/2$, we obtain:

$$t = -|s|(1 - \frac{\omega_o/Q_c}{(\frac{\omega_o}{2Q_t} + i\Delta\omega) + \frac{\beta^2}{\frac{\omega_o}{2Q_t}+i\Delta\omega}}). \tag{5.7}$$

The normalized transmission T through the ring resonator is then given by $T = |t|^2/|s|^2$.

Using this model, we inferred maximum loaded Q values of Q_t = 41,000, and intrinsic Q-factors of Q_o = 45,000. In order to improve the performance of our devices, we decided to subject them to the post-fabrication microelectronic treatments described in [34, 48], namely Piranha etch/HF cycling and annealing. The former treatment decreases absorption due to surface states and reduces surface roughness, while the latter treatment reduces absorption due to water [34]. A cycle of Piranha etch ($3:1$ $H_2SO_4:H_2O_2$) and HF acid performed three times in succession (process detailed in [48]) had the most dramatic effect, increasing loaded Qs to as much as 94,000 and drastically improving the coupling across all devices. Annealing had limited effect on these devices. At high input powers, bistability was also seen in the highest-Q devices (not shown). The response from one of the best devices (with d = 300 nm) is seen in Figure 5.2.6. After post-processing, we were also able to see resonances for devices with d = 700 nm, indicating that Q_o for these devices had increased with respect to Q_c (Figure 5.2.7). From fitting the transmission spectrum, we deduced intrinsic Q-factors as high as Q_o = 127,000 (see inset, Figure 5.2.6).
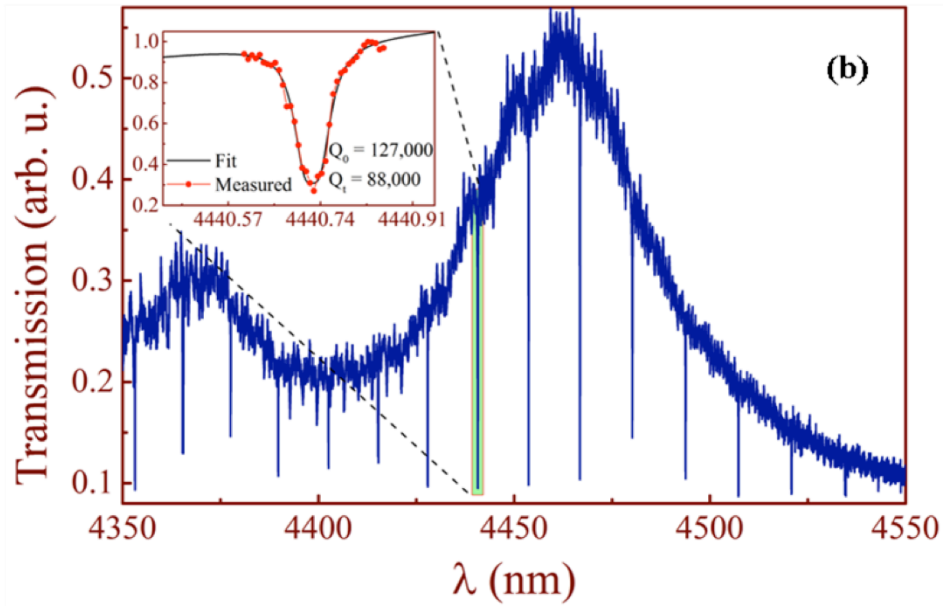
Figure 5.2.6: Device with d = 300 nm, after Piranha etch/HF cycling. Power transfer between the waveguide and the ring is greatly improved, and maximum loaded Q-factors have increased from 45,000 to 94,000, with a maximum intrinsic Q-factor of 127,000, shown in the inset.
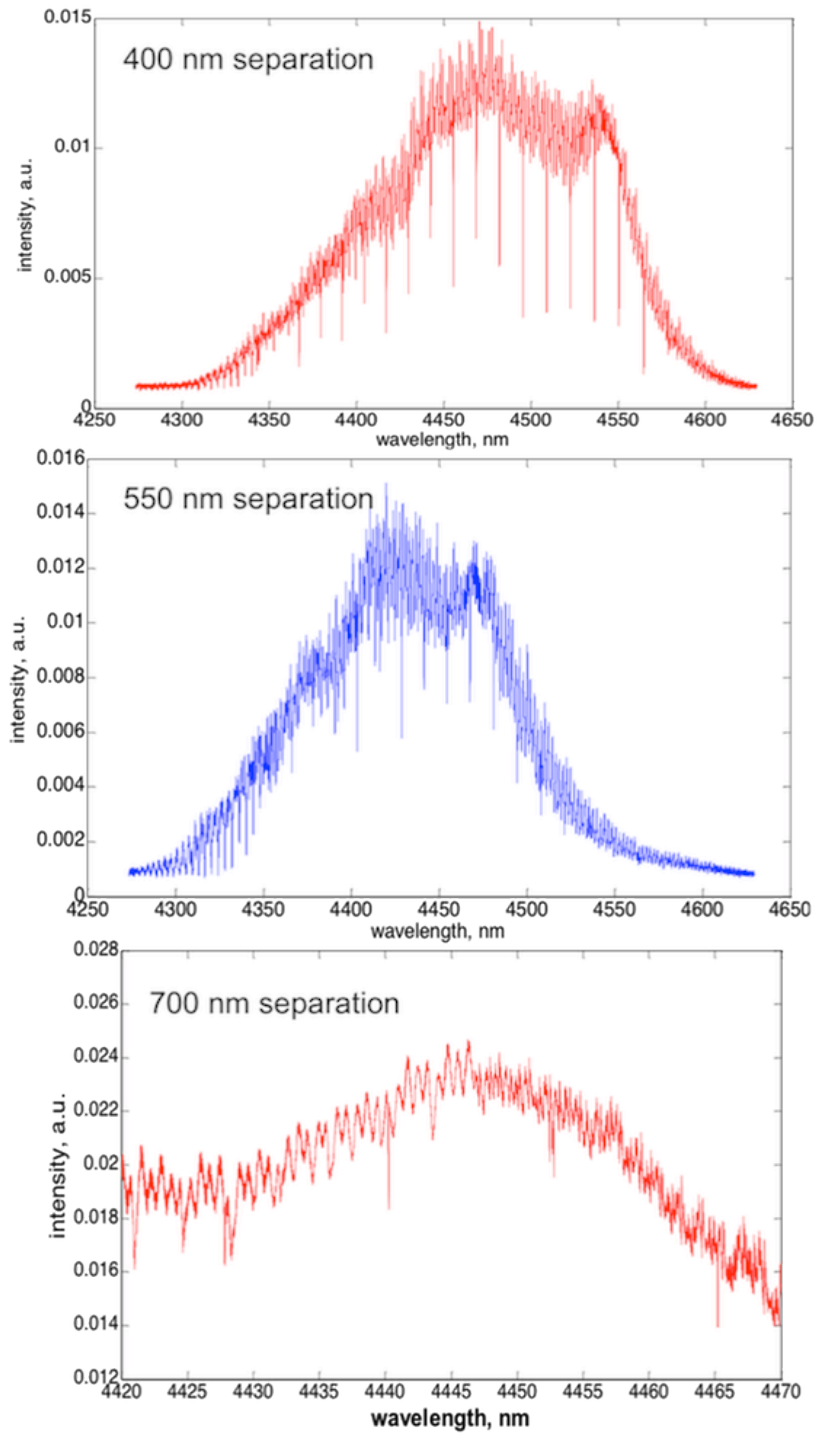
Figure 5.2.7: Transmission measurements of devices with d = 400 nm (top), 550 nm (center), and 700 nm (bottom), after Piranha etch/HF cycling.

81

To minimize scattering losses due to fabrication imperfections, we applied the resist reflow method to our devices[61]. In our case, resist reflow consisted of a 5-minute post-lithography bake in an oven at 140° C. Because of the fine features within our grating couplers, we had to use lower bake temperatures for ZEP reflow than those typically used for microresonators [61], which is usually done at around 160° C. After the reflow, the sample underwent etching, cleaving, and Piranha etch-HF acid cycling as described above. The results are shown in Figure 5.2.8. Q-factors increased noticeably after the reflow, with total Q-factors as high as $Q_t = 151,000$, corresponding to a resonance linewidth of 440MHz, and intrinsic Q-factors as high as $Q_o = 278,000$. These Q-values are the highest measured in the 4-5 μm wavelength range in Si. We note that for all device geometries we tested (a total of 12) Q-factors obtained with resist reflow were higher than Qs of the devices where the reflow was not used.

Using our Q values, we can estimate the loss of our ring resonators to be about 0.74 dB/cm at 4.5 μm. We note that this loss value takes into account light scattering (due to surface roughness) and material absorption (due mostly to surface states), and also bending losses of the ring resonator (which are negligible in large diameter devices that we studied). This is slightly higher than the lowest waveguide loss values measured in silicon devices at the mid-IR (0.6 dB/cm at 3.39 μm in the case of SOI waveguides) [62]. Our comparatively higher losses may be due to scattering losses from twinning defects inherent in SOS[63].
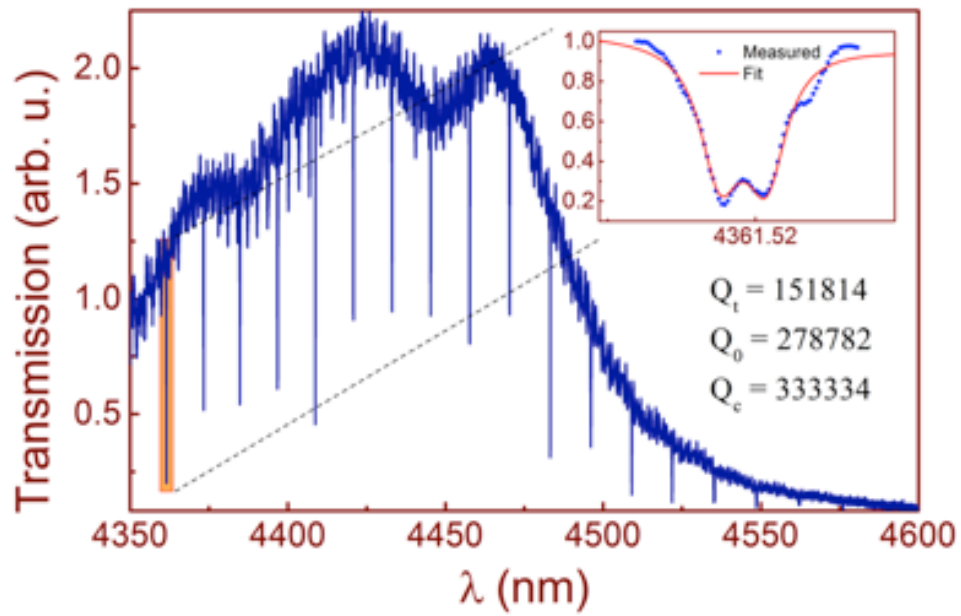
Figure 5.2.8: Transmission measurement of device with d = 300 nm, fabricated using resist reflow and post-fabrication Piranha-HF cycling. The reflow results in higher Q-factors, with a maximum loaded Q_t of 151,000 and intrinsic Q_o of 278,000, as shown in the inset.

5.2.3   PARTIALLY ETCHED DEVICES

Another variant on grating-coupled SOS ring resonators may be made by partially etching rather than fully etching the Si. This results in a devices that have a Si "pedestal" in cross section. Because of this, the mode should be more confined to the Si, though the waveguide width needs to be increased to accommodate the pedestal. The higher confinement in Si should lead to lower loss since less of the mode interacts with the comparatively lossier sapphire substrate.

We made grating-coupled SOS ring resonators with a 510 nm partial etch, and a waveguide width of 2.8 μm, and coupling gaps d of 600 nm, 800 nm, and 1000 nm. Other than the grating parameters (period and slit widths), which needed to be changed to accommodate the partial etch, all other parameters were kept the same as in the fully etched case. All part of the device (grating, taper, waveguide, ring) were etched to the same depth. Results from one of our partially etched devices, with no post-fabrication treatments performed, are shown in Figure 5.2.9 . No resist reflow was performed during the fabrication. Remarkably, the as-processed Q-factors on this sample were similar to devices made with resist reflow and Piranha-HF cycling. This is likely due to the fact that more of the mode is confined to the Si. Afterwards, Piranha-HF cycling was performed, but it had very little impact on either the Q-factors or power transfer between the coupling waveguide and resonator. Performing even shallower partial etches may have an even greater impact on Q.
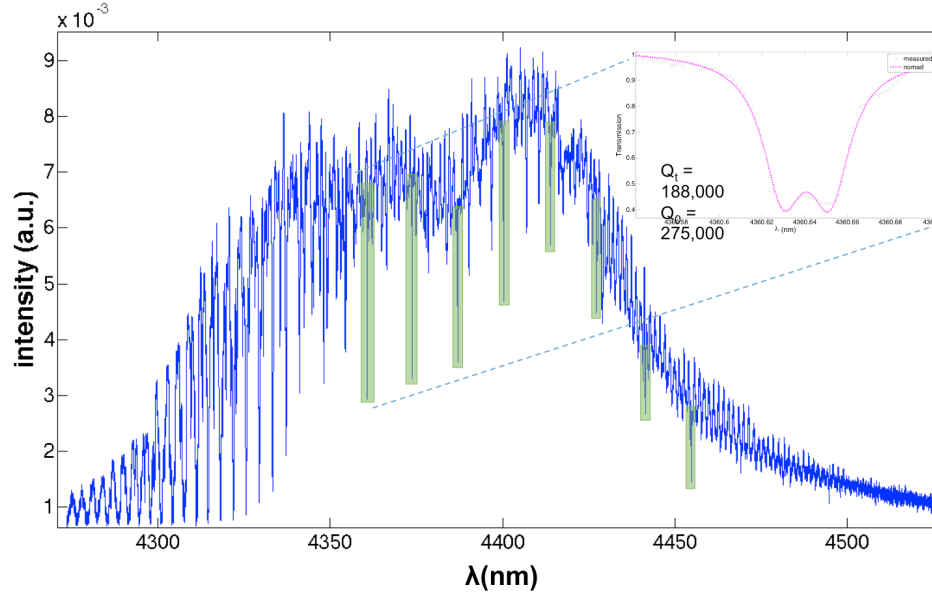
Figure 5.2.9: Transmission measurement of partially etched ring resonator (etch depth = 510 nm) device with d = 600 nm, with a maximum loaded Q_l of 188,000 and intrinsic Q_o of 275,000, as shown in the inset. No post-fabrication treatments were done on this sample.

5.3 CONCLUSION

In conclusion, we have realized mid-IR integrated on-chip optical networks operating at the 4.5 μm wavelength range, based on the SOS material platform. Grating-coupled ring resonators, with intrinsic Q-factors as high as 278,000, were demonstrated. High Q-factor resonators in the mid-IR are of great interest for trace-gas sensing in particular, and the realization of portable spectroscopy systems in general. Another exciting application of our platform is on-chip nonlinear wavelength conversion via four-wave mixing, as well as the potential realization of chip-scale frequency combs operating in the mid-IR.

6

Nonlinear Wavelength Generation in Silicon-based Mid-IR Devices

In this chapter, we explore the $\chi^{(3)}$ nonlinearities of Si, with a special emphasis on stimulated four-wave mixing (FWM) and optical parametric oscillation. We

discuss the suitability of the SOS devices described in Chapter 5 to nonlinear applications such as FWM and frequency comb generation in the mid-IR.

6.1 Optical nonlinearities in Si

One interesting feature of Si is its high optical nonlinearity, compared to many glasses and CMOS-compatible materials (Table 1). Because of Si's inversion symmetry, $\chi^{(2)}$ effects are suppressed, but the $\chi^{(3)}$ of Si is about one hundred times that of silica glass, and ten times larger than that of Si_3N_4. Additionally, Si has a high refractive index (3.42 at 4.5 μm), meaning that light can be more strongly confined within the material, thus enhancing the effective nonlinearity. However, the presence of two-photon absorption (TPA) at wavelengths below 2.2 μm means that Si becomes extremely lossy at the high intensities of light typically needed to achieve nonlinearities in the telecom regime. These absorbed photons lead to the creation of free carriers within Si, which also absorb light through free-carrier absorption. Because Si has a low free carrier recombination rate (due to its indirect bandgap), the free-carrier population and subsequent optical loss become quite considerable at high input intensities [5], In contrast, TPA (and depending on the wavelength chosen, even three-photon and four-photon absorption) is not an issue at the mid-IR, since two mid-IR photons cannot overcome the 1.1 eV bandgap of Si. It was shown in [64] that the transmission ratio for high power densities of 2.936 μm light (above the two-photon absorption cutoff of 2.2 μm) pumped into a Si waveguide does not vary significantly with power density, whereas at 2.09 μm, the light pumped into

87

Table 6.1.1: Kerr coefficients of various materials

Material	n_2 $[m^2/W]$
Si	3.6×10^{-18}
SiO_2	2.7×10^{-20}
CaF_2	1.26×10^{-20}
Diamond	1.3×10^{-19}
Si_3N_4	2.5×10^{-20}

the Si waveguide declines as the power density is increased, due to TPA. Hence, the mid-IR gives an opportunity to efficiently exploit the $\chi^{(3)}$ nonlinearities of Si.

Optical nonlinearities originate from the interaction of the optical field with bound electrons and phonons. The electrical field component of the optical field resonates with the outer electrons of Si atoms, causing polarization. We can write this induced polarization $P(t)$ in terms of the electric field $E(t)$ as follows (assuming an instantaneous dielectric response):

$$P(t) = \varepsilon_0 (\chi^{(1)} E(t) + \chi^{(2)} E^2(t) + \chi^{(3)} E^3(t) + ...), \qquad (6.1)$$

where ε_0 is the vacuum permittivity and $\chi^{(i)}$ are the i-th order optical susceptibilities [65]. The susceptibilities are tensors of rank $(i+1)$ from which all linear and nonlinear optical effects deriving from the polarizability of a material can be derived. Since our interest is in nonlinear effects, we focus on $\chi^{(3)}$ processes, as $\chi^{(2)}$ processes are non-existent in Si due to its inversion symmetry. If

we have a electric field $\mathbf{E}$ with three frequency components (ω_k):

$$\mathbf{E}(\mathbf{r}, t) = \sum_{k=1}^{3} \mathbf{E}_k = \frac{1}{2} \sum_{k=1}^{3} (\mathbf{E}_{\omega_k,k}(\mathbf{r}, \omega_k)e^{i\omega_k t} + c.c.), \qquad (6.2)$$

where $c.c$ is the complex conjugate. By substituting equation 6.2 into equation 6.1 and expanding $\chi^{(3)}$ in terms of its frequency components, we obtain several terms at different frequencies for the third-order polarization $P^{(3)}$:

$$
\begin{aligned}
P^{(3)} = \\
& \frac{3}{4}\varepsilon_0\chi^{(3)}\left[|E_{\omega_1}|^2 E_{\omega_1} + \therefore\right] \\
& +\frac{6}{4}\varepsilon_0\chi^{(3)}\left[(|E_{\omega_2}|^2 + |E_{\omega_3}|^2)E_{\omega_1} + \therefore\right] \\
& +\frac{1}{4}\varepsilon_0\chi^{(3)}\left[(E^3_{\omega_1}e^{i3\omega_1 t} + c.c) + \therefore\right] \\
& +\frac{3}{4}\varepsilon_0\chi^{(3)}\left[\frac{1}{2}(E^2_{\omega_1}E_{\omega_2}e^{i(2\omega_1+\omega_2)t} + c.c) + \therefore\right] \\
& +\frac{3}{4}\varepsilon_0\chi^{(3)}\left[\frac{1}{2}(E^2_{\omega_1}E^*_{\omega_2}e^{i(2\omega_1-\omega_2)t} + c.c) + \therefore\right] \\
& +\frac{6}{4}\varepsilon_0\chi^{(3)}\left[\frac{1}{2}(E_{\omega_1}E_{\omega_2}E^*_{\omega_3}e^{i(2\omega_1+\omega_2-\omega_3)t} + c.c) + \therefore\right] \\
& +\frac{6}{4}\varepsilon_0\chi^{(3)}\left[\frac{1}{2}(E_{\omega_1}E_{\omega_2}E_{\omega_3}e^{i(2\omega_1+\omega_2+\omega_3)t} + c.c) + \therefore\right],
\end{aligned}
$$

$$(6.3)$$

where $\therefore$ stands for all possible permutations of frequencies. The terms in equation 6.3 represent different nonlinear processes (described in more detail below) that can result from the third-order susceptibility. Efficient excitation of these processes is only achieved under both energy and momentum conservation (phase-matching). By choosing the appropriate frequencies (i.e., energy levels)

and performing phase-matching, we can choose a particular process from among multiple possible nonlinear processes.

The first term in equation 6.3, $\left[\frac{3}{4}\varepsilon_\circ\chi^{(3)}\left[|E_{\omega_1}|^2E_{\omega_1}+\therefore\right]\right]$, is the process known as self-phase modulation, in which excitations are induced by three photons (all at a single frequency ω_1). This process leads to the intensity-dependent refractive index component (the Kerr coefficient) n_2, which then modifies the frequency characteristics of the pulse that generated the refractive index change, leading to pulse broadening. At very high power levels, SPM may be used for super continuum generation. Additionally, the same photons that cause SPM can also cause two-photon absorption (TPA), as described above. Because of this, TPA leads to an intensity-dependent component, a_2, of the imaginary part of the refractive index, i.e. the absorption coefficient, $a_\circ$. SPM and TPA affect the complex refractive index n such that:

$$n = n_\circ + n_2 I - i\frac{\lambda}{4\pi}(a_\circ + a_2 I), \qquad (6.4)$$

where I is the intensity and n_2 and a_2 can be related to $\chi^{(3)}$ by the following equations:

$$n_2 = \frac{1}{cn_\circ^2\varepsilon_\circ}\frac{3}{4}Re\left(\chi^{(3)}\right) \qquad (6.5)$$

$$a_2 = \frac{-\omega}{c^2n_\circ^2\varepsilon_\circ}\frac{3}{2}Im\left(\chi^{(3)}\right) \qquad (6.6)$$

A useful nonlinear figure of merit is given by $F_n = n_2/(\lambda a_2)$, where λ is the
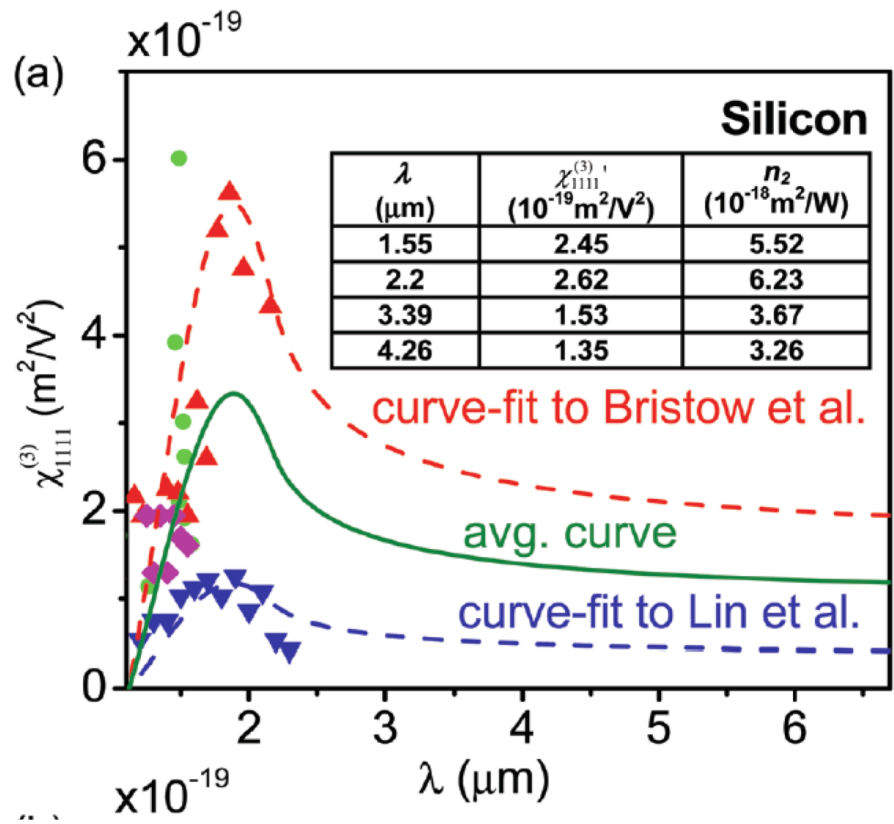
Figure 6.1.1: $\chi^{(3)}$ and n_2 of Si as a function of wavelength λ. $\chi^{(3)}$ has not yet been measured experimentally through most of the mid-IR, so three curve-fits to existing measurements are shown. Taken from [9], permission to use granted by Professor Bahram Jalali.

91

optical wavelength in vacuum [65, 66]. Since TPA goes to zero for wavelengths above 2.2 μm, this nonlinear figure of merit is quite high in the mid-IR, despite slightly lower (expected) n_2 in this wavelength regime. Figure 6.1.1 shows $\chi^{(3)}_{1111}$ as a function of λ over the infrared regime. Measurements are indicated by the solid triangles and diamonds. The dotted line shows the expected $\chi^{(3)}_{1111}$ extrapolated from curve fitting, since experimental measurements of n_2 have not yet been done beyond 2.3 μm.

The second term in equation 6.3 is the cross-phase modulation (XPM) term. In XPM, a signal at ω_1 affects another signal at ω_2. From equation 6.3, we can see that the change in refractive index induced by XPM is twice as strong as that induced by SPM. The third term in equation 6.3 corresponds to third-harmonic generation (THG), in which pumping at a single frequency ω_1 generates a new signal oscillating at $\omega_{THG} = 3\omega_1$. The remaining 4 terms in equation 6.3 describe different four-wave mixing (FWM) processes, in which three incident photons generate a fourth photon at the idler frequency ω_i. FWM will be described in more detail in the next section. Since FWM, like all Kerr nonlinear processes, is ultrafast, there is a strong interest in using FWM for a number of applications including wavelength conversion and parametric amplification.

In the above treatment, we focused on the contribution of the oscillations of bound electrons to the $\chi^{(3)}$ of silicon. However, another contribution comes from Raman scattering induced by optical phonons. The Raman scattering contribution is outside the scope of this work, but we note that Si also has a relatively high Raman gain, and exploiting this Raman gain at the mid-IR is also a

very fruitful subject of study [7, 64].

In order to effectively exploit silicon's $\chi^{(3)}$ nonlinearities, the light must be introduced into a waveguide or resonator in which the light can be strongly confined. To design effective structures for nonlinear wavelength generation, the structure must (1) have a high optical field confinement; (2) the n_2 of the structure's material must be high; (3) the FOM must be high (meaning that TPA will not be problematic) and (4) if necessary, phase matching should be maintained via dispersion engineering. We can define a nonlinear waveguide parameter γ to quantify this [65]:

$$\gamma = \frac{2\pi}{\lambda} \frac{n_2}{A_{eff}},$$

(6.7)

where A_{eff} is the effective mode area, defined as $(\int |\vec{E}|^2 dA)^2 / \int |\vec{E}|^4 dA$, where $\vec{E}$ is the electric field of the waveguide. From this, we can see that Si is a highly advantageous material for exploiting $\chi^{(3)}$ nonlinearities in the mid-IR. Due to its high refractive index, the optical field confinement will be high. As discussed earlier, Si has a higher n_2 than many other CMOS materials, and at mid-IR wavelengths, the FOM is quite high due to the lack of TPA. Dispersion engineering will be discussed in Section 6.2.2.

6.2 Four-wave mixing (FWM)

6.2.1 Introduction to FWM

As mentioned in Section 6.1, four-wave mixing (FWM) is a third order nonlinear process that results from the polarizability of electrons in atoms. Specifically, we use FWM to entail the processes described in the last 4 terms of equation 6.3:

$$\frac{3}{4}\varepsilon_\circ\chi^{(3)}\left[\frac{1}{2}\left(E_{\omega_1}^2 E_{\omega_2} e^{i(2\omega_1+\omega_2)t} + c.c\right) + \therefore\right] \tag{6.8}$$

$$\frac{3}{4}\varepsilon_\circ\chi^{(3)}\left[\frac{1}{2}\left(E_{\omega_1}^2 E_{\omega_2}^* e^{i(2\omega_1-\omega_2)t} + c.c\right) + \therefore\right] \tag{6.9}$$

$$\frac{6}{4}\varepsilon_\circ\chi^{(3)}\left[\frac{1}{2}\left(E_{\omega_1} E_{\omega_2} E_{\omega_3}^* e^{i(2\omega_1+\omega_2-\omega_3)t} + c.c\right) + \therefore\right] \tag{6.10}$$

$$\frac{6}{4}\varepsilon_\circ\chi^{(3)}\left[\frac{1}{2}\left(E_{\omega_1} E_{\omega_2} E_{\omega_3} e^{i(2\omega_1+\omega_2+\omega_3)t} + c.c\right) + \therefore\right], \tag{6.11}$$

For these processes to occur, the conditions of energy conservation and momentum conservation (phase matching) need to be met, such that:

$$\omega_4 = \omega_1 + \omega_2 - \omega_3 \text{(energy conservation), and} \tag{6.12}$$

$$\beta_4 = \beta_1 + \beta_2 - \beta_3 \text{(momentum conservation)}, \tag{6.13}$$

94
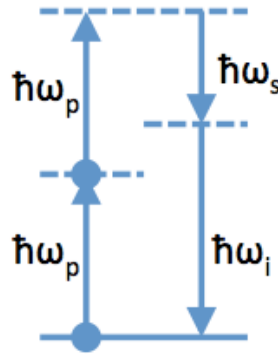
Figure 6.2.1: The phenomenon known as degenerate four-wave mixing occurs when two pump photons at the same frequency ω_p undergo nonlinear frequency conversion in a $\chi^{(3)}$ material. The conversion can either be stimulated by a signal photon, ω_s, to generate a third frequency at the idler ω_i, or it can occur spontaneously, in which the two pump photons spontaneously convert into two sidebands ω_s and ω_i.

where ω_4 and β_4 are the frequency and wave vector of the light generated through FWM. We are especially interested in the case where $\omega_1 = \omega_2$, known as degenerate FWM (Figure 6.2.1). There are two types of degenerate FWM, stimulated (a classical process), and spontaneous (a quantum process). Spontaneous degenerate FWM, in which two pump photons spontaneously generate the signal and idler sidebands, will be discussed in more detail in Section 6.3. Here, we focus on stimulated degenerate FWM, in which two pump photons mediate the conversion of a signal photon into an idler photon: $2\omega_p - \omega_s = \omega_i$. This type of FWM is often used for parametric up-conversion. For example, in the mid-IR, we may want to up-convert our signals to telecom wavelengths so that they may be more easily detected using the better detection technologies available at that wavelength range [8].

Despite Si's relatively large nonlinear susceptibility, the powers needed to achieve nonlinearities such as FWM in a Si waveguide are quite high (watt-level). This is especially problematic at the mid-IR, where multi-watt sources are limited. By using a high-Q factor resonator as our nonlinear device, we can reduce the needed input powers since a resonator with a quality factor Q and mode volume V effectively has an input power circulating within the resonator that scales linearly with Q/V. The silicon-on-sapphire ring resonators described in Chapter 5 provide an ideal platform for attaining FWM at the mid-IR, since they have high-Q factors and a multitude of modes which can be used for the pump, signal, idler, etc. Additionally, ring resonators, like all whispering gallery mode resonators, are inherently phase-matched[67, 68]. However, frequency matching in a ring resonator is not as simple, and requires careful dispersion engineering. In the next section, we discuss why dispersion engineering is necessary and how to go about doing it.

6.2.2 Dispersion engineering

It is very important to consider the group-velocity dispersion (GVD) when designing devices for nonlinear frequency generation. We can define a group delay dispersion parameter D

$$D = -\frac{\lambda}{c}\frac{d^2 n}{d\lambda^2}.$$

(6.14)

There are two regimes of GVD: normal GVD (D < 0), in which lower frequency components of a pulse travel faster through the medium than higher frequency
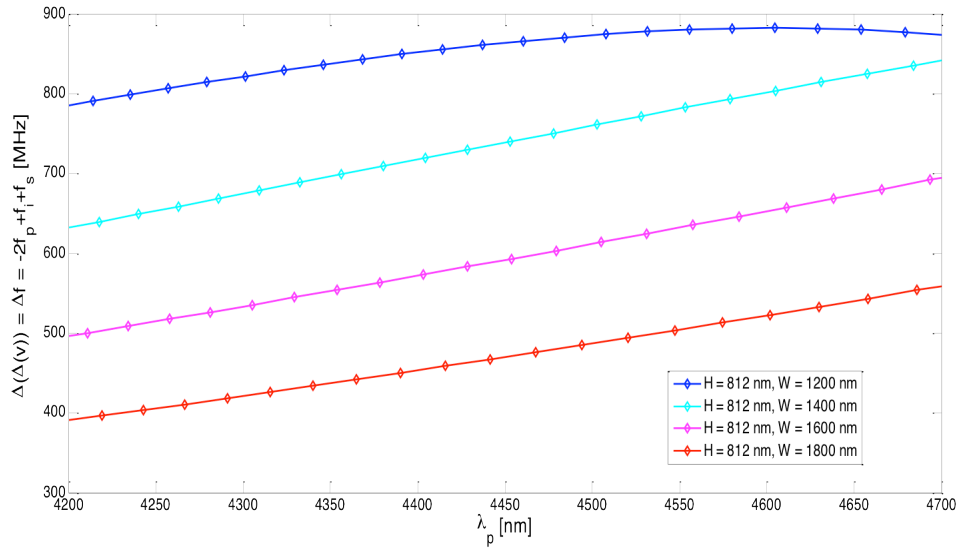
Figure 6.2.2: Expected change in FSR for fully etched silicon-on-sapphire devices for a variety of widths ranging from 1.2 to 1.8 µm (height of 812 nm.)

components, and anomalous GVD (D > 0), where higher frequency components of a pulse travel faster through the medium than the lower frequency components. At mid-IR wavelengths, Si's material dispersion is normal [66]. However, FWM requires operation in an anomalous dispersion regime, to counteract the effects of material and cavity dispersion, which cause the resonance frequencies of our ring to be irregularly spaced. Fortunately, we can compensate for the material dispersion of Si using waveguide dispersion, which is a parameter we can control in fabrication by controlling the cross-sectional dimensions of our ring. Generally, smaller cross-sectional dimensions result in higher anomalous dispersion, though we need to take care that the mode is still well-confined within the Si [69].

We used FDTD simulations to determine the expected change in FSR due to dispersion, $\Delta f = \Delta \omega_D / 2\pi$, for our SOS devices, both the fully etched devices (etch depth of 800 nm, width of 1.5 μm) and the partially etched devices (etch depth of 510 nm, width of 2.8 μm). Figure 6.2.2 shows the results for the fully etched devices for a variety of widths ranging from 1.2 to 1.8 μm, with Δf of about 400 to 900 MHz depending on the waveguide width. In the partially etched case, we obtain Δf of about 13 MHz (not shown) from 4.3 to 4.7 μm. Δf is much larger in the fully etched case as compared to the partially etched case. For stimulated FWM, we prefer that the Δf be small for a higher conversion efficiency from signal to idler, as will be discussed below, making the partially etched devices more preferable for this purpose. However, for parametric oscillation originating from spontaneous degenerate FWM (Section 6.3), a larger Δf is desirable, making the fully etched devices more preferable for this application.

6.2.3 FWM CONVERSION EFFICIENCY

Next, we would like to figure out what kind of FWM conversion efficiencies we can achieve with our devices, i.e. how much of our signal is converted to idler. From Turner et al. [68], the FWM conversion efficiency η in a ring resonator is given by:

$$\eta = \frac{I_i^{out}}{I_s^{in}} = \left| \gamma P_{pump} L_{eff} \right|^2 F_p^4 F_s F_i, \qquad (6.15)$$

where

$$L_{eff}^2 = L^2 exp(-aL) \left| \frac{1 - exp(-aL + j\Delta kL)}{aL - j\Delta kL} \right|^2, \qquad (6.16)$$

and

$$F_{p,s,i} = \left| \frac{\sigma}{1 - \tau exp(-aL/2 + jk_{p,s,i}L)} \right|^2, \qquad (6.17)$$

where I_i^{out} is the output intensity of the idler, I_s^{in} is is the input intensity of the signal, γ is the nonlinear waveguide parameter, ω_o is the pump frequency, A_{eff} is the effective mode area, P_p is the input pump power, L_{eff} is the effective length, $F_{p,s,i}$ are the resonant field enhancement factors for the pump, signal, and idler, respectively, L is the circumference of the ring, σ is the coupling coefficient, τ is the transmission coefficient, and $k_{p,s,i}$ are the wave numbers of the pump, signal, and idler fields, with a phase mismatch Δk. From this expression, we can see that a smaller value of Δk is preferred. If we take the limit where we assume that our ring resonator is critically coupled to the waveguide, that the signal, pump, and idler modes all have the same Q-factors and coupling coefficients, and $\Delta k = 0$, the generated power at the idler, P_i for a given P_p becomes [70]:

$$\eta = (\gamma 2\pi R)^2 \left(\frac{Q v_g}{\omega_p \pi R} \right)^4 P_p^2. \qquad (6.18)$$

Taking values of $Q = 200,000$, $v_g = 7.32 \times 10^7$ m/s, $R = 60$ μm, $omega_p = 4.46$ μm, $n_2 = 1.2 \times 10^{-18}$ (an extremely conservative estimate for n_2 in Si at 4.5 μm), $A_{e}ff = 1.66 \times 10^{-12}$, and $P_p = 10$ mW, which are values representative of our partially etched devices and laser sources, we obtain a conversion efficiency of **1.7%**. Similar values were obtained by solving the nonlinear coupled mode equations that describe this system. Since we do not have FCA due to TPA, we do not need to be concerned about saturation with increasing signal power as seen in [68].
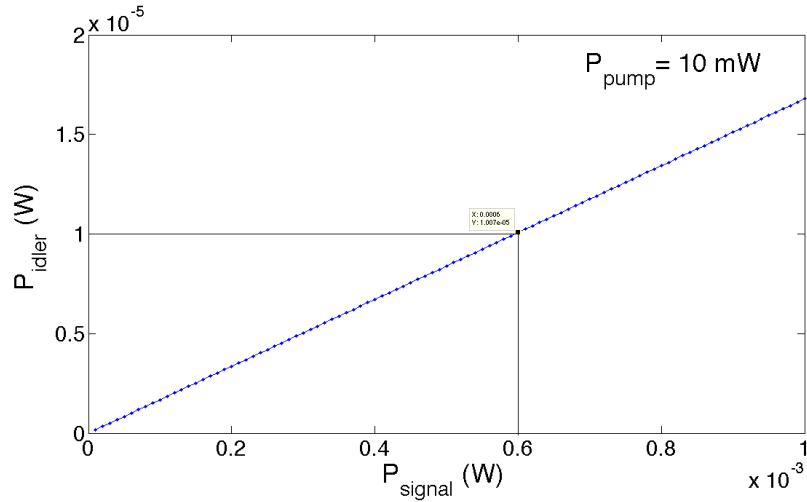
Figure 6.2.3: Expected power generated at idler P_i with varying pump power P_p. P_i values were calculated using equation 6.18 for values of Q = 200,000, v_g = 7.32x10^7 m/s, R = 60 μm, ω_p = 4.46 μm, n_2 = 1.2x10^{-18} (an extremely conservative estimate for n_2 in Si at 4.5 μm), A_{eff} = 1.66x10^{-12}, and P_p = 10 mW, values representative of our partially etched devices and laser sources.

With a conversion efficiency this high, we should be able to obtain 10 μW of idler for about 600 μW of signal and 10 mW of pump (Figure 6.2.3). These numbers indicate that the experimental demonstration of mid-IR FWM in our SOS devices should be readily attainable.

6.2.4 DESCRIPTION OF FWM EXPERIMENT

At the time of writing, we are working on demonstrating FWM in our SOS devices experimentally. We use a modified version of our experimental setup from chapters 2 and 5. A second QCL, the pump laser, has been introduced onto the input path via a 50-50 pellicle beam-splitter (Thorlabs). This QCL is a CW fixed-wavelength laser with emission at 4.46 μm and output power of 540 mW.

The pump laser can be tuned by about $\pm$ 1 cm^{-1}, or about 4 nm, via temperature tuning. The original QCL, with tunable emission from 4.3-4.6 μm and a maximum power of 200 mW, is our signal source. Of course, these numbers represent the powers emitted by the laser and not the powers actually inside the waveguide. Input from both lasers is introduced onto a grating coupler connected to a ring resonator with high Q. Using the collection beam path described in Chapter 5, we identify the signal and pump modes using the tunable laser, and then tune both the signal and pump laser to the desired resonances by monitoring the transmission signal on the detector. When the transmission signal on resonance is minimized, then we know our lasers are at the desired frequencies. Now we send the transmitted signal into a grating spectrometer (Horiba Jobin Yvon) with an external InSb detector (Horiba Jobin Yvon) mounted on an exit of the spectrometer. The output of the InSb detector is sent to a lock-in amplifier (Stanford Research Systems) which communicates with the spectrometer software, with which spectra can be read. Using this system, we can look for the generation of idlers from the signal and pump beams we introduce into our devices.

6.3 Optical parametric oscillation and frequency combs

6.3.1 Introduction

As mentioned previously, spontaneous degenerate FWM is another phenomenon that can be observed in $\chi^{(3)}$ materials. In spontaneous degenerate

FWM, two pump photons with frequency ω_p spontaneously convert into a new pair of photons: a frequency up-shifted signal photon (at frequency ω_s) and a frequency down-shifted idler photon (at frequency ω_i). This process is also known as optical parametric oscillation[67, 71]. As in stimulated FWM, this process can occur more efficiently in a microresonator if the pump, signal, and idler frequencies all coincide with modes of the resonator. Again, whispering-gallery type resonators, such as ring resonators, microspheres, and microtoroids, are well-suited for this purpose because of their multitude of phase-matched modes. The threshold for parametric oscillation is reached when the scattering rate into the signal and idler modes exceeds the cavity decay rates for those particular modes. High-Q microresonators are particularly suited for parametric oscillation as the threshold power scales with $1/Q^2$, meaning that ultra-high Q resonators can result in markedly lower parametric oscillation threshold powers.

As pump power increases, the intensity in the the signal and idler sidebands increases. At even higher pump powers, we can achieve parametric oscillation spectra with multiple sidebands. There are two processes by which this occurs (Figure 6.3.1): (1) pump photons from the pump laser can be converted to secondary sidebands, which again leads to a pairs of symmetric sidebands around the pump. (2) the generated signal and idler band themselves combine as pump photons for degenerate FWM. This process is known as cascaded FWM. When the signal and idler sidebands have comparable powers to the pump mode, cascaded FWM dominates over process (1) in terms of sideband generation.
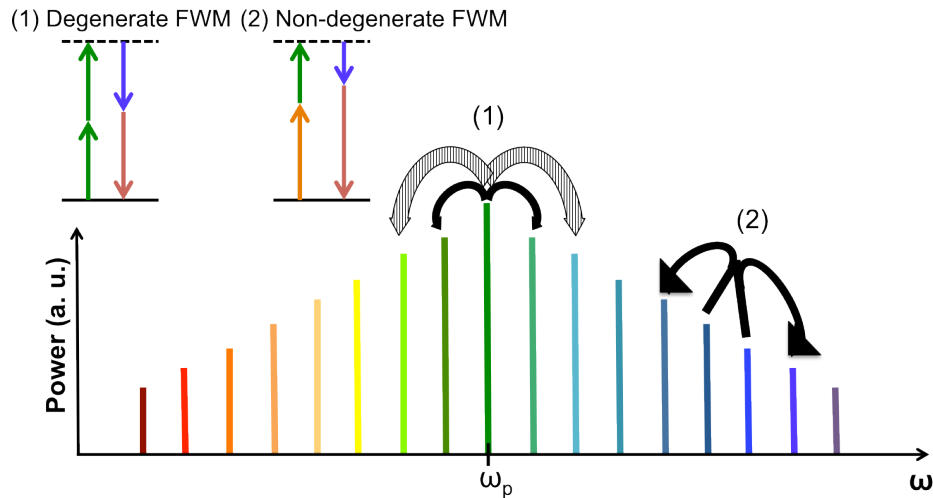
Figure 6.3.1: There are two processes by which sidebands are generated in a microresonator based parametric oscillator. (1) pump photons from the pump laser can be converted to secondary sidebands, which leads to a pair of symmetric sidebands around the pump. (2) the generated signal and idler band themselves combine as pump photons for degenerate FWM. This process is known as cascaded FWM. When the signal and idler sidebands have comparable powers to the pump mode, cascaded FWM dominates over process (1) in terms of sideband generation. The spacing between the modes is given by the FSR of the microresonator.

Through cascaded FWM, sidebands with equidistant spacings are generated. A structure emitting light at several equally spaced frequencies is known as an optical frequency comb. The bandwidth of the frequency comb is limited by dispersion, since cascaded FWM becomes less efficient once the cavity modes do not align well with the comb modes. Nevertheless, microresonator frequency combs spanning an octave of frequencies have been reported [72].

Because of the the precise spacing of the frequency lines within a frequency comb, frequency combs have elicited great interest in a number of disciplines: optical clocks, spectroscopy, and astronomy, to name only a few examples[71].

However, most of these applications have thus far been achieved with tabletop-size frequency combs made based around femtosecond lasers (these frequency combs operate on the principle of mode-locking, not on parametric oscillation as for the microresonator case[71]). For many applications, it would be preferable to have frequency combs with a much smaller footprint, i.e. the microresonator-based frequency comb. Microresonator-based frequency combs have been achieved in a number of material platforms: silica ring resonators (Hydex glass)[73], silica toroids[72], silicon nitride ring resonators[74], and crystalline (CaF_2 MgF_2)resonators [75, 76]. No frequency combs or broadband microresonator-based parametric oscillators have yet been demonstrated in Si despite its high $\chi^{(3)}$ nonlinearity[1], most likely due to the fact that TPA inhibits this possibility in telecom, where most Si photonics work is concentrated. As with stimulated FWM, the mid-IR wavelengths afford us an exciting opportunity to exploit the $\chi^{(3)}$ nonlinearities of Si in the form of a frequency comb.

Mid-IR frequency combs would be of great utility for on-chip trace gas sensing, since the mid-infrared is the "fingerprint region" where where many important molecules have absorption lines. Not only could a mid-IR frequency comb serve as a broadband source on-chip, it could also serve as an on-chip spectral analysis element. This could drastically shrink the footprint of devices for trace gas sensing, and be highly broadband to boot, thus allowing the detection of multiple gas species using a single chip. Thus far, only one mid-IR frequency comb or broadband parametric oscillator has been demonstrated, by

---

[1]We note that a widely tunable parametric oscillator has been recently reported by Kuyken et al. in [77], but this demonstration was in a waveguide, not a resonator.

C. Wang *et.al*, in a MgF$_2$ platform, with broadband operation (200 nm) around a wavelength of 2.5 μm [76]. Combs spanning wavelengths beyond 3 μm have not yet been demonstrated in any material platform. Si-based mid-IR frequency combs would be more easily integrable with other optical and electronic elements, so the possibility of Si frequency combs is an especially exciting one for on-chip trace gas sensing. The silicon-on-sapphire ring resonators described in Chapter 5 provide an ideal platform for demonstrating parametric oscillation and potentially frequency combs at the mid-IR, since they have high-Q factors and a multitude of modes which can be used for the pump and sidebands. High-Q factors are especially useful for parametric oscillation as the threshold power is inversely related to Q^2. In the following sections, we analyze the potential of our SOS devices for parametric oscillation.

6.3.2 DISPERSION ENGINEERING FOR PARAMETRIC OSCILLATION

Dispersion engineering is also a very important consideration for achieving parametric oscillation in whispering-gallery type resonators. To understand this, considering a resonator with three consecutive modes (Figure 6.3.2), the idler (ω_i), pump (ω_p), and signal (ω_s) modes, following the treatment in [78]. When we pump the center mode strongly, the frequencies of all three modes will shift due to the intensity-dependent refractive index: $n_{nl} = n_2 I$, where n_{nl} is the shift in refractive index due to the nonlinearity, and I is the circulating intensity. If we assume that our signal and idler fields are weak, the pump mode is only affected by SPM, and the signal and idler modes are affected by XPM. Recall from the

discussion in Section 6.1 that the index change due to XPM is twice that of SPM. Therefore, the frequency spacing between the pump and idler $\omega_{pi} = \omega_p - \omega_i$ will increase and the separation between the signal and pump $\omega_{sp} = \omega_s - \omega_p$ will decrease. The difference in mode spacings around the pump mode $\Delta\omega_p$ then can be written as:

$$\Delta\omega_p = \omega_{sp} - \omega_{pi} = \Delta\omega_D - \frac{2n_{nl}}{n(\omega_p)}\omega_p = \Delta\omega_D - \Delta\omega_{nl}, \qquad (6.19)$$

where $\Delta\omega_D/2\pi$ is the change in FSR due to dispersion, $\Delta\omega_{nl}/2\pi$ is the change in FSR due to the nonlinear refractive index. Since $\Delta\omega_{nl}$ is negative for Si, we can compensate for the frequency shift caused by $\Delta\omega_{nl}$ if $\Delta\omega_D > 0$ (anomalous dispersion). Thus, we need to operate in the anomalous dispersion regime to see parametric oscillation. As discussed in Section 6.2.2, both our fully etched and partially etched devices operate in the anomalous dispersion regime. The fully etched device has a larger anomalous dispersion, which makes it more suitable for broadband parametric oscillation over a large wavelength range.

6.3.3   THRESHOLD CALCULATIONS

Next, we would like to determine at what threshold power we should see parametric oscillation. This is an extremely important consideration for our experiment, since we are limited as to power output by virtue of working at the mid-IR. No high-power EDFA-type amplifiers are yet available for the mid-IR, so we are restricted to the power emitted by our most powerful QCL, 540 mW. As
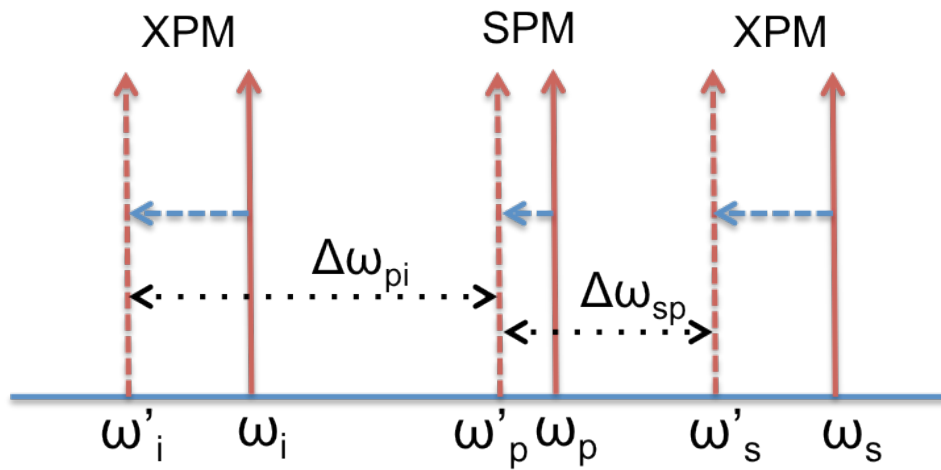
Figure 6.3.2: Consider a resonator with three consecutive modes, the idler (ω_i), pump (ω_p), and signal (ω_s) modes, following the treatment in [78]. When we pump the center mode strongly, the frequencies of all three modes will shift due to the intensity-dependent refractive index: $n_{nl} = n_2 I$, where n_{nl} is the shift in refractive index due to the nonlinearity, and I is the circulating intensity. If we assume that our signal and idler fields are weak, the pump mode is only affected by SPM, and the signal and idler modes are affected by XPM. Recall from the discussion in Section 6.1 that the index change due to XPM is twice that of SPM. Therefore, the frequency spacing between the pump and idler $\omega_{pi} = \omega_p - \omega_i$ will increase and the separation between the signal and pump $\omega_{sp} = \omega_s - \omega_p$ will decrease.

mentioned previously, parametric oscillation begins when the parametric gain exceeds the cavity loss for the sideband modes [67, 71, 79, 80]. By writing a set of nonlinear coupled mode equations to describe the amplitude evolution of the modes within a resonator when one of the modes is pumped with a laser at λ_p, and solving them in steady-state, the following expression for parametric threshold can be obtained [79, 80]:

$$P_{th} = 1.54 \frac{\pi}{2} \frac{\gamma_o + \gamma_c}{2\gamma_c} \frac{n_o^2 V_{eff}}{n_2 \lambda_p Q^2},$$

(6.20)

where γ_o is the intrinsic decay rate of the cavity mode, γ_o is the external decay rate of the cavity mode, n_o is the refractive index of the material, $V_{eff} = 2\pi R A_{eff}$ is the effective mode volume, n_2 is the nonlinear refractive index of the material, and Q is the total Q-factor of the cavity mode. Assuming $R = 60$ μm, critical coupling ($\gamma_o = \gamma_c$), $Q_t = 150{,}000$, $A_{eff} = 1.6 \times 10^{-12}$ m^2, and $n_o = 3.428$, $\lambda = 4.46m$, and an extremely conservative value of $n_2 = 1.2 \times 10^{-18}$ m^2/W, we get a parametric threshold power of about 41 mW. Using the average value for n_2 from [9], $n_2 = 3.2\text{e-}18$ m^2/W, we get a threshold power of 16 mW of power needed in the cavity. With a Q_t of just 200,000, the threshold (for the higher n_2 value) declines to 9 mW. With a high efficiency grating and careful experimental design, it should be very feasible to get 9-30 mW of the power from our 540 mW laser into our devices. These parametric threshold powers are highly promising as to the potential for using our SOS devices as parametric oscillators and possibly even frequency combs.

6.3.4 DESCRIPTION OF PARAMETRIC OSCILLATION EXPERIMENT

The measurement we plan to use to observe optical parametric oscillation is very similar to the one we are using in our FWM experiments. Of course, there is only one pump beam in this case, the 540 mW fixed-wavelength laser. By blue detuning our laser from the pump resonance, and then slowly decreasing this detuning, we can thermally lock to our laser to the cavity resonance [79]. The input path and the collection path may both be simplified in order to decrease the number of sources of loss (such as 50-50 beamsplitters) and maximize the input and output coupling efficiencies. Additionally, a higher efficiency grating may need to be fabricated so that more power may be coupled into the waveguide and ring resonator. To lower the threshold power even further, we will want to investigate methods for fabricating ring resonators with Q_t of over 200,000.

6.4 CONCLUSION

In this chapter, we presented a detailed discussion of the $\chi^{(3)}$ nonlinearities of Si, with a focus on four-wave mixing and parametric oscillation. We analyzed the suitability of our SOS ring resonators from Chapter 5 for these nonlinear frequency generation applications, and concluded that experimental demonstration of mid-IR stimulated four-wave mixing and parametric oscillation should be feasible with our devices. Ongoing experiments in this regard are described.

References

[1] Candice Tsay, Elvis Mujagić, Christi K. Madsen, Claire F. Gmachl, and Craig B. Arnold. Mid-infrared characterization of solution-processed as2s3 chalcogenide glass waveguides. *Opt. Express*, 18(15):15523–15530, Jul 2010.

[2] Richard A Soref, Stephen J Emelett, and Walter R Buchwald. Silicon waveguided components for the long-wave infrared region. *Journal of Optics A: Pure and Applied Optics*, 8(10):840, 2006.

[3] Edward D. Palik. *Handbook of Optical Constants of Solids, Volume 1*. Academic Press, 1985.

[4] Richard Soref. Mid-infrared photonics in silicon and germanium. *Nat. Photon.*, 4(8):495–497, August 2010.

[5] Bahram Jalali. Silicon photonics: Nonlinear optics in the mid-infrared. *Nat. Photon.*, 4(8):495–497, August 2010.

[6] Sanja Zlatanovic, Jung S. Park, Slaven Moro, Jose M. Chavez Boggio, Ivan B. Divliansky, Nikola Alic, Shayan Mookherjea, and Stojan Radic. Mid-infrared wavelength conversion in silicon waveguides using ultracompact telecom-band-derived pump source. *Nat. Photon.*, 4(8):506–508, August 2010.

[7] Varun Raghunathan, David Borlaug, Robert R. Rice, and Bahram Jalali. Demonstration of a mid-infrared silicon raman amplifier. *Opt. Express*, 15(22):14355–14362, Oct 2007.

[8] Xiaoping Liu, Jr. Richard M. Osgood, Yurii A. Vlasov, and William M. Green. Mid-infrared wavelength conversion in silicon waveguides using ultracompact telecom-band-derived pump source. *Nat. Photon.*, 4(8):557–560, August 2010.

[9] Nick K. Hon, Richard Soref, and Bahram Jalali. The third-order nonlinear optical coefficients of si, ge, and si[sub 1 -][sub x]ge[sub x] in the midwave and longwave infrared. *Journal of Applied Physics*, 110(1):011301, 2011.

[10] Yoshihiro Akahane, Takashi Asano, Bong-Shik Song, and Susumu Noda. High-q photonic nanocavity in a two-dimensional photonic crystal. *Nat. Photon.*, 425(6961):944–947, October 2003.

[11] Raji Shankar, Rick Leijssen, Irfan Bulu, and Marko Lončar. Mid-infrared photonic crystal cavities in silicon. *Opt. Express*, 19(6):5579–5586, Mar 2011.

[12] John D. Joannopoulos, Steven G. Johnson, Joshua N. Winn, and Robert D. Meade. *Photonic Crystals: Molding the Flow of Light, 2nd ed.* Princeton University Press, 2008.

[13] Steven Johnson and John Joannopoulos. Introduction to photonic crystals: Bloch⌧s theorem, band diagrams, and gaps (but no defects), 2003.

[14] Xiushan Zhu and Nasser Peyghambarian. High-power zblan glass fiber lasers: Review and prospect. *Advances in OptoElectronics*, 2010.

[15] Murray W. McCutcheon, Georg W. Rieger, Iva W. Cheung, Jeff F. Young, Dan Dalacu, Simon Frederick, Philip J. Poole, Geof C. Aers, and Robin L. Williams. Resonant scattering and second-harmonic spectroscopy of planar photonic crystal microcavities. *Applied Physics Letters*, 87(22):221110, 2005.

[16] Parag B. Deotare, Murray W. McCutcheon, Ian W. Frank, Mughees Khan, and Marko LonCar. High quality factor photonic crystal nanobeam cavities. *Applied Physics Letters*, 94(12):121106, 2009.

[17] M. Galli, S. L. Portalupi, M. Belotti, L. C. Andreani, L. O'Faolain, and T. F. Krauss. Light scattering and fano resonances in high-q photonic crystal nanocavities. *Applied Physics Letters*, 94(7):071101, 2009.

[18] Q. Y. Lu, Y. Bai, N. Bandyopadhyay, S. Slivken, and M. Razeghi. 2.4 w room temperature continuous wave operation of distributed feedback quantum cascade lasers. *Applied Physics Letters*, 98(18):181106, 2011.

[19] Masaya Notomi, Akihiko Shinya, Satoshi Mitsugi, Goh Kira, Eiichi Kuramochi, and Takasumi Tanabe. Optical bistable switching action of si high-q photonic-crystal nanocavities. *Opt. Express*, 13(7):2678–2687, Apr 2005.

[20] Thomas M. Babinec, Birgit J. M. Hausmann, Mughees Khan, Yinan Zhang, Jeronimo R. Maze, Philip R. Hemmer, and Marko Lončar. A diamond nanowire single-photon source. *Nat. Nano.*, 5(3):495–497, March 2010.

[21] Raji Shankar, Irfan Bulu, and Marko LonCar. Integrated high-quality factor silicon-on-sapphire ring resonators for the mid-infrared. *Applied Physics Letters*, 102(5):051108, 2013.

[22] Tom Baehr-Jones, Alexander Spott, Rob Ilic, Andrew Spott, Boyan Penkov, William Asher, and Michael Hochberg. Silicon-on-sapphire integrated waveguides for the mid-infrared. *Opt. Express*, 18(12):12127–12135, Jun 2010.

[23] Alexander Spott, Yang Liu, Tom Baehr-Jones, Rob Ilic, and Michael Hochberg. Silicon waveguides and ring resonators at 5.5 mu m. *Applied Physics Letters*, 97(21):213501, 2010.

[24] Mackenzie A. Van Camp, Solomon Assefa, Douglas M. Gill, Tymon Barwicz, Steven M. Shank, Philip M. Rice, Teya Topuria, and William M. J. Green. Demonstration of electrooptic modulation at 2165nm using a silicon mach-zehnder interferometer. *Opt. Express*, 20(27):28009–28016, Dec 2012.

[25] Kinam Kim, Jae-Young Choi, Taek Kim, Seong-Ho Cho, and Hyun-Jong Chung. A role for graphene in silicon-based semiconductor devices. *Nature*, 479(7373):338–344, 2011.

[26] Ming Liu, Xiaobo Yin, Erick Ulin-Avila, Baisong Geng, Thomas Zentgraf, Long Ju, Feng Wang, and Xiang Zhang. A graphene-based broadband optical modulator. *Nature*, 474(7349):64–67, 2011.

[27] Arka Majumdar, Jonghwan Kim, Jelena Vuckovic, and Feng Wang. Electrical control of silicon photonic crystal cavity by graphene. *Nano Letters*, 13(2):515–518, 2013.

[28] Xuetao Gan, Ren-Jye Shiue, Yuanda Gao, Kin Fai Mak, Xinwen Yao, Luozhou Li, Attila Szep, Dennis Walker, James Hone, Tony F. Heinz, and Dirk Englund. High-contrast electrooptic modulation of a photonic crystal nanocavity by electrical gating of graphene. *Nano Letters*, 13(2):691–696, 2013.

[29] Feng Wang, Yuanbo Zhang, Chuanshan Tian, Caglar Girit, Alex Zettl, Michael Crommie, and Y. Ron Shen. Gate-variable optical transitions in graphene. *Science*, 320(5873):206–209, 2008.

[30] Alfonso Reina, Xiaoting Jia, John Ho, Daniel Nezich, Hyungbin Son, Vladimir Bulovic, Mildred S Dresselhaus, and Jing Kong. Large area, few-layer graphene films on arbitrary substrates by chemical vapor deposition. *Nano letters*, 9(1):30–35, 2008.

[31] Yu Yao, Mikhail A. Kats, Patrice Genevet, Nanfang Yu, Yi Song, Jing Kong, and Federico Capasso. Broad electrical tuning of graphene-loaded plasmonic antennas. *Nano Letters*, 13(3):1257–1264, 2013.

[32] Zhi-Min Liao, Bing-Hong Han, Yang-Bo Zhou, and Da-Peng Yu. Hysteresis reversion in graphene field-effect transistors. *The Journal of Chemical Physics*, 133(4):044703, 2010.

[33] ZQ Li, EA Henriksen, Z Jiang, Z Hao, MC Martin, P Kim, HL Stormer, and Dimitri N Basov. Dirac charge dynamics in graphene by infrared spectroscopy. *Nature Physics*, 4(7):532–535, 2008.

[34] Raji Shankar, Irfan Bulu, Rick Leijssen, and Marko Lončar. Study of thermally-induced optical bistability and the role of surface treatments in si-based mid-infrared photonic crystal cavities. *Opt. Express*, 19(24):24828–24837, Nov 2011.

[35] Jiyoul Lee, Loren G. Kaake, Jeong Ho Cho, X.-Y. Zhu, Timothy P. Lodge, and C. Daniel Frisbie. Ion gel-gated polymer thin-film transistors: Operating mechanism and characterization of gate dielectric capacitance, switching speed, and stability. *The Journal of Physical Chemistry C*, 113(20):8972–8981, 2009.

[36] Laurent-Daniel Haret, Takasumi Tanabe, Eiichi Kuramochi, and Masaya Notomi. Extremely low power optical bistability in silicon demonstrated

using 1d photonic crystal nanocavity. *Opt. Express*, 17(23):21108–21117, Nov 2009.

[37] Toshitsugu Uesugi, Bong-Shik Song, Takashi Asano, and Susumu Noda. Investigation of optical nonlinearities in an ultra-high-q si nanocavity in a two-dimensional photonic crystal slab. *Opt. Express*, 14(1):377–386, Jan 2006.

[38] Paul Barclay, Kartik Srinivasan, and Oskar Painter. Nonlinear response of silicon photonic crystal microresonators excited via an integrated waveguide and fiber taper. *Opt. Express*, 13(3):801–820, Feb 2005.

[39] Vilson R. Almeida and Michal Lipson. Optical bistability on a silicon chip. *Opt. Lett.*, 29(20):2387–2389, Oct 2004.

[40] Marin SoljaČi&Cacute and JD Joannopoulos. Enhancement of nonlinear effects using photonic crystals. *Nature materials*, 3(4):211–219, 2004.

[41] M. Brunstein, R. Braive, R. Hostein, A. Beveratos, I. Rober-Philip, I. Sagnes, T. J. Karle, A. M. Yacomotti, J. A. Levenson, V. Moreau, G. Tessier, and Y. De Wilde. Thermo-optical dynamics in an optically pumped photonic crystal nano-cavity. *Opt. Express*, 17(19):17118–17129, Sep 2009.

[42] Evelin Weidner, Sylvain Combrie, Alfredo de Rossi, Nguyen-Vi-Quynh Tran, and Simone Cassette. Nonlinear and bistable behavior of an ultrahigh-q gaas photonic crystal nanocavity. *Applied Physics Letters*, 90(10):101118, 2007.

[43] Wolfram H. P. Pernice, Mo Li, and Hong X. Tang. Time-domain measurement of optical transport in silicon micro-ring resonators. *Opt. Express*, 18(17):18438–18452, Aug 2010.

[44] Xiaoge Gregory Zhang. *Electrochemistry of Silicon and Its Oxide*. Kluwer Academic/Plenum Publishers, 2001.

[45] Dieter K. Schroder. *Semiconductor Material and Device Characterization*. Wiley Interscience, 2006.

[46] Rei Kitamura, Laurent Pilon, and Miroslaw Jonasz. Optical constants of silica glass from extreme ultraviolet to far infrared at near room temperature. *Appl. Opt.*, 46(33):8118–8133, Nov 2007.

[47] Alfredo de Rossi, Michele Lauritano, Sylvain Combrié, Quynh Vy Tran, and Chad Husko. Interplay of plasma-induced and fast thermal nonlinearities in a gaas-based photonic crystal nanocavity. *Phys. Rev. A*, 79:043818, Apr 2009.

[48] Matthew Borselli, Thomas J. Johnson, and Oskar Painter. Measuring the role of surface chemistry in silicon microphotonics. *Applied Physics Letters*, 88(13):131114, 2006.

[49] Y. Yamashita, K. Namba, Y. Nakato, Y. Nishioka, and H. Kobayashi. Spectroscopic observation of interface states of ultrathin silicon oxide. *Journal of Applied Physics*, 79(9):7051–7057, 1996.

[50] H. Froitzheim, H. Lammering, and H. L. Günter. Energy-loss-spectroscopy studies on the adsorption of hydrogen on cleaved si(111)-(2×1) surfaces. *Phys. Rev. B*, 27:2278–2284, Feb 1983.

[51] Bong-Shik Song, Susumu Noda, Takashi Asano, and Yoshihiro Akahane. Ultra-high-q photonic double-heterostructure nanocavity. *Nature materials*, 4(3):207–210, 2005.

[52] Fangxin Li, Stuart D. Jackson, Christian Grillet, Eric Magi, Darren Hudson, Steven J. Madden, Yashodhan Moghe, Christopher O'Brien, Andrew Read, Steven G. Duvall, Peter Atanackovic, Benjamin J. Eggleton, and David J. Moss. Low propagation loss silicon-on-sapphire waveguides for the mid-infrared. *Opt. Express*, 19(16):15212–15220, Aug 2011.

[53] Milan M. Milosevic, Milos Nedeljkovic, Taha M. Ben Masaud, Ehsan Jaberansary, Harold M. H. Chong, Neil G. Emerson, Graham T. Reed, and Goran Z. Mashanovich. Silicon waveguides and devices for the mid-infrared. *Applied Physics Letters*, 101(12):121105, 2012.

[54] Xia Chen, Ke Xu, Zhenzhou Cheng, Christy K. Y. Fung, and Hon K. Tsang. Wideband subwavelength gratings for coupling between silicon-on-insulator waveguides and optical fibers. *Opt. Lett.*, 37(17):3483–3485, Sep 2012.

[55] Zhenzhou Cheng, Xia Chen, C.Y. Wong, Ke Xu, C.K.Y. Fung, Y.M. Chen, and Hon-Ki Tsang. Mid-infrared grating couplers for silicon-on-sapphire waveguides. *Photonics Journal, IEEE*, 4(1):104–113, Feb.

[56] Sharee McNab, Nikolaj Moll, and Yurii Vlasov. Ultra-low loss photonic integrated circuit with membrane-type photonic crystal waveguides. *Opt. Express*, 11(22):2927–2939, Nov 2003.

[57] D. Vermeulen, S. Selvaraja, P. Verheyen, G. Lepage, W. Bogaerts, P. Absil, D. Van Thourhout, and G. Roelkens. High-efficiency fiber-to-chip grating couplers realized using an advanced cmos-compatible silicon-on-insulator platform. *Opt. Express*, 18(17):18278–18283, Aug 2010.

[58] Shun Lien Chuang. *Physics of Photonic Devices, 2nd ed.* Wiley, 2009.

[59] Sébastien Le Digabel. Algorithm 909: Nomad: Nonlinear optimization with the mads algorithm. *ACM Trans. Math. Softw.*, 37(4):44:1–44:15, February 2011.

[60] T. J. Kippenberg, S. M. Spillane, and K. J. Vahala. Modal coupling in traveling-wave resonators. *Opt. Lett.*, 27(19):1669–1671, Oct 2002.

[61] Matthew Borselli, Thomas Johnson, and Oskar Painter. Beyond the rayleigh scattering limit in high-q silicon microdisks: theory and experiment. *Opt. Express*, 13(5):1515–1530, Mar 2005.

[62] Goran Z. Mashanovich, Milan M. Milošević, Milos Nedeljkovic, Nathan Owens, Boqian Xiong, Ee Jin Teo, and Youfang Hu. Low loss silicon waveguides for the mid-infrared. *Opt. Express*, 19(8):7112–7119, Apr 2011.

[63] George Imthurn. The history of silicon-on-sapphire. White Paper, 2007.

[64] B. Jalali, V. Raghunathan, R. Shori, S. Fathpour, D. Dimitropoulos, and Oscar Stafsudd. Prospects for silicon mid-ir raman lasers. *Selected Topics in Quantum Electronics, IEEE Journal of*, 12(6):1618–1627, 2006.

[65] J Leuthold, C Koos, and W Freude. Nonlinear silicon photonics. *Nature photonics*, 4(8):535–544, 2010.

[66] Q. Lin, Oskar J. Painter, and Govind P. Agrawal. Nonlinear optical phenomena in silicon waveguides: modeling and applications. *Opt. Express*, 15(25):16604–16644, Dec 2007.

[67] T. J. Kippenberg, S. M. Spillane, and K. J. Vahala. Kerr-nonlinearity optical parametric oscillation in an ultrahigh-*q* toroid microcavity. *Phys. Rev. Lett.*, 93:083904, Aug 2004.

[68] Amy C. Turner, Mark A. Foster, Alexander L. Gaeta, and Michal Lipson. Ultra-low power parametric frequency conversion in a silicon microring resonator. *Opt. Express*, 16(7):4881–4887, Mar 2008.

[69] Amy C. Turner, Christina Manolatou, Bradley S. Schmidt, Michal Lipson, Mark A. Foster, Jay E. Sharping, and Alexander L. Gaeta. Tailored anomalous group-velocity dispersion in silicon channel waveguides. *Opt. Express*, 14(10):4357–4362, May 2006.

[70] Stefano Azzini, Davide Grassani, Matteo Galli, Lucio Claudio Andreani, Marc Sorel, Michael J. Strain, L. G. Helt, J. E. Sipe, Marco Liscidini, and Daniele Bajoni. From classical four-wave mixing to parametric fluorescence in silicon microring resonators. *Opt. Lett.*, 37(18):3807–3809, Sep 2012.

[71] T. J. Kippenberg, R. Holzwarth, and S. A. Diddams. Microresonator-based optical frequency combs. *Science*, 332(6029):555–559, 2011.

[72] P. Del'Haye, T. Herr, E. Gavartin, M. L. Gorodetsky, R. Holzwarth, and T. J. Kippenberg. Octave spanning tunable frequency comb from a microresonator. *Phys. Rev. Lett.*, 107:063901, Aug 2011.

[73] L Razzari, D Duchesne, M Ferrera, R Morandotti, S Chu, BE Little, and DJ Moss. Cmos-compatible integrated optical hyper-parametric oscillator. *Nature Photonics*, 4(1):41–45, 2009.

[74] Jacob S Levy, Alexander Gondarenko, Mark A Foster, Amy C Turner-Foster, Alexander L Gaeta, and Michal Lipson. Cmos-compatible multiple-wavelength oscillator for on-chip optical interconnects. *Nature photonics*, 4(1):37–40, 2009.

[75] Anatoliy A. Savchenkov, Andrey B. Matsko, Vladimir S. Ilchenko, Iouri Solomatine, David Seidel, and Lute Maleki. Tunable optical frequency comb with a crystalline whispering gallery mode resonator. *Phys. Rev. Lett.*, 101:093902, Aug 2008.

[76] C.Y. Wang, T. Herr, P. Del'Haye, A. Schliesser, J. Hofer, R. Holzwarth, T. W. Hänsch, N. Picquè, and T. J. Kippenberg. Mid-infrared optical frequency combs at 2.5??m based on crystalline microresonators. *Nature Communications*, 4(1345), 2013.

[77] Bart Kuyken, Xiaoping Liu, Richard M Osgood, Roel Baets, Günther Roelkens, and WM Green. A silicon-based widely tunable short-wave infrared optical parametric oscillator. *Optics Express*, 21(5):5931–5940, 2013.

[78] Imad H. Agha, Yoshitomo Okawachi, Mark A. Foster, Jay E. Sharping, and Alexander L. Gaeta. Four-wave-mixing parametric oscillations in dispersion-compensated high-q silica microspheres. *Phys. Rev. A*, 76:043837, Oct 2007.

[79] T Herr, K Hartinger, J Riemensberger, CY Wang, E Gavartin, R Holzwarth, ML Gorodetsky, and TJ Kippenberg. Universal formation dynamics and noise of kerr-frequency combs in microresonators. *Nature Photonics*, 6(7):480–487, 2012.

[80] Andrey B. Matsko, Anatoliy A. Savchenkov, Dmitry Strekalov, Vladimir S. Ilchenko, and Lute Maleki. Optical hyperparametric oscillations in a whispering-gallery-mode resonator: Threshold and phase diffusion. *Phys. Rev. A*, 71:033804, Mar 2005.